Image Analysis Methods in the Measurement of Ice Loads on Structures

by

©Azam Fazelpour

A thesis submitted to the School of Graduate Studies in partial fulfilment of the requirement for the degree of

Master of Engineering

Faculty of Engineering and Applied Science

Memorial University of Newfoundland

September 2017

St. John's Newfoundland

Abstract

The icing of marine vessels and offshore structures causes significant reductions in their efficiency and creates unsafe working conditions. Ice detection and removal play important roles to reduce the risk of hazards and increase operational efficiency. Ice detection and measurement on structures are a challenge in marine industries, due to a lack of studies in this field. In this research, image processing methods are developed to measure ice loads on structures. Image processing algorithms are used to detect the ice accumulated on the structures and then the ice loads are calculated. The combination of thermal and visual imaging is suggested to detect ice, in order to reduce drawbacks occurring in these types of imaging. Also, the ice load is calculated on a known structure based on the structure information and the ice detection results. Experiments are conducted to verify the results of ice load measurements obtained by the algorithms. Ice loads are calculated in a variety of situations, such as using different imaging types, changing camera positions and angles of view and using different ice load values. The calculated ice load results show good coherence with the actual values obtained by measuring the samples which are used in the experimental setups.

Acknowledgements

I gratefully acknowledge several people who have supported and aided this thesis. The supervision of Dr. Vlastimil Masek and Dr.Yuri S. Muzychka is appreciated. Their guidance and encouragement have been a great pleasure throughout my master's studies. I appreciate the helpful advice of Dr. Saeed. R Dehghani. Learning from his bright ideas and experiences has been a great opportunity for me. Being a member of the marine icing research group has provided me with many advantages.

I am also thankful for the financial support from Statoil (Norway), ABS, MITACS, and Petroleum Research Newfoundland and Labrador (PRNL) for this research.

Contents

List of Tables

List of Figures

Nomenclature

α	Horizontal focal length
β	Vertical focal length
θ	Skew parameter
ρ	Ice density
σ_B^2	Image discrimination factor
AOV	Angle of view
D	Ice thickness
G_λ	Irradiation
$G_{\lambda,a}$	Absorption
$G_{\lambda,r}$	Reflection
$G_{\lambda,t}$	Transmission
I	Grayscale image
I_b	Binary image
h	Partial element length
I_{c1}	Binary image of the first combination

I_{c2}	Binary image of the second combination
I_{c3}	Binary image of the third combination
I_{c4}	Binary image of the fourth combination
I_g	Grayscale infrared image
I_{Hg}	Upper level of ice intensity in grayscale infrared images
I_{Hk}	Upper level of ice intensity for each component of colour infrared images
$I_k I_k$	Each component of colour infrared images
I_{Lg}	Lower level of ice intensity in grayscale infrared images
I_{Lk}	Lower level of ice intensity for each component of colour infrared images
I'_g	Grayscale visual image
$I'_{Hg} I'_{Hg}$	Upper level of ice intensity in grayscale visual images
$I'_{Hk} I'_{Hk}$	Upper level of ice intensity for each component of colour visual images
I'_k	Each component of colour visual images
$I'_{Lg} I'_{Lg}$	Lower level of ice intensity in grayscale visual images
$I'_{Lk} I'_{Lk}$	Lower level of ice intensity for each component of colour visual images
i i	Pixel row number

j	Pixel column number
l	Length
M	Ice load on structures
m	Ice load each elements
P	Vector in world coordinate system
p	Vector in image coordinate system
r	Radius
R	Rotation matrix
S	Surface area
T	Threshold value
t	Transition matrix
x_0	Origin pixel row
Y	Camera altitude
y_0	Origin pixel column

Chapter 1

Introduction

1.1 Literature Review

Marine vessels and offshore structures are faced with severe icing during cold seasons in Arctic regions. Stability, integrity and safety are some parameters threatened by icing phenomena in cold regions. Safety is affected by types of accumulated ice. Sea spray ice causes the highest hazard rating, while snow and glaze ice threaten safety less [1]. Ice accumulates from periodic wave-impact sea spray caused by wave breakup and the cold substrates of structures [2], [3]. Superstructure ice reduces platform safety by affecting stability, damaging the structure, causing the loss of communication and covering rig and equipment surfaces. Therefore, monitoring ice conditions plays an important role in predicting the icing conditions and deicing structures. The detection and measurement of ice loads are other challenges in this field of research which have been investigated for a

number of years. Models have been developed to predict the amount of ice load on the marine structures [4]–[7]. Current methods for modeling and measuring ice loads are based on physical properties. These methods need expensive equipment and human interference, which causes financial loss and increases safety hazards [8], [9]. Developing algorithms to automatically predict and remove ice accumulation is an essential component to reduce hazards and costs. Figure 1.1 illustrates thick layers of ice accumulated on a cargo ship. The ice is removed by ocean crew members [10].

Figure 1.1. Icing in the marine industry [10]

Image processing techniques have been established for ice monitoring and ice detection in several industries affected by the icing problem. Image analysis based methods have been developed to measure the ice thickness on transmission lines [11]. An on-line method is used to measure ice thickness accreted on a transmission line. The edge of iced objects is detected using two threshold methods: the floating-threshold and optimal threshold method. Wavelet-transform and floating-threshold methods effectively calculate the thickness of smooth ice, while the combination of the optimal threshold and the

morphological algorithm is effective in the detection of complex ice edges. Comparing the boundary of the ice and the structure yields the value of the ice thickness [12]. Data concerning ice intensities and locations in no-ice situations is used to improve edge detection during the measurement of ice thickness. Using this information leads to the accurate calculation of ice thickness when transmission lines drift. In another example, two cameras are used to capture images of an iced power transmission line. The corresponding points are matched in these two images using correlation methods. Ice edges are detected using 3D coordinates obtained from two images [13]. Background colour affects the detection of the ice area in images due to weather conditions and seasonal changes. A combination of a thresholding method and an edge detection method is used to more accurately detect the boundary of a transmission line covered by ice [14]. Figure 1.2 shows ice accumulation on power transmission lines.

Figure 1.2. Ice accumulation on transmission lines [1], [15]

Positive results have been obtained using visual imaging in special conditions such as in a clear scene with high contrast and appropriate lighting. Visual cameras need light during

dark conditions and cannot provide a clear image in foggy conditions [16]. In order to overcome these shortcomings of visual cameras, the use of thermal cameras is proposed. As thermal images are captured according to the object's temperature, inappropriate lighting and weather conditions do not affect imaging. This method measures the thickness of sea ice in situations in which visual imaging is unable to extract the ice boundary [17]. Thermal images reveal differences in the emissivity and temperature of objects and provide a good opportunity to distinguish ice from the background. Objects with a temperature close to the freezing point of water emit energy at a range that most commercial infrared sensors can record. Therefore, infrared thermography can be useful for ice-surface studies [18].

Some studies have been developed to monitor ice conditions and ice detection using thermal cameras. The following is a list of some of these studies of the application of thermal imaging. An infrared camera is used to monitor the surface temperature of energized airfoils and to measure the ice accretion on the airfoil in a wind tunnel. In addition, the effect of ice accumulation on the temperature of airfoils is revealed using this camera [19]. In another example, a thermal camera is used to monitor snow cover and ice conditions in winter. The real-time ice conditions are determined by classifying captured infrared images [20]. Thermal cameras can also be used for capturing the process of freezing. The front velocity of sub-cooled water at the moment water freezes is studied. An infrared camera is used to monitor the process of freezing. Four images of sub-cooled water are captured several times to monitor the velocity of the thermal front. The results produced by the infrared camera cohere with the results obtained using other methods [21]. An infrared camera and mid-infrared laser scanning can be also used to measure a 3D ice shape

without considering the type of ice. The results of 3D measurement using this method concur with the results acquired by a visual camera [22]. Furthermore, different road conditions such as snowy, icy, wet and dry can be distinguished using an infrared camera and an external source that illuminates the road with a near-infrared laser. Using three different near-infrared laser wavelengths allows for the classifying of various road conditions with higher accuracy [23]. For icing in wind tunnels, a system to measure ice shapes is developed using the laser sheet and image processing technique. Laser radiation is projected onto the ice surface, and then backscattered light reflected by the ice is detected by an IR camera. This method measures the ice shape with a high accuracy [24].

Distinguishing between saline and fresh ice is an important factor for de-icing systems in marine industries. A lab experiment is performed to detect variations in ice temperature using an infrared camera to analyze the thermal signatures of saline and fresh water ice. The behaviour of pure and saline ice with different temperatures is observed using a thermal camera. Figure 1.3 shows a result of their thermal imaging by an interval of 8 s. However, falsely detected information is still a concern [25], [26]. In another study, ice samples are located on a heated surface. Saline ice has lower conductivity compared to fresh ice. Therefore, these two types of ice show different signatures during infrared imaging [27].

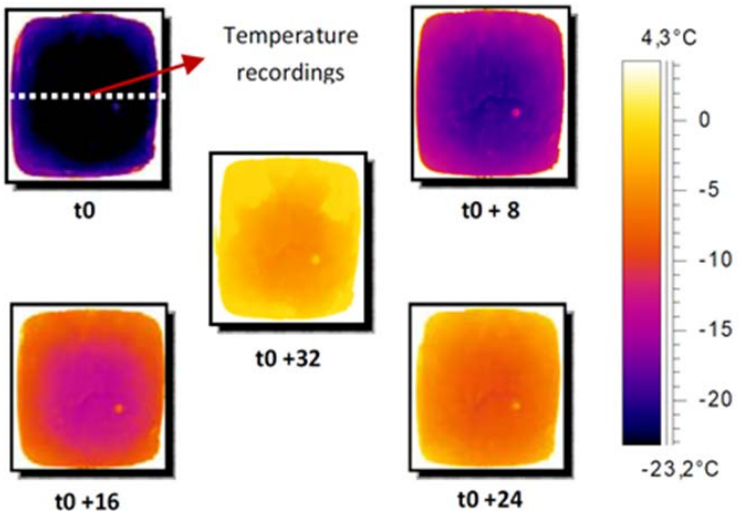

Figure 1.3. Ice signature measurements using thermal imaging [25]

1.2 Scope of Thesis

The icing of marine vessels and offshore structures causes a significant reduction in their efficiency and creates unsafe working conditions. Therefore, detecting and estimating the amount of ice load play an important role in increasing both workplace safety and the performance of the system. The goal of this thesis is to develop ice measurement methods based on image analysis.

The second chapter contains an overview of the image processing methods employed in this study. The chapter begins with an explanation of the general and the Otsu thresholding method. Then, the morphological algorithms useful in appropriate ice detection are reviewed. Camera calibration is discussed at the end of this chapter to show how to convert object coordinates in real world coordinate systems to image coordinate systems and vice versa. In chapter 3, the electromagnetic spectrum is reviewed and the infrared portion is

discussed. Some properties of the infrared portion, which is useful in ice imaging, are explained.

In chapter 4, an IR camera is calibrated for capturing images. Thermal videos of icing phenomenon are recorded. The freezing rate is calculated by applying an image processing algorithm to the data obtained by the recorded video. Furthermore, in this chapter, using thermal imaging, ice thickness is calculated for simple structures represented by an iced cylinder. The effect of light and background colour on ice thickness measurements is investigated. Then, two iced cylinders are in a single image and the ice thickness of one of them is calculated by combining thermal and visual imaging. This method can differentiate between these two distinct ice structures in an image. The combination of colour images and grayscale images is used and the results of ice thickness measurements are discussed and compared.

In chapter 5, ice is accumulated on a more complex structure as the image target. The images are captured from many points of view. The value of the ice load on this structure is obtained by analyzing the geometric information of the camera and structure and further the ice detection results. The results for four different ice loads in six camera positions are discussed.

Chapter 6 contains the main achievements of this study. Also in this chapter, some suggestions are considered for future work in the field of ice load measurement on structures in cold regions**.**

Chapter 2

Object Detection and Camera Calibration

2.1 Introduction

This chapter contains an overview of the image processing methods employed in this study. The chapter begins with an explanation of the general and the Otsu thresholding method. Then, the morphological algorithms useful in appropriate ice detection are reviewed. Camera calibration is discussed at the end of this chapter to show how to convert object coordinates in real world coordinate systems to image coordinate systems and vice versa.

2.2 The Thresholding Method

Thresholding is a popular technique for the segmentation of objects in an image. In cases where pixel intensities are divided into two modes, a threshold value of T can be assigned

to a point between these two modes to separate the image into the background part and the main object. Equation (2.1) produces a two level binary image based on the threshold value of T. Images can be segmented based on a constant or variable threshold value. Thresholding an image using a constant threshold value is called the global thresholding method [28].

$$I_b(i,j) = \begin{cases} 1 & if \quad I_g(i,j) > T \\ 0 & if \quad I_g(i,j) \leq T \end{cases} \tag{2.1}$$

Several advanced object detection methods are developed based on general image thresholding. The edges of objects are detected based on the colour difference in the image. Binary images are created by applying threshold values to the red, green, and blue components of a colour image. The edges of the object are extracted by comparing the image thresholding results. In another similar work, a thresholding value is applied to the hue, saturation and illuminance component of the image to detect the edges of an object [29].

The Otsu image thresholding method is developed to find the threshold value automatically according to statistical analysis of a grayscale image. This thresholding method optimizes the global thresholding method. The threshold value is calculated by maximizing the discriminant parameters $\sigma_B^2(T)$ between classes in the image, as shown in equations (2.2) and (2.3). The intensity value that maximizes the discriminant parameter in an image is selected as the Otsu threshold value. Also, this method is applicable to classify a wide range of images [30].

$$\sigma_B^2(T^*) = \max_{0 \leq k \leq L-1} \sigma_B^2(T) \tag{2.2}$$

$$I_b(i,j) = \begin{cases} 1 & if\ \ I_g(i,j) > T^* \\ 0 & if\ I_g(i,j) \leq T^* \end{cases} \tag{2.3}$$

Although the Otsu thresholding method is a traditional image thresholding method, it is still employed in object detection procedures. The Otsu thresholding method is applied to captured images from an airplane to detect ice created on wind turbine blades [31]. In another work, classifying particle images, the Otsu thresholding method is used to classify images into several clusters and obtain binary images [32].

2.3 Morphological Operations

Morphological algorithms are non-linear operations employed in image processing to modify images in order to be more interpretable. These algorithms are applied to images using the structuring elements and morphological operations. Structuring elements are small shapes with a specified size applied to probe the images. The type of structuring elements is selected based on the application and the object shape. Morphological operations are applied to binary or grayscale images. Dilation and erosion are two fundamental morphological operations. Other morphological operations, such as opening and closing, are developed based on dilation and erosion. The morphological algorithm is usually used to eliminate the imperfect areas that appear after image segmentation [33].

2.4 Dilation

Dilation is a basic morphological operation applied in order to fill the gaps produced in the images after segmentation. As equation (2.4) demonstrates, the dilation of object A by

the structuring element B in a binary image retains a set of areas belonging to A and B that overlap each other in at least one element when B is probing A. In other words, if the structuring element meets a pixel of the image, the value of the pixel is 1 and it is 0 otherwise.

$$A \oplus B = \left\{ z \middle| \left[(\hat{B})_z \cap A \right] \subseteq A \right\} \tag{2.4}$$

Figure 2.1 shows the dilation of a square A, with a dimension of *d*, by a square element B, with a dimension of *d/4*. As can be clearly seen, the result is a larger square with a dimension of *5d/4*. In the operating dilation, a layer of pixels is added the object boundaries. The dimension and shape of the output are controlled by the shape and size of the structuring elements [33].

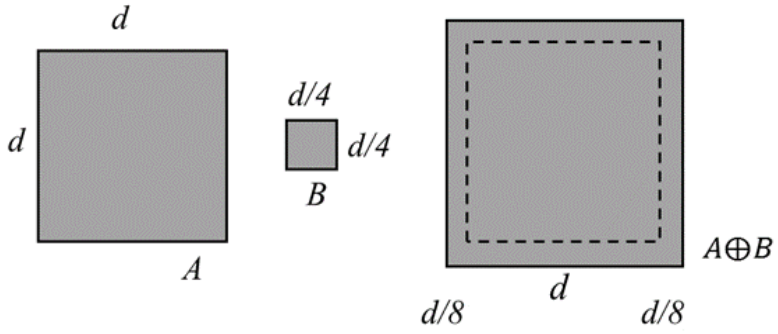

Figure 2.1. The process of dilation by a square structuring element

2.5 Erosion

Erosion is another fundamental morphological operation used to remove small unwanted parts of an image. Equation (2.5) illustrates how image A is affected by structuring element B when erosion is applied. According to this formulation, the erosion of image A by

structuring element B produces a binary image that loses points that fit in the structuring element while B is scanning A.

$$(A \ominus B)^c = \{z|(B)_z \subseteq A\}^c \tag{2.5}$$

Figure 2.2 shows a square structuring element with a dimension of *d/4* being applied to a square object with a dimension of *d*. The object dimension is reduced to *3d/4* after eroding the image. The shape and size of the eroded image are controlled by structuring elements and this operation leads to the elimination of small areas in the image [33].

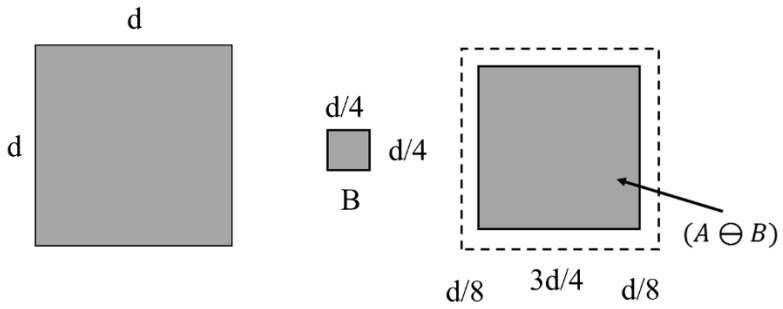

Figure 2.2. The process of erosion by a square structuring element

2.6 Camera Parameters

Camera parameters include intrinsic and extrinsic parameters, the necessary elements to convert a point from a world coordinate system to an image coordinate system and vice versa. The process of calculating these parameters is called camera calibration. In the following section, obtaining these parameters and applying camera calibration is discussed.

2.6.1 Extrinsic Parameters

Extrinsic parameters define a transformation that converts a 3D world coordinate system to a 3D camera coordinate system. These parameters are defined by the orientation and translation of the camera with respect to the world coordinate system. According to equation (2.6), the extrinsic parameter matrix M_{ext} includes the rotation matrix R and the translation vector t. The rotation matrix R is a 3×3 matrix that demonstrates the rotation of three axes of the camera coordinate system with respect to the world coordinate system. In a similar way, the translation vector, t, is a 3×1 vector that shows the relative position of the camera frames and the world coordinate system. This transformation includes six extrinsic parameters that indicate the rotation and position of the camera.

$$M_{ext} \stackrel{\text{def}}{=} [R \quad t] \tag{2.6}$$

2.6.2 Intrinsic Parameters

A camera's intrinsic parameters are used to convert the camera's coordinate system to an image plane coordinate system. In other words, these parameters are used to transfer the points from camera coordinates into pixel coordinates on the image plane. Figure 2.3 illustrates the relationship between camera and image frame coordinates [34].

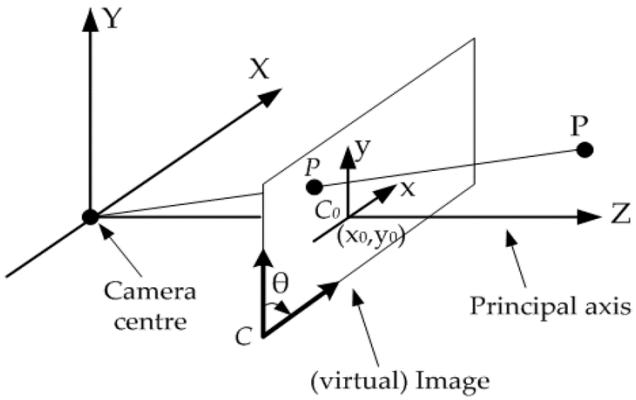

Figure 2.3. Camera and image frame coordinates [35]

The optical, geometrical and digital properties of a camera constitute the intrinsic parameters. Equation (2.7) and (2.8) determine the process of mapping points $P(X, Y, Z)$ from the camera coordinate system into $p(x, y)$ in the image frame coordinate system, where C_0 (x_0, y_0) is the image frame origin. The focal length in pixels, the skew parameter, and the principal points are five camera intrinsic parameters [34].

$$x = \alpha \frac{X}{Z} - \alpha \cot\theta \frac{Y}{Z} + x_0 \tag{2.7}$$

$$y = \frac{\beta}{\sin\theta} \frac{Y}{Z} + y_0 \tag{2.8}$$

These equations convert points from a 3D coordinate system to a 2D coordinate system. The relation between a coordinate vector $p(x, y, 1)$ in the image frame coordinate system and the coordinate vector $P(X, Y, Z, 1)$ in the camera coordinate system is formulated in equation (2.11), where M and K are obtained from equations (2.9) and (2.10).

$$K \stackrel{\text{def}}{=} \begin{bmatrix} \alpha & -\alpha \cot\theta & x_0 \\ 0 & \frac{\beta}{\sin\theta} & y_0 \\ 0 & 0 & 1 \end{bmatrix} \tag{2.9}$$

$$M_{int} \stackrel{\text{def}}{=} (K\ 0) \tag{2.10}$$

$$p = \frac{1}{z} M_{int} P_c \tag{2.11}$$

The matrix M transforms points from a camera coordinate system to an image frame coordinate system. This matrix is defined by the perspective projection of the camera, the transformation of the camera coordinate system to the image frame system and the distortion caused by the lens. In the next section, the extrinsic parameter is explained [34].

2.7 Camera Calibration

As explained in previous sections, a point in the world coordinate system is converted to the image plane coordinate system by five intrinsic parameters and six extrinsic parameters. Calculating these 11 parameters is called camera calibration. Figure 2.4 illustrates transforming a point in the world coordinate system to the image frame coordinate system.

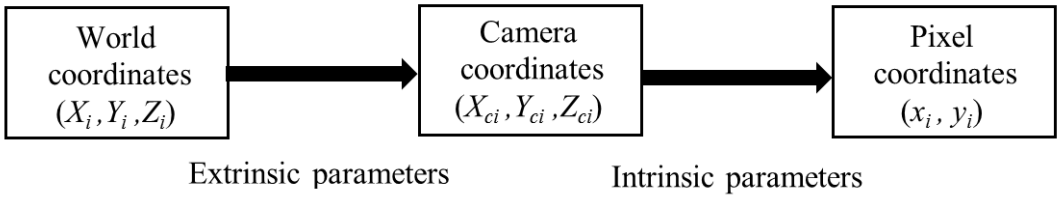

Figure 2.4. The block diagram for the camera calibration

Equation (2.12) shows the general formula for camera calibration. The intrinsic and extrinsic parameters are estimated using at least 6 known points in the world and in the

image coordinate system. In order to reduce camera calibration error, at least 6 points need to be selected.

$$p = K\ [\ R\ |t]P = MP \tag{2.12}$$

Camera calibration is performed to calculate camera parameters and has many applications in machine vision to detect, measure and recognize objects. For example, a forest fire detection system was developed using image processing methods based on fire properties such as length, height, and direction of fire. Camera calibration is used to convert the fire properties obtained in the images to the real fire properties in the world coordinate system [36].

One of the most popular methods for camera calibration to obtain camera parameters is a chessboard camera calibration method. Matlab is one software program that provides applications for camera calibration with a high accuracy using a chessboard. This software estimates intrinsic, extrinsic, and lens distortion parameters using several captured images from different directions [37].

2.8 Conclusion

Although the Otsu thresholding method is a traditional image thresholding method, it is still employed in object detection procedures by creating a binary image. Morphological operations are applied to binary or grayscale images. Dilation and erosion are two fundamental morphological operations. They are usually used to eliminate the imperfect areas that appear after image segmentation. A point in the world coordinate system is

converted to the image plane coordinate system by five intrinsic parameters and six extrinsic parameters. Camera calibration is performed to calculate these camera parameters and has many applications in machine vision to detect, measure and recognize objects.

Chapter3

Infrared Imaging

3.1 Introduction

In chapter 3, the electromagnetic spectrum is reviewed and the infrared portion is discussed. The infrared band is the portion of the electromagnetic spectrum with a wavelength of between 0.8μm and 30μm. It is located between the visible and microwave bands. Some properties of the infrared portion, which is useful in ice imaging, are explained in this chapter.

3.2 Electromagnetic Spectrum and Imaging

Electromagnetic spectrum radiation is the most important source of energy used to create images. The electromagnetic spectrum covers all electromagnetic waves based on frequencies and wavelengths. The spectrum ranges from the gamma band, with the highest energy level, to the radio band, with the lowest energy level. Figure 3.1 shows the distribution of this range. Images can be generated by detecting the radiation from each band and these images provide the necessary means for specific applications.

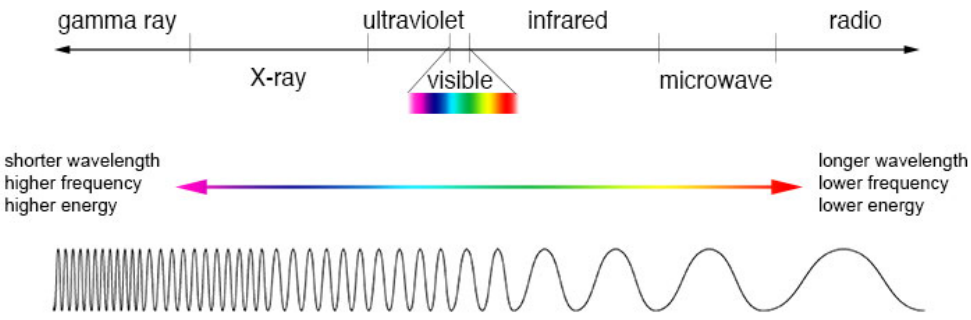

Figure 3.1. Electromagnetic spectrum [38]

When the electromagnetic irradiation contacts a semitransparent surface, it is broken down into three components by the processes of absorption, transmission and reflection. Equation (3.1) demonstrates the relation between the irradiation and transition, absorption and reflection processes in a medium.

$$G_\lambda = G_{\lambda,a} + G_{\lambda,r} + G_{\lambda,t} \tag{3.1}$$

The values of these three components vary based on the radiation wavelength and the medium type. For example, a blackbody's transmission and reflection components are zero

and all contacted radiation is absorbed regardless of the radiation wavelength. For an opaque material, no transmission occurs and all interacting radiation is absorbed in and reflected from the medium [39]. Figure 3.2 illustrates the processes of transmission, absorption, and reflection for a blackbody [40].

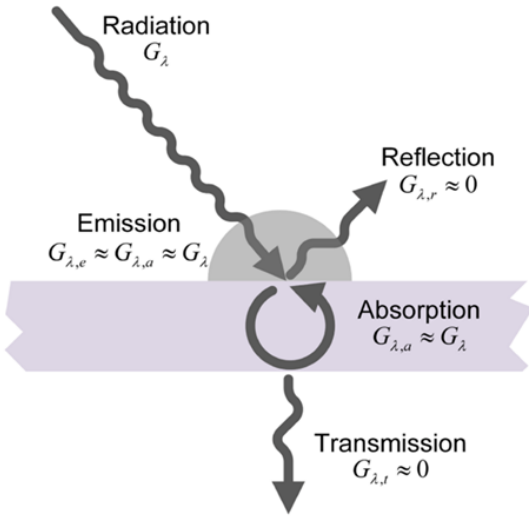

Figure 3.2. Transmission, absorption, and reflection of a blackbody [40]

Images are created by recording reflected and emitted radiation from objects. The segments of the electromagnetic spectrum are used in different imaging applications. Gamma ray imaging is usually used in medical and astronomical industries. The gamma radiation emitted from an object is obtained and detected by the relevant sensor to provide images to be analyzed. The X-ray band is another range that is used for imaging. X-ray band imaging not only produces extremely beneficial applications in the medical field, but is also applied by industries and areas such as manufacturing. The next band with imaging applications is the ultraviolet band. This band has a variety of imaging applications such as

biomedical imaging and astronomical observation. Imaging in the visible portion of the electromagnetic spectrum is the most common and applicable. Human eyes are sensitive to radiation in this band of the electromagnetic spectrum; therefore, this type of imaging is known as visual imaging. Microwave imaging is widely used in the radar remote sensing field and provides advantages such as weather prediction and the ability to acquire day and night data. The band with the shortest wavelength, the radio band, is also used for imaging. One of the applications of radio band imaging is in medicine. In magnetic resonance imaging (MRI), radio waves are illuminated on the patient's body and the waves emitted from the body are detected on an image plane [33], [41]. As a part of this thesis concerns data analysis based on infrared image processing, this portion of the electromagnetic band is explained individually in the next section.

3.3 Infrared Imaging

The infrared band is the portion of the electromagnetic spectrum with a wavelength of between 0.8μm and 30μm. It is located between the visible and microwave bands. Some parts of the infrared band are not applicable for imaging studies because these wavelengths are filtered by the atmosphere. Figure 3.3 displays the useful portion of the infrared band called the "atmospheric transmission window". The infrared band is divided according to wavelength ranges into the following parts: near infrared (NIR, 0.8-1.1 μm), short wave infrared (SWIR, 0.9-2.5 μm), mid wave infrared (MWIR, 3-5 μm), long wave infrared (LWIR, 8-14 μm), very long wave infrared (VLWIR, 12- 25 μm) and far infrared (FIR, > 25 μm). As NIR and SWIR are close to the visible band, they have the same behaviour.

This means that these two portions reflect the external light to the imaging sensor and create an image, and an external source of energy is necessary to capture infrared images at night. The MWIR and LWIR are known as the thermal band, which is useful for thermal imaging. Radiation from objects that emit thermal energy can be recorded by a thermal sensor as a thermal image and this provides beneficial information for analysis [42].

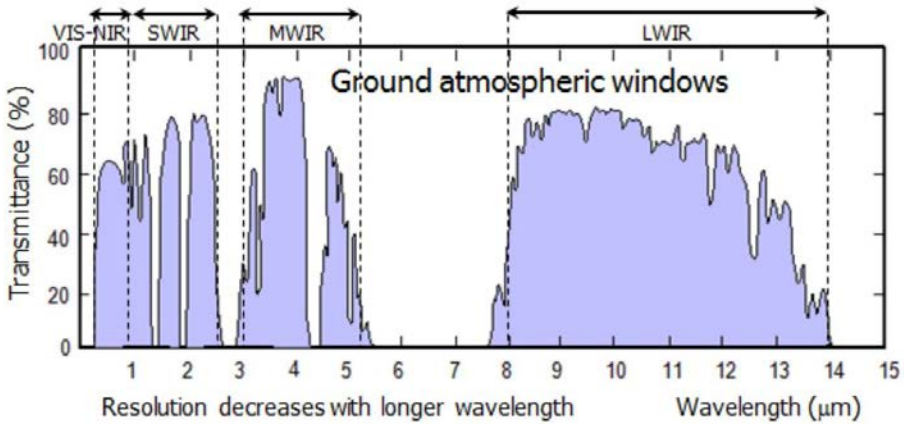

Figure 3.3. Atmospheric transmission windows [42]

For imaging in MWIR and LWIR, the infrared radiation behaviour of objects should be considered. For example, transparent mediums such as glass act similarly to a blackbody or an opaque at MWIR and LWIR wavelengths. As a result, their transmission components are zero and only the object's surface information is recorded. A benefit of imaging in the thermal band is that there is no need to use external illumination. Objects radiate thermal energy as a function of temperature and emissivity. A colder object emits less energy; therefore, appears darker in a thermal image in comparison to similar objects with a higher temperature [42].

Emissivity defines the physical properties of a material that determine the amount of material heat radiation. Two different materials with the same temperature can appear in a thermal image with different intensities. As this research focuses on ice and cold water studies, the emissivity of different types of snow, ice, and water is illustrated in figure 3.4. The figure shows that the emissivity of water, ice and snow is very close to a blackbody emissivity, which has an emissivity of 1 [40]. As a result, a thermal image of ice contains the information about the ice surface's temperature. This fact provides a valuable opportunity to apply thermal imaging in ice studies, and some of these applications are listed in chapter 1.

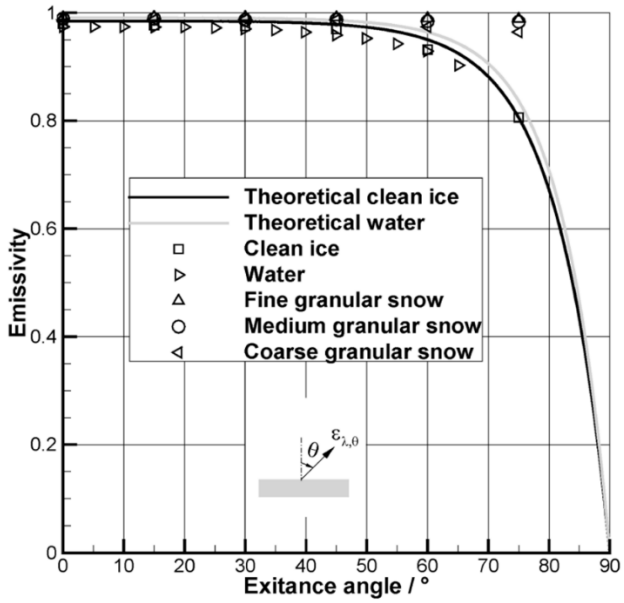

Figure 3.4. Emissivity of ice and water [40]

MWIR and LWIR cameras are used in ice and cold surface studies based on relevant applications. For example, as surfaces with higher temperatures emit energy in shorter

wavelengths, an MWIR camera is more useful for imaging in these cases, while LWIR cameras are used in colder situations [42].

3.4 Infrared Camera Calibration

In this study, an MWIR camera, Flir SC700, is used to capture images and record videos. A user calibration must be loaded on the camera to be applicable in ice studies. A temperature/radiance calibration is performed to calibrate the thermal camera. The thermal camera must be set up to see a blackbody. After defining a region of interest for the thermal camera, the calibration is performed. At least two temperature/radiance points are required for the Flir calibration wizard. A linear curve is fit to the added points; therefore, more points lead to a better calibration result.

The blackbody temperature in the region of interest is measured using a thermocouple and input into the Flir wizard to be converted to a radiance value. The selected temperature points must cover the temperature range which is studied using the thermal camera. As figure 3.5 illustrates, the collected points must show a linear characteristic. Several user calibrations can be loaded in the thermal camera based on the specific situation and application [43].

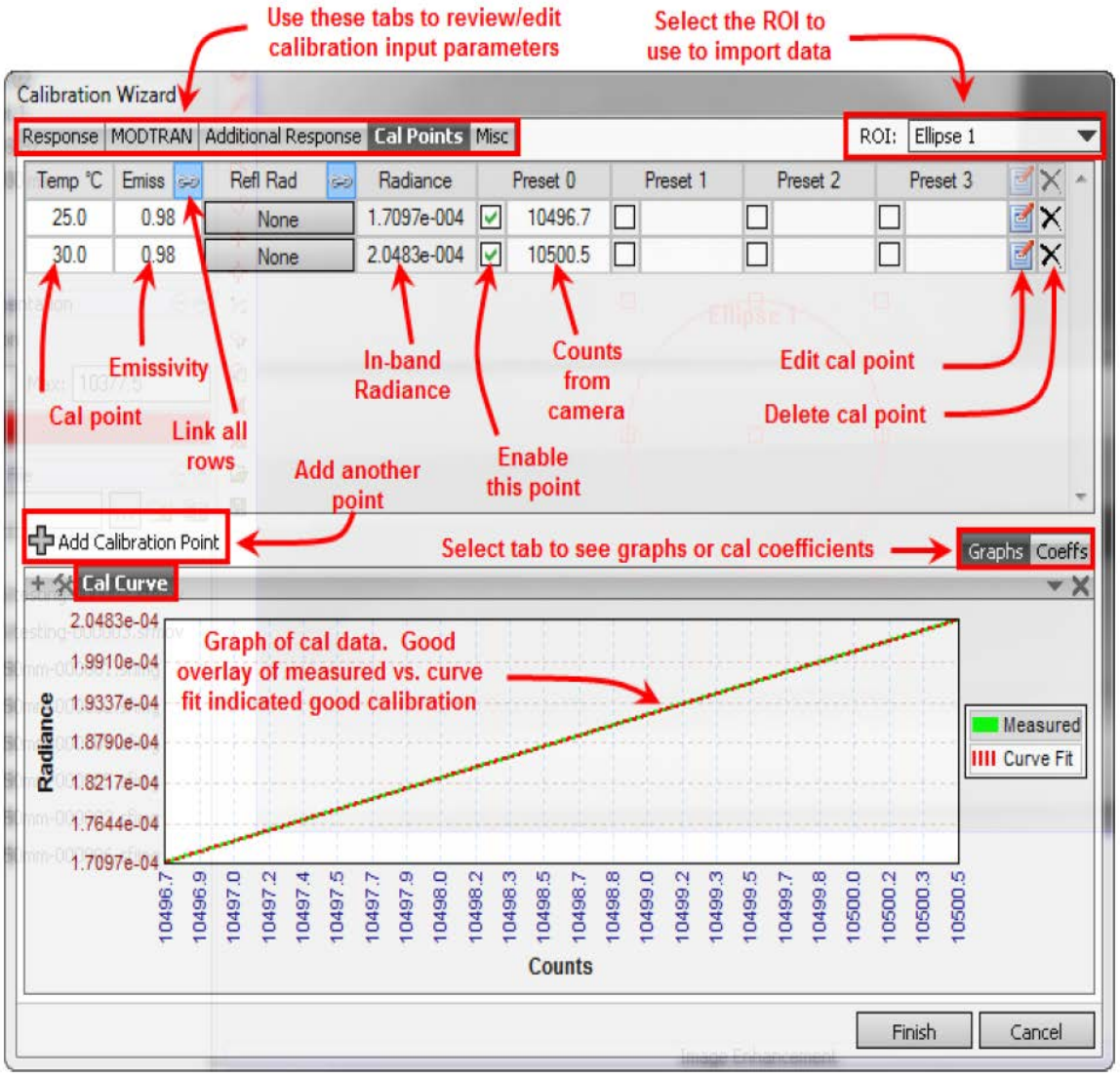

Figure 3.5. Thermal camera calibration [43]

3.5 Conclusion

A benefit of imaging in the thermal band is that there is no need to use external illumination. Objects radiate thermal energy as a function of temperature and emissivity. A thermal image of ice contains the information about the ice surface's temperature. This fact

provides a valuable opportunity to apply thermal imaging in ice studies. MWIR and LWIR cameras are used in ice and cold surface studies based on relevant applications.

Chapter 4

Ice Load Measurements on Simple Structures

4.1 Introduction

In this chapter, an IR camera is calibrated for capturing images. Thermal videos of icing phenomenon are recorded. The freezing rate is calculated by applying an image processing algorithm to the data obtained by the recorded video. Furthermore, in this chapter, using thermal imaging, ice thickness is calculated for simple structures represented by an iced cylinder. The effect of light and background colour on ice thickness measurements is investigated. Then, two iced cylinders are in a single image and the ice thickness of one of them is calculated by combining thermal and visual imaging. This method can differentiate between these two distinct ice structures in an image. The combination of colour images

and grayscale images is used and the results of ice thickness measurements are discussed and compared.

4.2 Droplet Freezing Measurements

Thermal cameras detect objects by their emissivity and IR radiance. The ice surface temperature is not uniform during transition processes. The temperature increases from the boundary of the ice towards its center. Thermal cameras are able to report temperature changes on the ice surface at every individual moment. The freezing process of saline and fresh water droplets is investigated by recording thermal videos. In this study, videos were recorded of droplets with a diameter of 2 mm at the moment of impact on cold surfaces with temperatures of -25°C, -20°C, -15°C, -10°C and -5°C in individual experiments, and the droplets were frozen. The droplet's freezing time is affected by its salinity and the surface temperature. Figure 4.1 illustrates the thermal images of droplets over a 3 s time span [44].

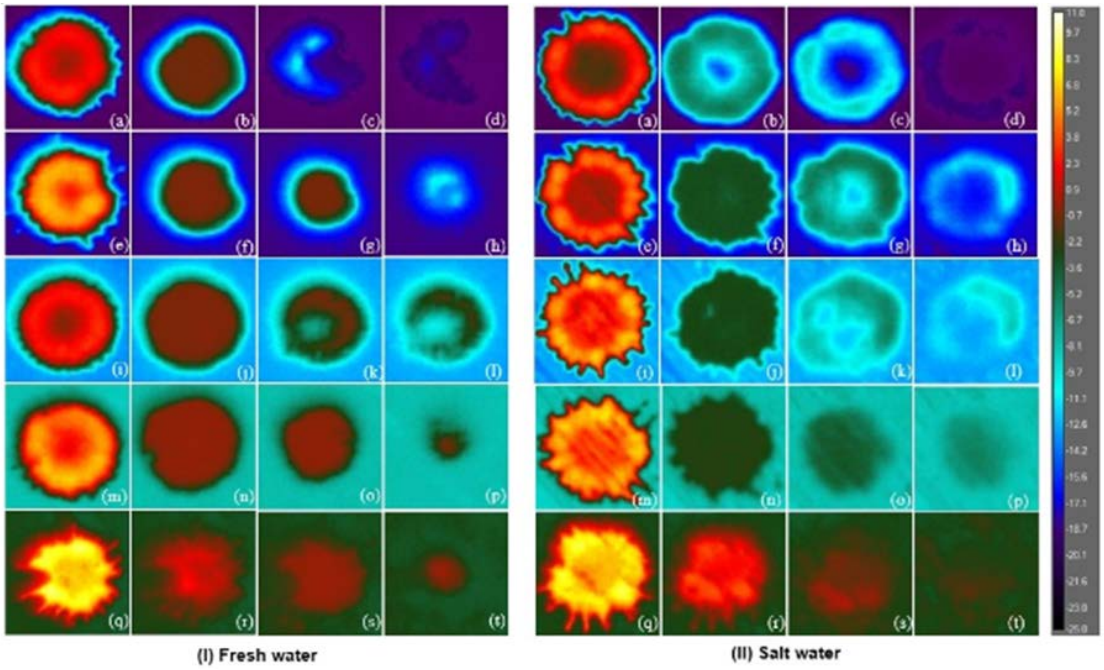

Figure 4.1. Saline and fresh water droplets impinging on cold surfaces [44]

4.2.1 **Methodology and Results**

The freezing rate of droplets provides information about their icing behaviour; therefore, an image analysis method is developed to measure a droplet's freezing rates. The method is applied to videos recorded of droplets freezing when they strike a cold surface. Images are extracted from a video at a sample rate to represent the icing phenomena. The extracted images are converted to grayscale images in preparation for the following process. In the next step, the temperatures must be converted to the image intensities; therefore, it is necessary to use a linear legend with fixed boundaries in thermal videos. If a colour legend picture is converted to a grayscale picture, the image intensity at each temperature will be obtained using software such as Matlab, as shown in figure 4.2. The intensity of the freezing temperature for a droplet is assigned as the threshold value, and by applying the

thresholding method, the droplet area is segmented into two parts: the frozen and the liquid droplet. The fraction of solidification is obtained with the percentage of the frozen part of a droplet relative to its total surface.

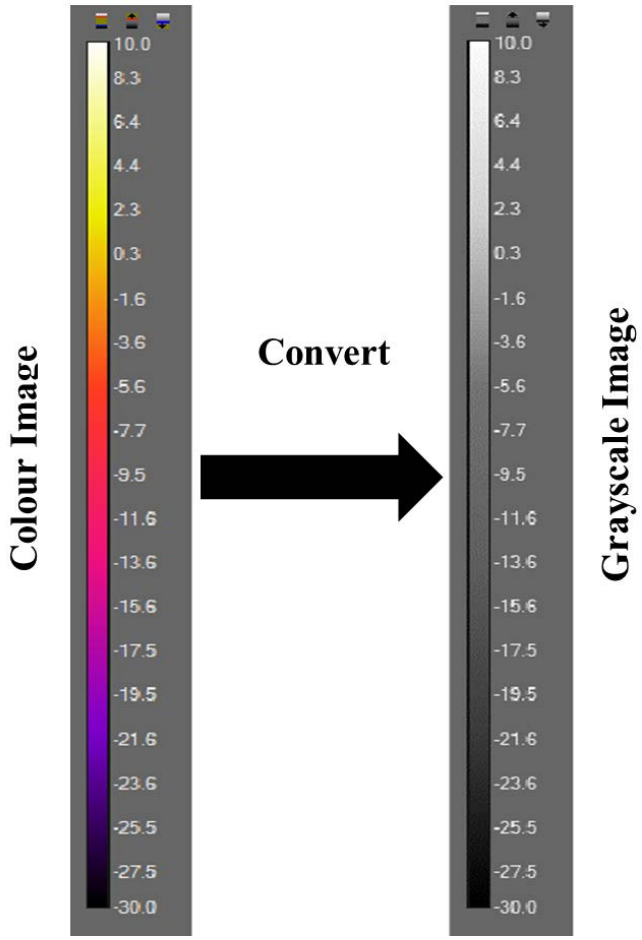

Figure 4.2. Converting a colour legend image to a grayscale legend image

Videos were recorded of droplets with a salinity value of 0‰, 20‰ and 35‰ striking the cold surfaces with temperatures of -15°C and -25°C. Images are exported from the thermal video at intervals of 0.05 s. Based on the plate and lab temperature, the boundary of the videos is set between 10°C and -30°C. The freezing points of water with a salinity

value of 35‰, 20‰ and 0‰ are determined as -2°C, -1°C, and 0°C; therefore, the threshold values corresponding to these temperatures are obtained: 155, 174, and 184.

Figure 4.3 illustrates the results of freezing rate measurements for water droplets with a salinity of 35‰ when they strike -15°C and -25°C cold surfaces. 80 percent of the droplet is frozen on the -25°C surface within 0.5 s, while just 20 percent of the droplet is solidified on the -15°C surface in this time. When the droplets meet the -15°C surface, the freezing rate is very slow in comparison to another surface. After 1.5 s, more than 80 percent of the given droplet on the -15°C and -25°C surfaces is frozen.

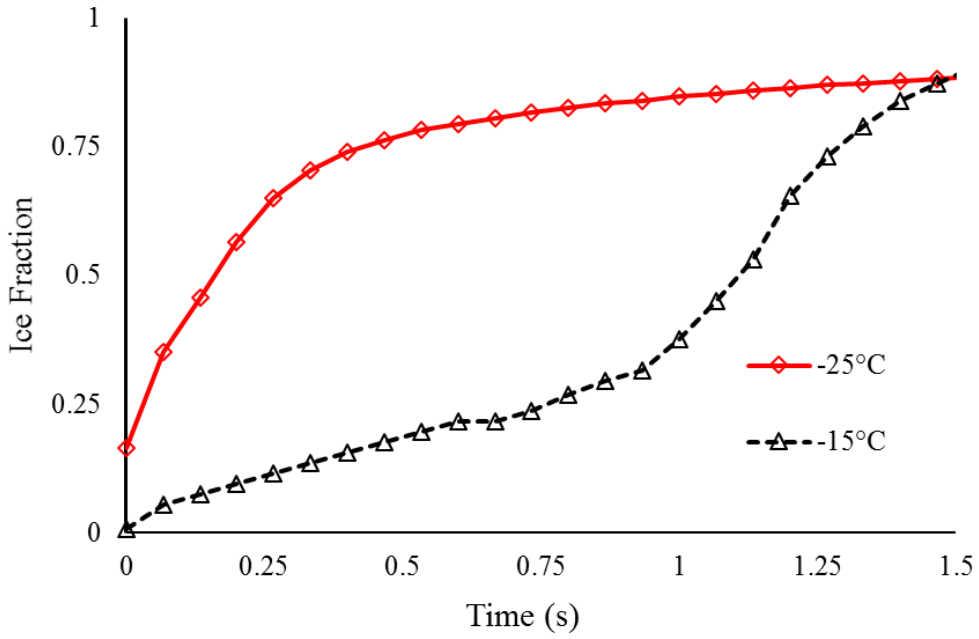

Figure 4.3. Ice fraction results for water droplets with a salinity of 35‰

Figure 4.4 shows the ice fraction for droplets with a salinity of 20‰ on cold surfaces with temperatures of -25°C and -15°C. The freezing point temperature is -1°C for these droplets. In the case that a cold surface with a temperature of -25°C is employed, after less

than 0.1 s, more than 99 percent of a given droplet is frozen, while a droplet on the -15°C surface needs almost 0.2 s to be nearly frozen.

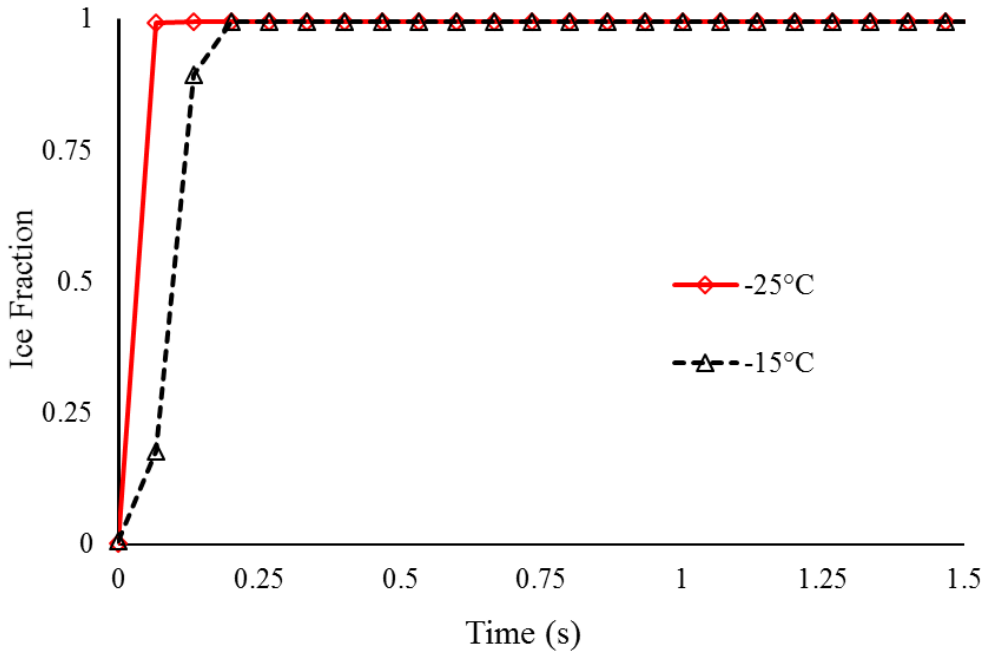

Figure 4.4. Ice fraction results for water droplets with a salinity of 20‰

In figure 4.5, the ice fractions of fresh water droplets are illustrated. As expected, using a colder surface leads to faster freezing times for droplets. The droplets, within 1.5s of contact with -25°C and -15°C surfaces, are frozen completely. Comparison figures 4.3 to 4.5 demonstrate different freezing behaviours for saline and fresh water.

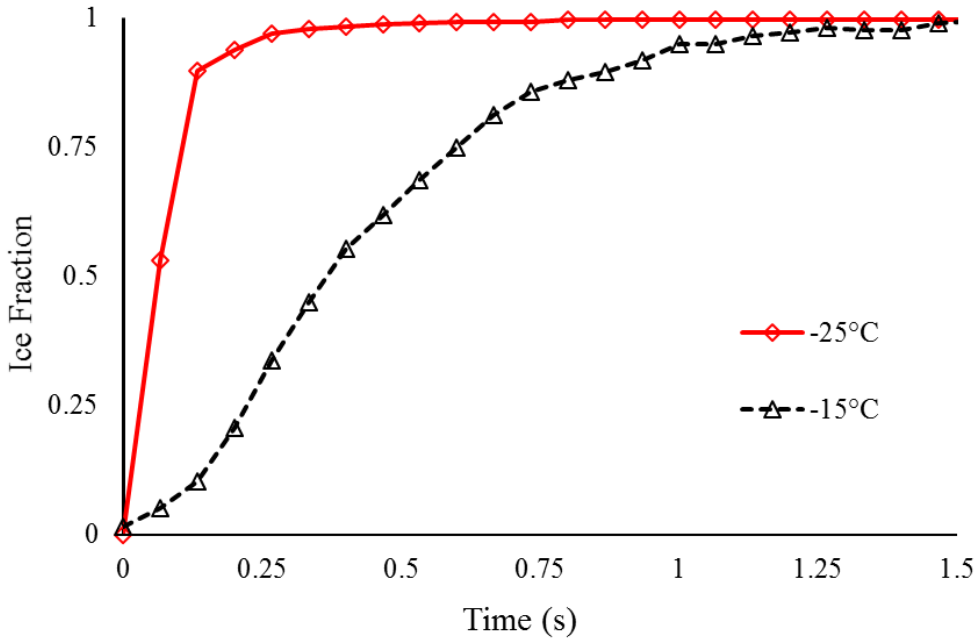

Figure 4.5. Ice fraction results for fresh water droplets

4.3 Effect of Ambient Conditions

As explained in the introduction, some indirect methods have been developed based on visual image processing to detect ice and measure its thickness. Visual cameras need light during dark conditions and cannot provide a clear image in bad weather conditions, such as foggy weather. In order to overcome these shortcomings of visual cameras, the use of thermal cameras is proposed. As thermal images are captured according to the object's temperature, inappropriate lighting and weather conditions do not affect imaging in most cases.

In this part of the thesis, a new method is developed to measure ice thickness using thermal imaging. An experiment is conducted to capture thermal infrared images. The ice

area is extracted with thresholding methods and morphological algorithms. Ice thickness is measured in both light and low flux light conditions with black and white backgrounds.

4.3.1 Methodology

Figure 4.6 illustrates the steps required in order to measure ice thickness. In the first step, a noise removal filter is required to reduce the noise before object detection. A median filter is applied to the infrared image to reduce the noise occurring in the image, while the edge of the image is preserved.

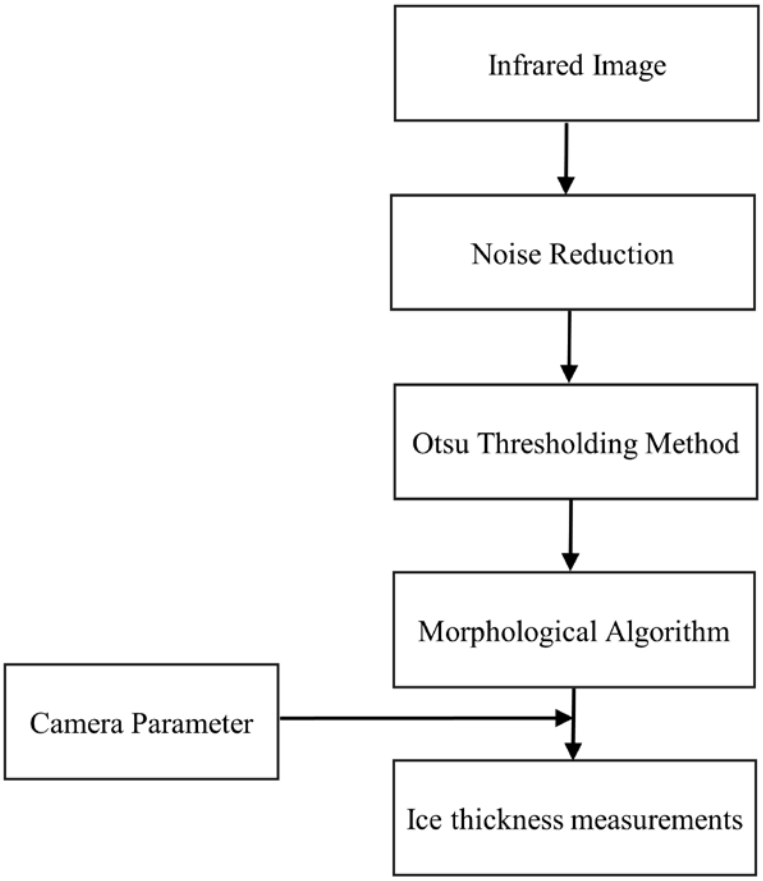

Figure 4.6. Block diagram of ice thickness measurement on a cylinder

A thresholding algorithm based on the Otsu method is performed to detect the ice, as shown in equation (4.1). This thresholding method divides the image into the background and the main target [30]. Ice pixels are represented by a value of 1 in the image and background pixels are represented by a value of 0. A binary image with some imperfect areas is thus obtained using the Otsu method. These imperfect areas are the result of small objects in the image with a similar intensity to that of ice. Erosion and dilation morphological algorithms are used to remove these imperfect areas in the binary image.

$$I_b(i,j) = \begin{cases} 1 & I_g(i,j) > T \\ 0 & Otherwise \end{cases} \tag{4.1}$$

Camera calibration is implemented using the software which accompanies the thermal camera. Using the parameters obtained by camera calibration, the pixel size is calculated. The ice thickness is measured using the number of ice pixels and the pixel size.

4.3.2 Results and Discussion

An experiment is conducted at a temperature of -15°C. A cylindrical structure, covered with ice, is the main object in the image. The camera calibration is performed by defining the distance of the thermal camera from the object and a real dimension value on the object for the thermal camera software. The effect of the background colour is investigated using a black and a white background behind the main object. In order to study the effect of light on ice measurements, images are captured in low light flux and high light flux conditions. Therefore, four cases are obtained to measure their ice thicknesses. These cases include

black background with high light, a black background with low light, a white background with high light and a white background with low light.

Figure 4.7 represents the binary images obtained by applying the steps, shown in figure 4.6, to infrared images in the four situations mentioned. Figure 4.7 (a) displays the captured infrared image using a black background and high light and figure 4.7 (b) shows the binary image obtained by applying the Otsu method on figure 4.7 (a). The boundary of the ice is extracted accurately, although visual imaging can give the same result. Figure 4.7 (c) and (d) are the results of image processing in a black background and low light situation. The ice area is detected completely, while visual imaging cannot detect the ice in this situation due to low light. Figure 4.7 (e) and (f) display the image processing results for the white background and high light case. Visual imaging needs a complicated segmentation algorithm to detect ice in this situation, while using thermal imaging ice is detected by a simple thresholding method. Figure 4.7 (g) and (h) illustrate the results of image processing for white background and low light, which are difficult situations in visual imaging. The infrared images obtained in these four combinations are almost the same; therefore, similar binary images are acquired. Although morphological algorithms cause changes in the edges of the images, these changes produce slight inaccuracies in the ice measurements.

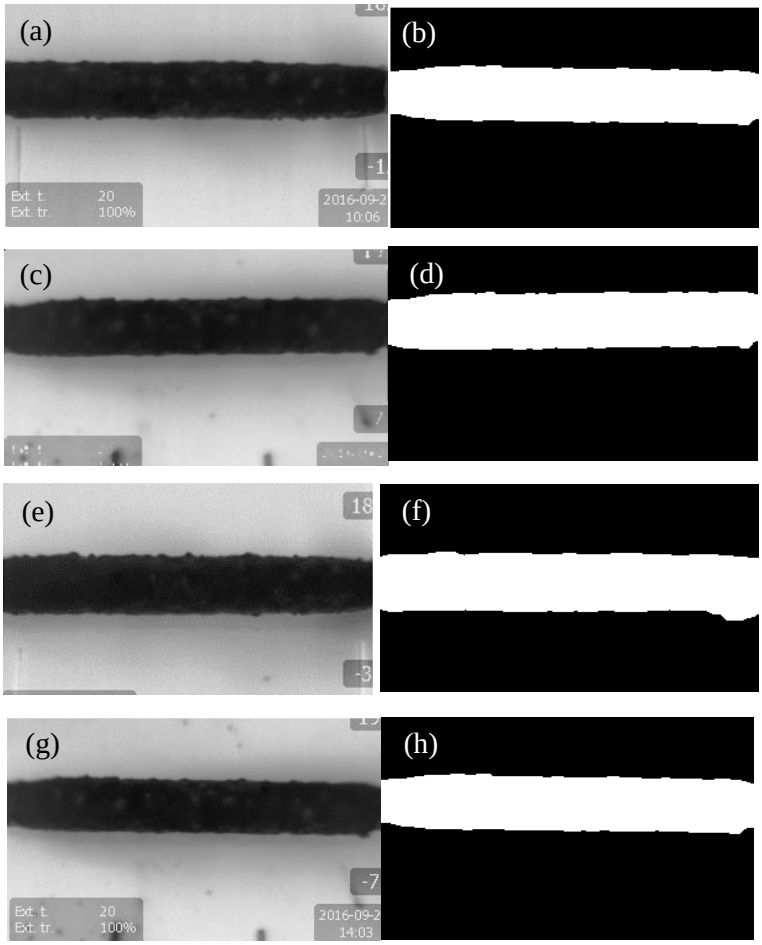

Figure 4.7. Extracted images for four cases, using different background colours and light levels

The real value measured for ice thickness is 5.3 cm. Table 4.1 shows the ice thicknesses calculated for the cases with a black and a white background at light levels of 0 lux and 350 lux. The results show high accuracy of ice thickness measurements with less than a 3 percent error. In the case with a white background and high light, the calculated ice thickness is 5.44 cm, which is less accurate than the other results. This error is caused by the dark area appearing at the end of the corresponding cylinder. This dark area, which is the result of heat transfer, is caused due to the time duration of capturing this image. The results are extremely reliable and accurate

Table 4.1. Ice thicknesses according to background colours and light levels

Light (lux)	Ice thickness (cm)	
	White Background	Black Background
0	5.24	5.21
350	5.44	5.35

4.4 Ice Loads on Structures

In this section, an analysis of infrared and visual images is performed to measure the ice thickness of a cylindrical component. The proposed method is useful for ice detection and the measurement of structures, even in harsh and low light situations, such as night. This type of analysis can fill a gap in the knowledge related to ice measurements using both visual and thermal images. Thermal imaging shows differences in the emissivity and temperature of objects. This can help to detect objects and measure the amount of ice accumulated on the objects. Combining the information of visual and thermal images can compensate for their weak points and present better results.

Combinations of colour-visual images (CVI), grayscale-visual images (GVI), colour-infrared images (CII) and grayscale-infrared images (GII) are used to find the most accurate results. A binary image is acquired using the threshold method based on data collected from infrared and visual images. Using threshold levels removes irrelevant data that come from the background. Common ice pixels detected from both infrared and visual images are considered as the ice area. Thresholding methods cause unwanted gaps and strips in binary images. Morphological algorithms are used to remove these imperfections. The best results are obtained when one of the elements of the combinations is CII. The results of using CVI

and GVI are almost the same. The experiments show that this method is reliable and its results are aligned with the real data.

4.4.1 Theory and Methodology

Measuring the intensity of ice at various points of the target object and organizing the data occur in the stage of data collection. Data collections are performed to define ice intensity ranges in infrared and visual images using the infrared and visual images taken. Iced structures are located in different positions and angles to simulate all possible cases with different behaviour. CVIs and CIIs are converted to the RGB format, and consequently, pixels in these images include red, green and blue components. Three intensity ranges are obtained for CVIs and CIIs and one intensity range is provided for GVIs and GIIs. Ice pixel ranges for images are found using ice histograms and checking ice pixel values, which are formulated in equations (4.2) to (4.5). These intensity ranges, which are acquired in this step, provide threshold levels that will be used for ice detection.

$$I_{Lk} \leq I_k(i,j) \leq I_{Hk} \qquad k = Red, Green, and\ Blue \tag{4.2}$$

$$I'_{Lk} \leq I'_k(i,j) \leq I'_{Hk} \qquad k = Red, Green, and\ Blue \tag{4.3}$$

$$I_{Lg} \leq I_g(i,j) \leq I_{Hg} \tag{4.4}$$

$$I'_{Lg} \leq I'_g(i,j) \leq I'_{Hg} \tag{4.5}$$

After data collection, several steps are needed to obtain the ice thickness value. Figure 4.8 shows the steps that lead to ice thickness measurements. Preprocessing includes image

resampling and noise reduction is applied to visual and infrared images in the first step. In these experiments, the resolution of infrared images is less than that of visual images. Therefore, the infrared and visual images should be converted to the same image size in order to combine the information correctly. Image resampling is performed for the infrared image to obtain the same size as the visual image. Some noise is generated in the visual image and filtering is performed to reduce noise in the image before the object detection. The median filter is chosen to remove the noise while the edge of the ice is preserved.

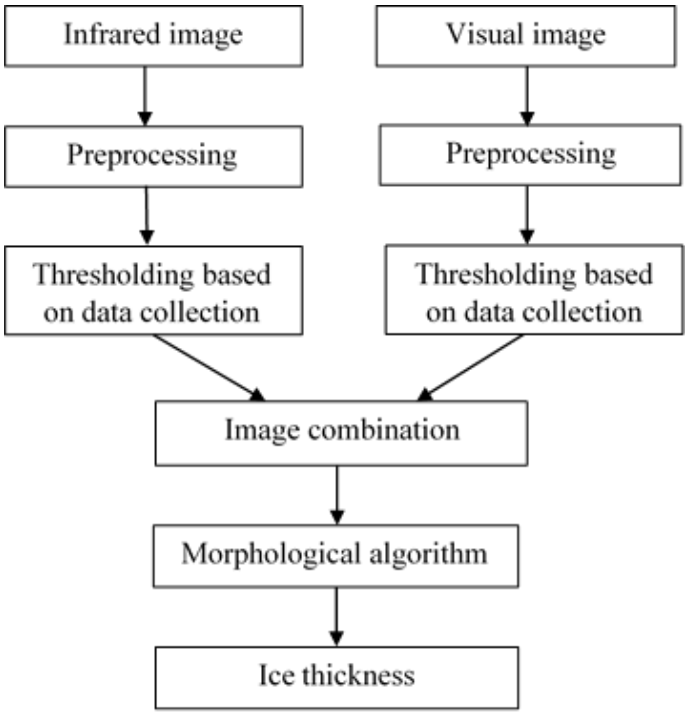

Figure 4.8. Block diagram of ice thickness measurement, combining thermal and visual imaging

In the next step, threshold levels, obtained from equations (4.2) to (4.5), are used to classify images into the background and ice area categories. Pixels that do not belong to the ice intensity range are eliminated and replaced by the value of 0, the ice pixels are

valued as 1 and a binary image is formed [45]. Four binary images are obtained by thresholding CVIs, CIIs, GVIs and GIIs. Using the AND function for the combination of four binary images provides four new binary images that contain the information of both infrared and visual images. The first binary image is created by the combination of the thresholded CII and thresholded CVI and shown as $I_{c1}(i,j)$. The second binary image is obtained using the thresholded CII and thresholded GVI with the name of $I_{c2}(i,j)\mathrm{I}_1$. The third binary image is defined using the combination of the thresholded CVI and thresholded GII and defined as $I_{c3}(i,j)$. The combination of the thresholded GVI and thresholded GII creates a binary image with the notation of $I_{c4}(i,j)$. Equations (4.6) to (4.9) formulate all the mentioned combinations.

$$I_{c1}(i,j) = \begin{cases} 1 & I_{Lk} \le I_k(i,j) \le I_{Hk} \; and \; I'_{Lk} \le I'_k(i,j) \le I'_{Hk} \\ 0 & Otherwise \end{cases} \tag{4.6}$$

$$I_{c2}(i,j) = \begin{cases} 1 & I_{Lk} \le I_k(i,j) \le I_{Hk} \; and \; I'_{Lg} \le I'_g(i,j) \le I'_{Hg} \\ 0 & Otherwise \end{cases} \tag{4.7}$$

$$I_{c3}(i,j) = \begin{cases} 1 & I_{Lg} \le I_g(i,j) \le I_{Hg} \; and \; I'_{Lk} \le I'_k(i,j) \le I'_{Hk} \\ 0 & Otherwise \end{cases} \tag{4.8}$$

$$I_{c4}(i,j) = \begin{cases} 1 & I_{Lg} \le I_g(i,j) \le I_{Hg} \; and \; I'_{Lg} \le I'_g(i,j) \le I'_{Hg} \\ 0 & Otherwise \end{cases} \tag{4.9}$$

$$k = Red, Green, and\ Blue$$

The lack of collected data may cause black gaps in the ice area of binary images. Also, the same intensity values of the background and ice area cause the creation of some small white strips, which are connected to the ice area. Morphological image processing algorithms are used to correct or remove imperfect areas are obtained by the threshold method. The closing morphological algorithm removes small black areas, which are surrounded by the ice area. The opening morphological algorithm is used to eliminate white strip areas.

In order to calculate pixel size in the real world coordinate system, a camera calibration is performed to measure each pixel size using the thermal camera's software. The iced surface area is calculated using the multiplication of the calculated pixel size and the number of ice pixels, which is determined from the binary image. The ice surface is assumed to be rectangular; its width is the iced structure diameter and its length is the structure length. Ice thicknesses are measured by subtracting the structure thicknesses from the iced structure thicknesses [12].

4.4.2 Results and Discussion

Experiments are conducted in a cold room which has a temperature of $-20 \pm 1℃$. A cylindrical component with an outer diameter of 4 cm, covered by saline ice with a salinity of 35‰, is used as the target object of image processing. Another cylinder, which acts as part of the background, is covered by fresh water ice to represent old ice, which has lower salinity, or ice located far from the target cylinder. The size of the background cylinder is

the same as the target cylinder. This cylinder is located behind the first cylinder. The wall of the cold room, which is behind the cylinders, acts as the rest of the background. Two cylindrical components are placed at five different angles and arrangements, making five different cases in this research. The camera is located at a distance of 1.45 m to the front object during the imaging. The camera calibration is performed using infrared camera software, the distance of the camera to the front object and also by defining a real dimension value of the object in the software.

The specified steps in the methodology are used to extract and measure ice thickness. Four combinations of visual and infrared images are compared to determine which combination is more accurate. The combinations are CII-CVI, CII-GVI, GII-CVI and GII-GVI. After preprocessing of the images, several images containing the iced structure are used to determine threshold levels for infrared and visual images. Table 4.2 shows the threshold levels which are obtained for red, green and blue components and grayscale images.

Table 4.2. Threshold levels for components of R, G, B and grayscale images

Channel	Visual image		Infrared image	
	Lower level	Upper level	Lower level	Upper level
R	43	133	25	160
G	58	132	0	31
B	51	120	90	178
Grayscale	61	122	30	66

Five cases with different arrangements and angles are investigated to define their ice thicknesses. The histogram of case number 1 is calculated to discuss possible results. As

figure 4.9 (a) shows, the histograms of three components, red, green and blue, which are R, G, and B, are centered of the intensity of 100 in their visual image and their deviations are almost the same. The grayscale histogram of the visual image is very similar to R, G and B histograms in shape, shown in figure 4.9 (b). Demonstrated in table 4.2, the ice pixel intensity levels have similar values for R, G and B components and the grayscale image. Therefore, the CVI does not have more information than the GVI does.

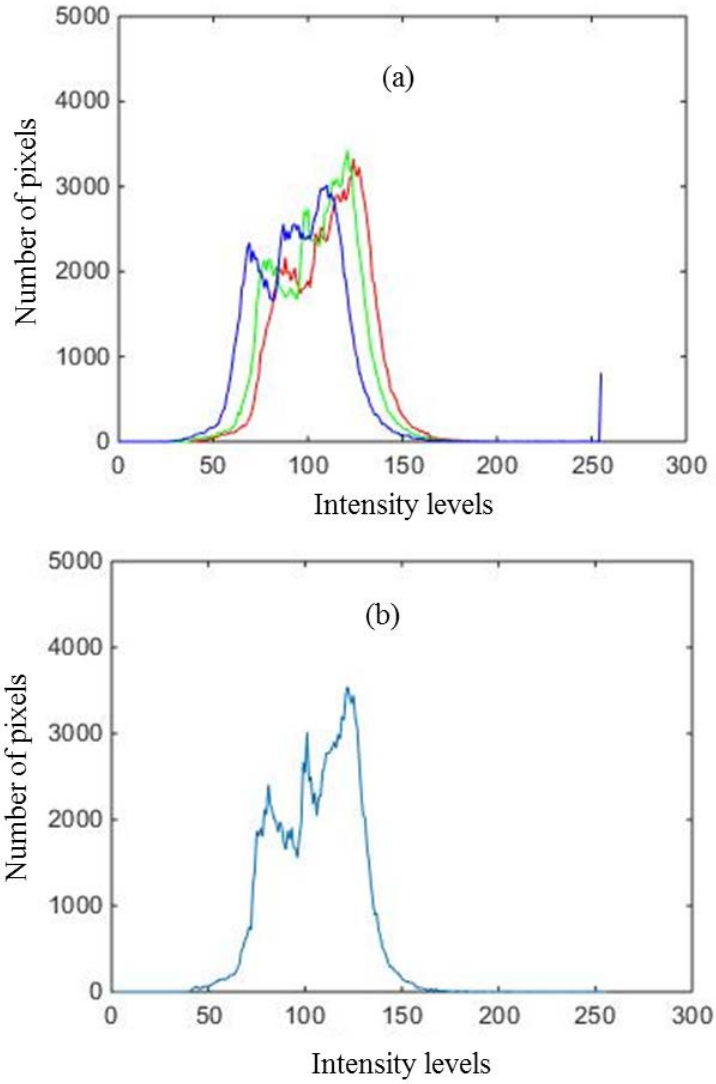

Figure 4.9. Histograms of the visual image of case number 1

The histogram of the CII, figure 4.10 (a) and the histogram of the GII, figure 4.10 (b) show different trends and shapes. According to data from table 4.2, the values of ice intensity levels are different for the three components, R, G and B. Therefore, using combinations that include CII or GII causes different results. The colour image has three independent components and there is more information in this type of image; consequently, the result of using CII is more accurate than that of GII.

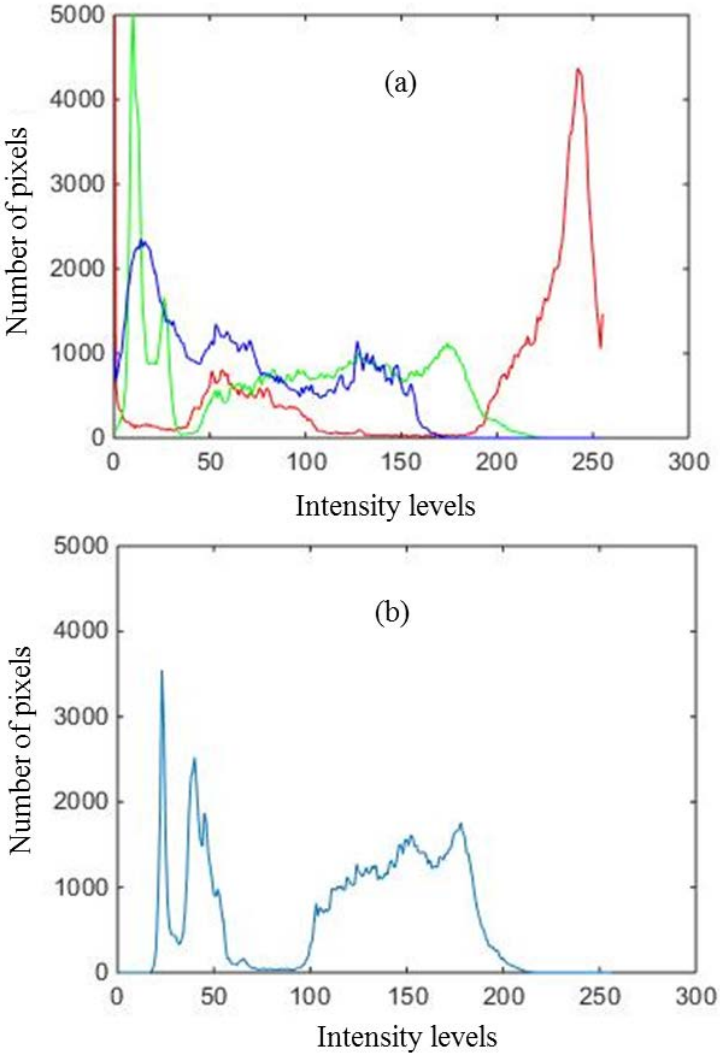

Figure 4.10. Histograms of the infrared images of case number 1

The threshold method is applied on images to create binary images. Binary images are obtained for five cases using different combinations of infrared images and visual images. In all cases, the target cylinder, covered by saline ice, is on top of the second cylinder, covered by fresh water ice. Some shadow appears in the visual image. The shadow does not have any effect on infrared images but its effect is shown in visual images. Therefore, using infrared images removes the effect of the shadow in the results.

In case number 1, as figure 4.11 (a) and (b) show, the main cylinder mostly covers the lower one. Due to the different temperature and emissivity of the background with respect to the target object, the colour of the target object is different from the background. This contrast with the background helps to extract the object from the background using threshold levels. Figure 4.11 (c) shows the binary images acquired using the combination of CVI and CII. This combination shows fairly good results. Figure 4.11 (f) shows the binary image obtained using the combination of GII, figure 4.11 (d) and GVI, figure 4.11 (e). An extra part is shown in figure 4.11 (f) that shows the threshold has considered part of the fresh water ice as the target ice. The shapes of the ice are detected and reported well in the binary image.

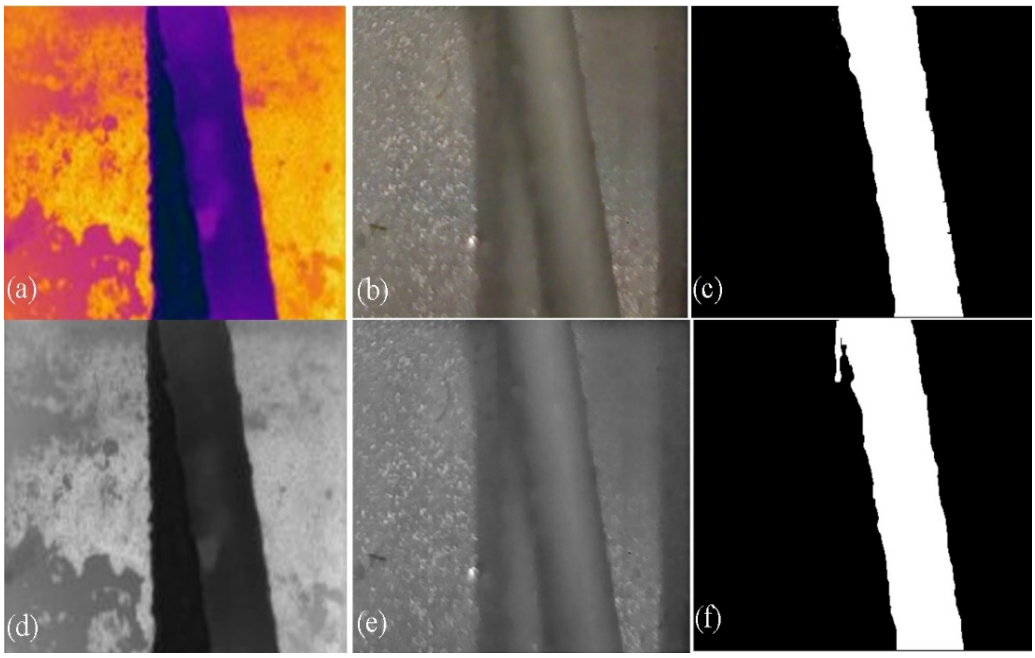

Figure 4.11. Extracted images for case number 1

In case number 2, the target cylinder only covers a small portion of the second cylinder, as shown in figure 4.12. In both infrared and visual images, the second cylinder has the same colour as the main cylinder; therefore, the object cannot be extracted using only the threshold method. Morphological algorithms are used to remove the effect of the similarity of the object and the background. Figure 4.12 (c) shows the binary image acquired using figure 4.12 (a) and (b). Figure 4.12 (f) shows the binary image obtained using GVI and CII and figure 4.12 (d) displays the binary image created combining GVI and GII. There is no difference between the results of the first and second combination. The effect of using the morphological algorithms in the boundary of the binary image is shown in figure 4.12 (c) and (e).

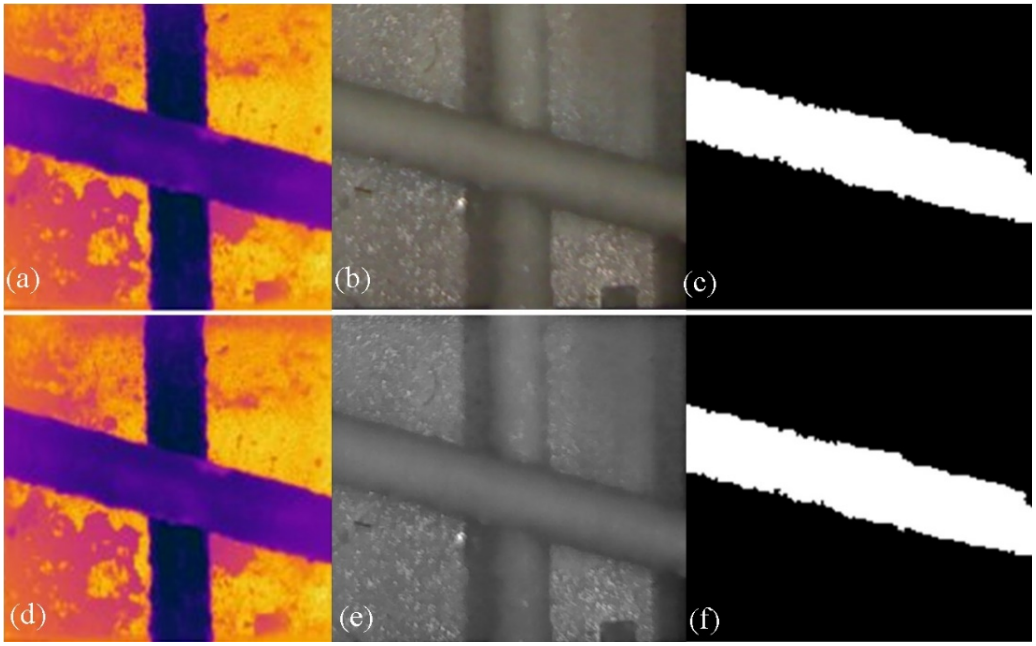

Figure 4.12. Extracted images for case number 2

As figure 4.13 shows, in case number 3, some parts of the object have the same colour as the background in the CII. The visual image helps to recognize the correct ice area of the target object and remove the part of the background that is considered as ice in the infrared image. Using infrared images, the shadow that appears in the visual image and has the same intensity, as the ice is considered as the background. The morphological algorithms that are used to remove imperfection have a negative effect on the boundary in binary images. The combination using GII is affected more by the morphological algorithms than that of CII, and the ice in the bottom of the cylinder is not detected. Figure 4.13 (c) demonstrates the binary image using the combination of CII and CVI and figure 4.13 (d) displays the binary image using the combination of GII and GVI.

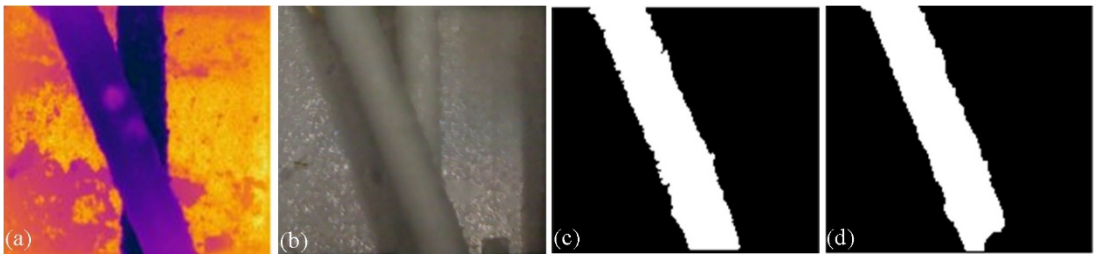

Figure 4.13. Extracted images for case number 3

In case number 4, the visual image shows no ice in the bottom of the target cylinder, figure 4.14 (b), but because the cylinder has the same temperature as the ice, it has the same colour as the ice in the infrared image, figure 4.14 (a). According to this proposed method, a pixel is considered to be ice if it belongs to the ice range of the visual and infrared images. Therefore, the bottom of the cylinder, which does not belong to the visual ice intensity range, is assumed as the background. Using CII in a combination has a better result than the combination that uses GII. The effect of the morphological algorithm is shown in the boundary of binary images. Figure 4.14 (c) represents the binary image using the combination of CII and CVI and figure 4.14 (d) displays the binary image using the combination of GII and GVI.

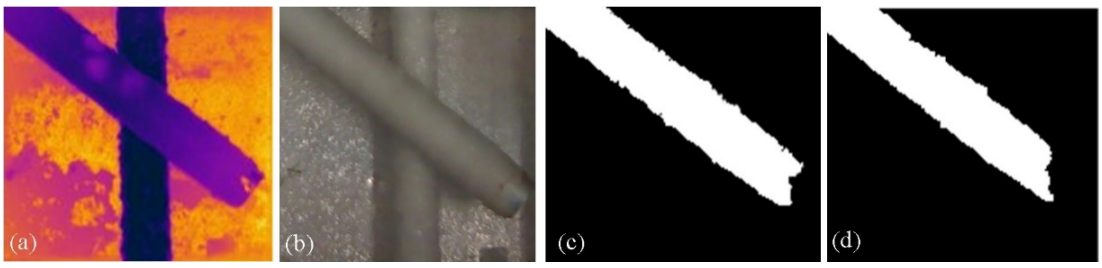

Figure 4.14. Extracted images for case number 4

In case number 5, two cylinders are almost orthogonal to each other with a high similarity between the background and objects, shown in figure 4.15. When applying the threshold method on a single image, these parts of the background are considered as the target object. Combining the images helps to recognize the ice area and background correctly. There are some similarities between the boundaries of fresh water and saline ice which appear in infrared and visual images. The morphological algorithms are used to remove these similarities. The effect of morphological algorithms on boundaries of ice is shown in figure 4.15 (c) and (f) which are the results of the combination of CII and CVI, figure 4.15 (a) and (b), and the combination of GII and GVI, figure 4.15 (d) and (e). The combination of GII and GVI shows less accuracy in ice detection.

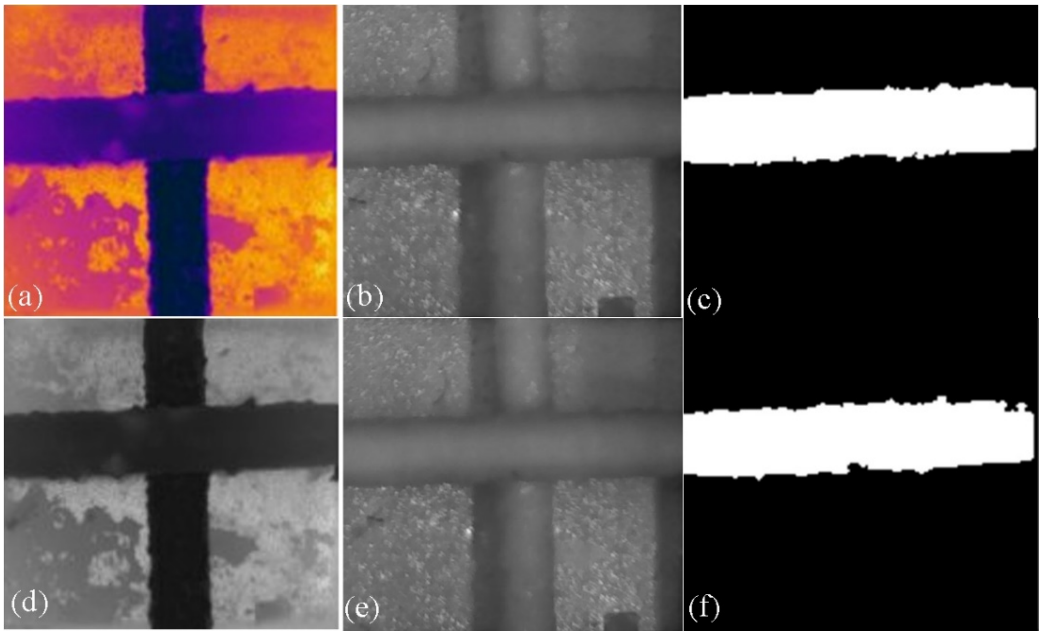

Figure 4.15. Extracted images for case number 5

The ice thickness is measured at several points. The ice thickness is about 1.75 cm. Figure 4.16 shows the numerical results of the ice thickness calculated for every case. The results show that the combinations that use CII calculate the ice thickness more accurately, while the combinations that use GII have less accuracy. These results indicate that the combination with CVI has the same results as those of GVI, which is expected from figure 4.9. In cases 3 and 4, using GII causes more inaccuracy in the results than in other cases. In case number 3, the main object and the background have a similarity in some areas. Using CII in the combination is more useful to detect the ice area than using GII. A larger size of an opening morphological algorithm is needed to remove the additional area that appears when using GII in the combination. Increasing the opening function size causes an increase in inaccuracy. In case number 4, the morphological algorithms remove the area distributed around the bottom and reduce the number of ice pixels. As a result, a thinner ice is calculated in this case. The values of these results are less than those of the experimental result because the opening morphological operation is used to eliminate thin protrusions in the binary image.

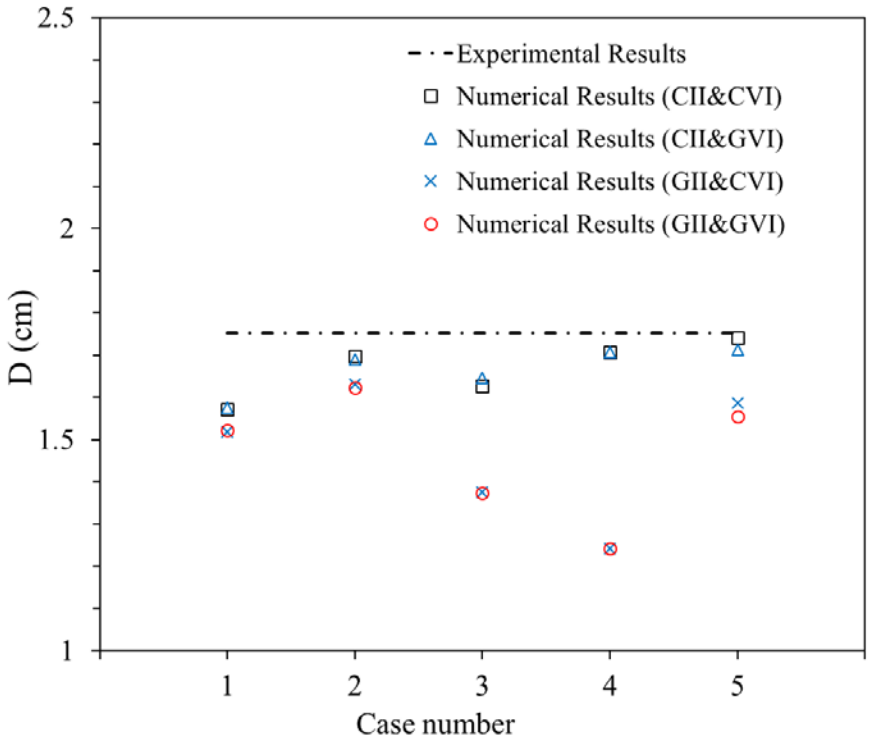

Figure 4.16. Ice thicknesses for five cases and the real measured thickness

4.5 Conclusion

The combination of thermal and visual imaging was investigated. As thermal imaging and visual imaging fail in some situations, using a combination of thermal and visual imaging is a suggestion to eliminate the drawbacks of these two types of imaging. The experimental and numerical results show that using CII in any combination leads to more accurate results than combinations that use GII. The results showed less than 7.5 percent error in the combinations that used CII, which is acceptable.

Chapter 5

Ice Load Measurements on Known Structures

5.1 Introduction

In this part of the thesis, a new method for ice load measurement is developed based on the information of a known structure and image processing results. Most image processing methods are developed based on captured image analyses. In this method, ice loads on structures are calculated by combining structure coordinates and captured image data. Using the structure coordinates and camera parameters, the schematic of the structure is drawn in the image frame. Experiments are performed to capture images and obtain real measured data. Applying the threshold method and a morphological algorithm, the ice area

is extracted from captured images. The ice load on each element of the structure is calculated and the total ice load is then obtained by the summation of the ice loads.

5.2 Methodology

Complex structures are created by a set of elements that are joined to each other. In this method, intersecting nodes of the structure and its connections are defined in a determined coordinate system. This coordinate system is called the world coordinate system. The world coordinate system is converted to the camera coordinate system using extrinsic parameters, including rotation matrix *R* and translation matrix *t*. As explained in chapter 2, these two matrices show the camera position and angle with respect to the world coordinate system. Also, to obtain the structure coordinate in the image plane, intrinsic parameters are calculated using camera calibration. Intrinsic parameters are defined as a matrix *K*, and these include the focal length, image coordinate system origin, and correction parameters. Equation (5.1) shows the conversion of a point P_i from the world coordinate system to point p_i in the image coordinate system using intrinsic and extrinsic parameters [46].

$$p_i = K[R|t]P_i \tag{5.1}$$

Using equation (5.1), each intersecting node P_i of the structure, with coordinates (X_i, Y_i, Z_i) in the world coordinate system, is transformed into an intersecting node p_i with coordinate (x_i, y_i) in the image coordinate system. Furthermore, the connections between the intersecting nodes must be defined in the image plane. Figure 5.1 illustrates the coordinate conversion from a world coordinate system to an image plane coordinate

system. Using this method, the structure is traced in the image plane according to the camera parameters and the structure information without capturing any image. The structure schematic is drawn in a binary image format and is stored as an image.

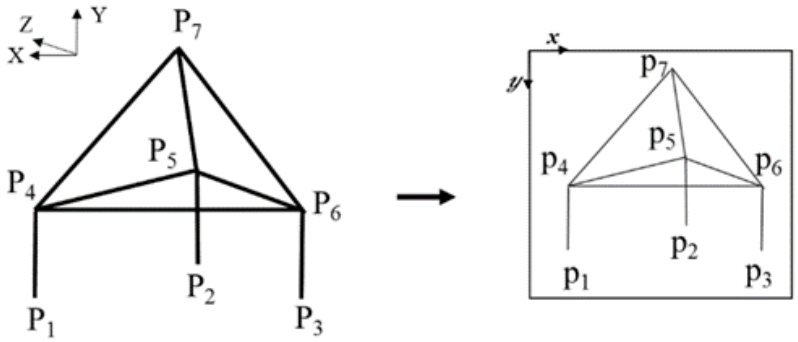

Figure 5.1. Structure coordinate conversion from a 3D to a 2D coordinate system

Images are captured when ice is fully accumulated and stable. RGB images are converted to grayscale images and the Otsu thresholding method is applied on these images to detect the iced structure in the image [30]. This method produces a binary image and assigns a value of 1 for the iced structure and a value of 0 for the background. Some areas that are not the target may appear in the binary image as ice. In order to eliminate these irrelevant areas, the structure schematic in the image plane is employed, and the pixels outside of the structure area are assigned a value of 0. In the next step of ice detection, dilating and eroding morphological operations are applied to fill false gaps and remove small areas created in the binary image. As the block diagram in figure 5.2 illustrates, the results of ice detection are combined with the results of structure detection to calculate the ice thickness for each part of the structure.

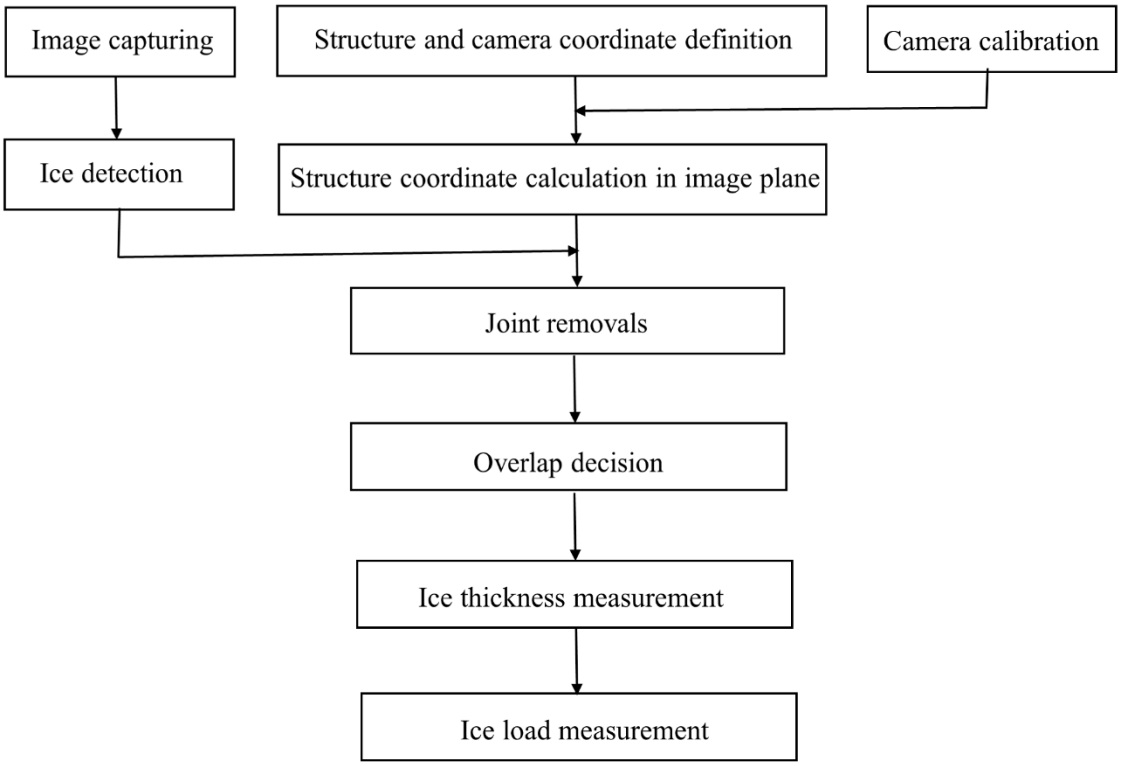

Figure 5.2. Block diagram of ice load measurement on a known structure

Using this method, the ice thickness of each element of the structure must be calculated. To find the ice thickness of each element independently, the joints between the elements of the structure are removed in the binary image using the joint coordinates p_i obtained in the image coordinate system and also by defining a joint removal area. Figure 5.3 shows the settling of ice on a selected part of the structure after removing the joints. The thickness of an iced element r_i is calculated using its detected surface area S_i in the binary image and its length h_i, as shown in equation (5.2). The ice thickness of an element is calculated by subtracting the element thickness r_e in a no ice situation from the thickness of the iced element. These thickness values are obtained according to the number of their pixels. Using the camera parameters, the ice thickness values are converted from the image coordinate

system to the world coordinate system [33]. Employing the calculated ice thicknesses r_i, ice density ρ, element length l, and element radius r_e, the ice load of each element m_i is obtained, as demonstrated in equation (5.3). The total ice load M is calculated by the summation of the calculated element ice loads, as demonstrated in equation (5.4).

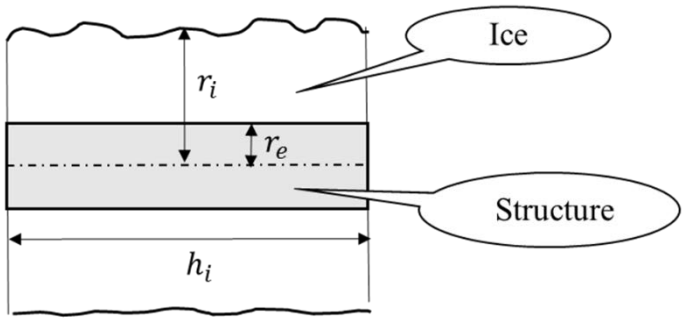

Figure 5.3. Ice accumulated on the structure

$$r_i = \frac{s_i}{2h_i} \tag{5.2}$$

$$m_i = \rho\pi l_i(r_i{}^2 - r_e{}^2) \tag{5.3}$$

$$M = \sum m_i \tag{5.4}$$

This algorithm is able to calculate the ice thickness of elements including overlaps. In the case that two or more elements of the iced structure overlap, they are detected as a single element in the binary image. The detected ice thickness may be larger than or the same as each iced element's thickness. In these cases, the decision concerning how to

calculate ice thickness is made according to the distance between the overlapping elements by setting threshold values.

Three situations are considered to estimate the ice thicknesses of overlapping elements according to their distance from each other: these are a small distance, medium distance, and large distance. In the case that they have a small distance, the detected area is assigned for both of elements; therefore, the same ice thickness is obtained for these two overlapping elements. For a medium distance, the detected ice thickness is larger than the ice thickness of each element. The difference between real thicknesses and detected thicknesses is estimated by the surface area surrounded by the overlapping elements. The ice thickness of each element is estimated by subtracting the surface between these two elements from the measured ice surface area in the binary image. When overlapping elements have a large distance, the detected ice surface is assigned to these elements according to their length. For example, for two overlapping elements with the same length, it is assumed that half of the ice surface belongs to one and a half to another one.

Different ice thicknesses are calculated based on camera positions and angles of its view. Figure 5.4 shows an elliptical cross section of a cylinder covered by ice from three different views. Locating the camera at viewpoint 1, the ice cross section seems to be a circle with a diameter equal to the minor axis of the ellipse D_1. A larger circle with a diameter of D_3 is detected if the camera is located at viewpoint 3. Setting the camera at viewpoint 2, a medium-size circle with diameter D_2 is obtained and its surface area is closer to the ellipse surface area. Calculating different ice thicknesses from different views may cause underestimation or overestimation. The average of the calculated ice thicknesses from different views provides more accurate ice thickness estimations.

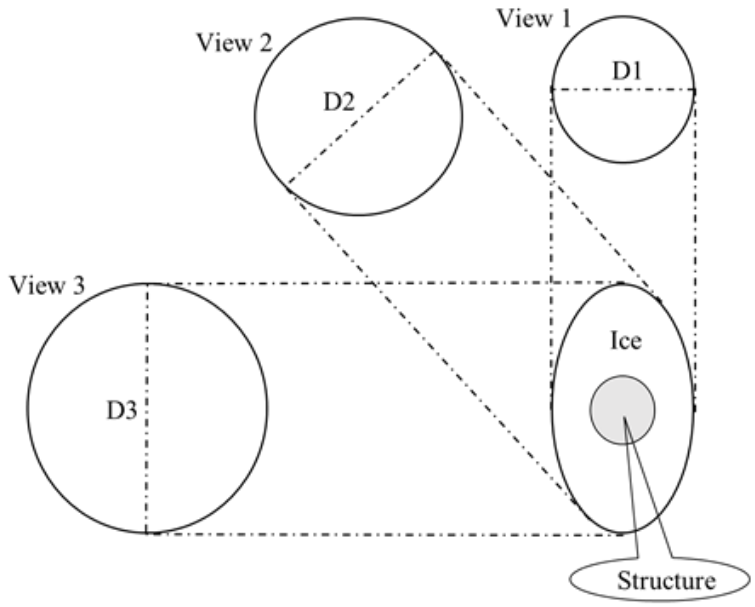

Figure 5.4. The schematic of an iced structure with elliptic cross section from different views

5.3 Experimental Setup

A set of experiments was conducted in a cold room with a temperature of -20 ± 1℃. Nine cylindrical elements with a diameter of 1 cm were welded to form a pyramidal structure. The geometry of this complex structure was known. The length of the legs of the structure was 15 cm and the other bars' lengths were 30 cm. The structure was unsymmetrically covered by saline ice with a salinity of 35‰. The ice accretion procedure was repeated four times to obtain 700 g, 1100 g, 1500 g and 1900 g ice loads on this structure. These ice loads were measured using an accurate digital scale. Figure 5.5 displays the structure covered with different ice loads. Figure 5.5 (a) displays the pyramidal structure with no ice, figure 5.5 (b) and (c) illustrate the iced structure with a 700 g ice load, figure 5.5 (d) and (e) show the iced structure with a 1100 g ice load, figure 5.5 (f) and (g) illustrate

the iced structure with a 1500 g ice load and figure 5.5 (h) and (i) show the iced structure with a 1900 g ice load.

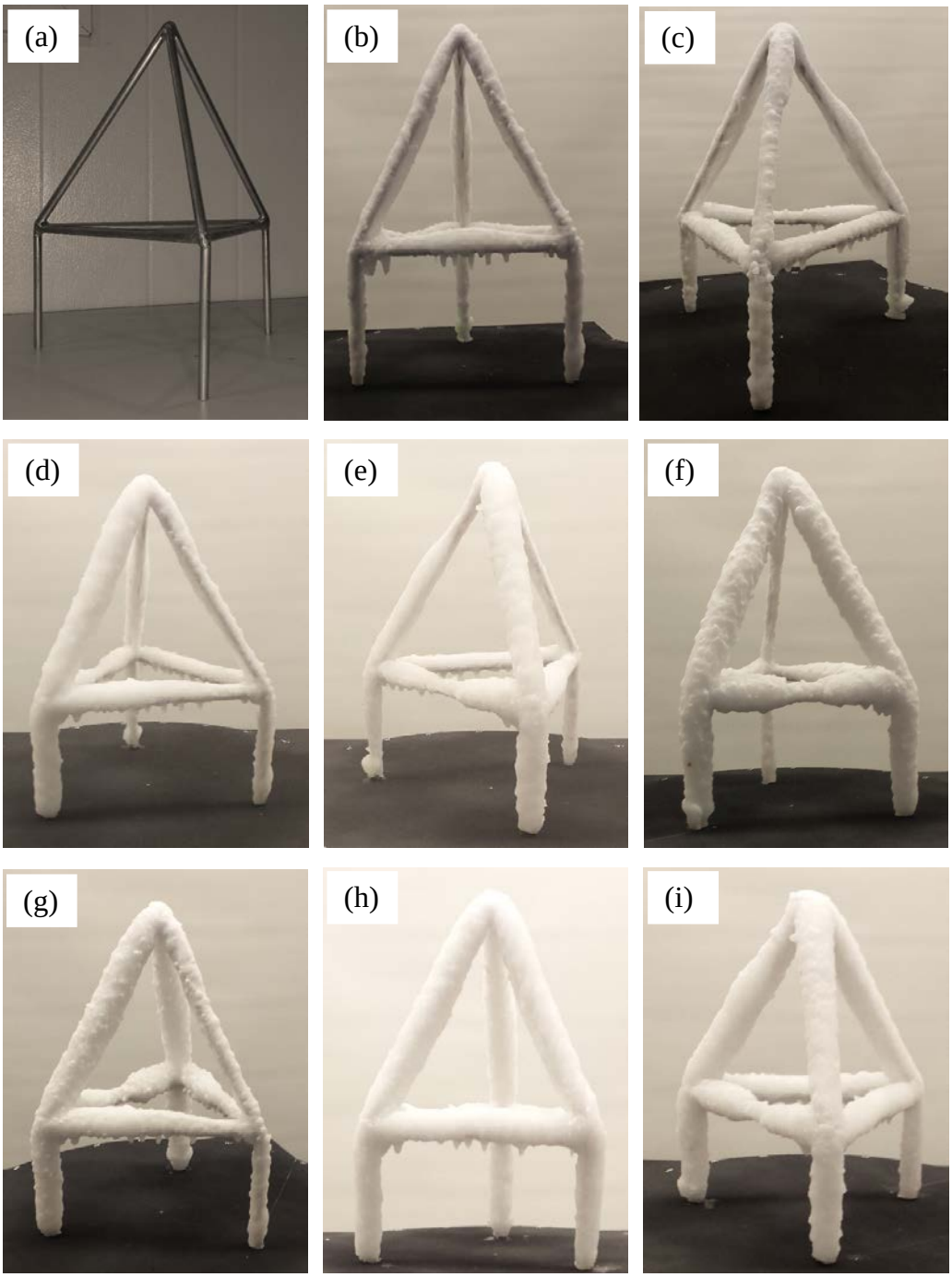

Figure 5.5. The known structure used for experiments

To capture the images of the structure from different views, the structure is located on a circular disk, which is able to rotate around its center in intervals of 15° from 0° to 360° to provide different angles of view. The origin point of the world coordinate system is located at the center of the disk. The structure's intersecting node coordinates and the connection between them are defined with respect to the world coordinate system. The intersecting nodes are P_1(15, 0, -8.37), P_2(-15, 0, -8.37), P_3(15, 15, -8.37), P_4(-15, 15, -8.37), P_5 (0, 15, 16.7), P_6 (0, 0, 16.7), and P_7 (0, 41, 0). All units are given in cm, and the joints and connections between them are shown in figure 5.1 . The camera is located at coordinate points of (100 cm, *Y*, 0) with respect to the center of the disk and with an angle of 0° with respect to the *X*, *Y* and *Z* axes. The camera is moved to six different altitudes, Y: 0 cm, 9 cm, 18 cm, 27cm, 36 cm and 45 cm and the disk rotation provides 24 various views of the structure for camera imaging at each altitude, as in figure 5.6.

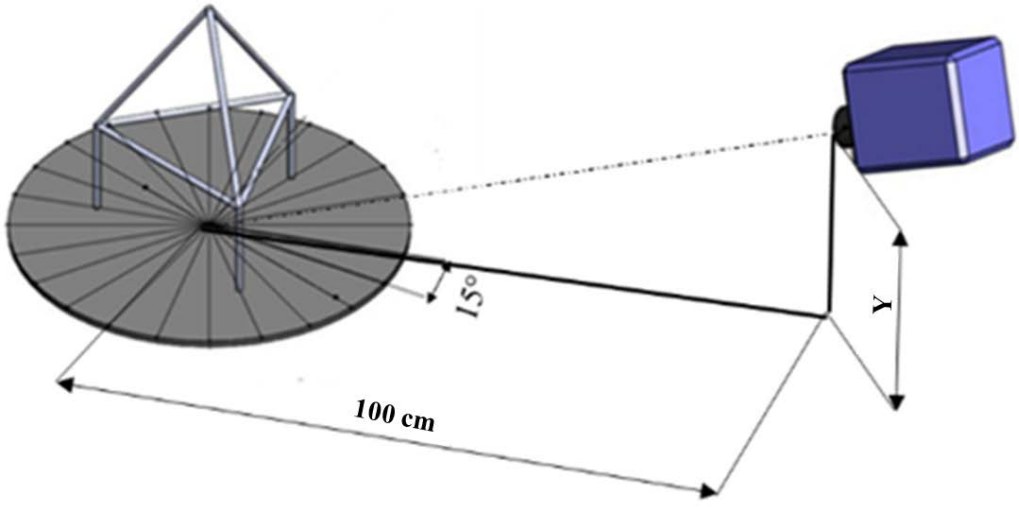

Figure 5.6. A schematic of the experimental setup

5.4 Results and Discussion

The steps described in the methodology section are applied to the captured images to calculate the ice loads on the structure. For each ice load value, 24 angles of view and 6 camera altitudes are investigated. In the following sections, calculated ice load values for four ice loads, 700 g, 1100 g, 1500 g, and 1900 g are discussed.

5.4.1 Results for 700 g Ice Load

Figure 5.7 (b) shows the result of tracing the structure in the image plane according to the camera parameters and the structure information. In this case, the disk is located at an angle of 0°, and the camera is located at a height of 18 cm. A comparison of figure 5.7 (a) and (b) shows a good agreement between the location of the structure in the image and the tracing of the structure in the image plane. The ice is detected using the Otsu thresholding method on the image, which is shown in figure 5.7 (a), and by applying morphological operations. The binary image illustrated in figure 5.7(c) is the result of the ice detection step. Defining the structure's intersecting nodes and connections, the joints between the connected elements are removed to obtain the ice thickness of each element, as shown in figure 5.7 (d). The ice thicknesses of six structural elements are calculated independently and overlaps appear in three elements. Ice thicknesses for overlapping elements are estimated using this method.

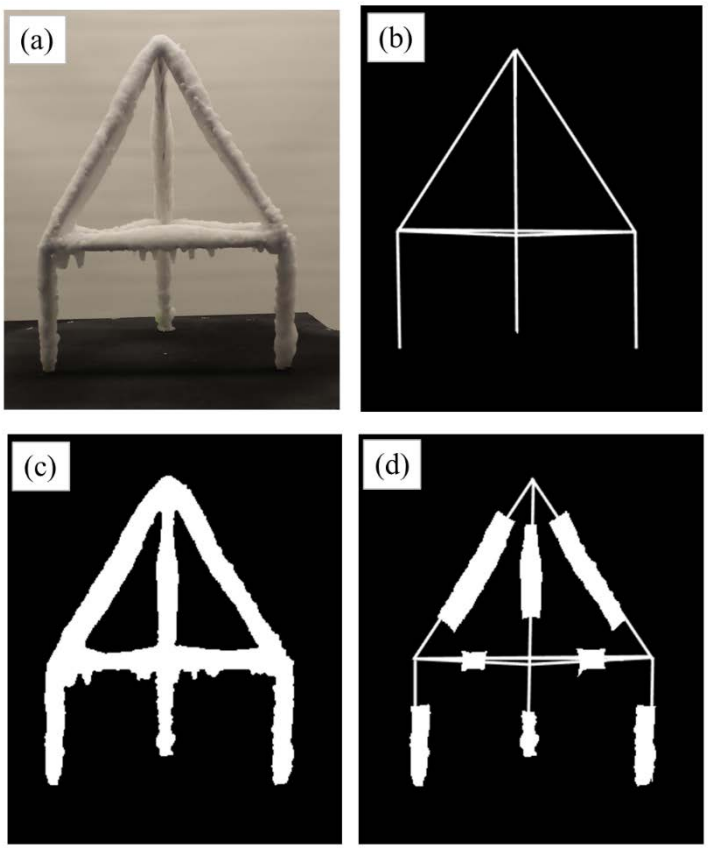

Figure 5.7. Image processing results for M= 700 g and AOV= 0°

Figure 5.8 shows the results of image processing under the condition that the disk is rotated to 30°. In this case, the overlap involves four elements in the binary image. The algorithm calculates ice thicknesses for these four elements by subtracting the area surrounded by elements from the measured ice area. One of the elements appears short in the image; removing the corresponding joints, in this case, leads to eliminating ice detected on this element. The ice thickness of an element with similar properties is assigned as the thickness of this element.

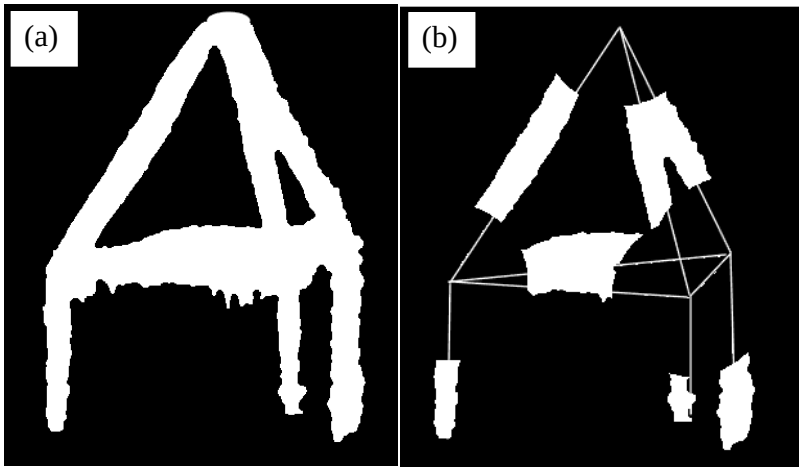

Figure 5.8. Image processing results for M= 700 g and AOV= 30°

Figure 5.9 shows the ice detection and joint movement at an angle of 165°. The ice thicknesses of four elements are calculated independently and the ice thicknesses of other elements are estimated using the proposed method. At this angle, most structural elements are located in the camera's view and have a diameter smaller than the real ice diameter. As a result, underestimation of the ice load is expected.

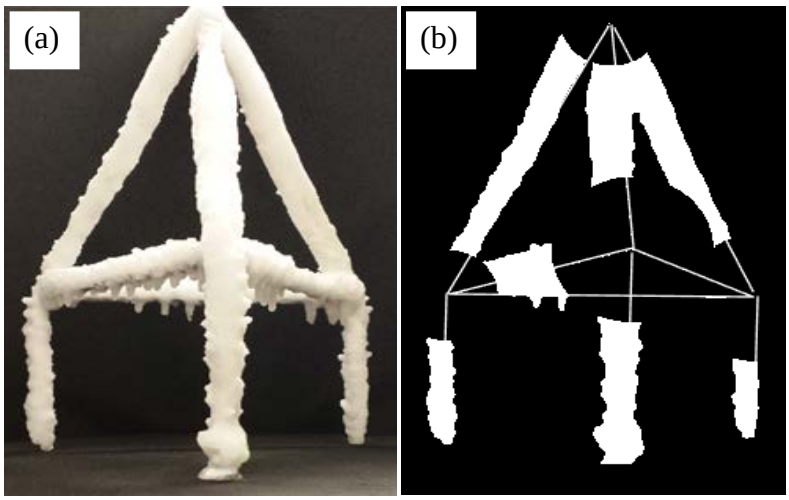

Figure 5.9. Image processing results for M= 700 g and AOV= 165°

Figure 5.10 illustrates the numerical results of the ice load calculated in 24 different views and the actual ice load, which is measured as 700 g using a calibrated scale at an altitude of 18 cm. Calculated ice loads fluctuate around the value of the actual ice load. Ice loads at different angles are mostly calculated with an error of less than 20 percent. Overestimation and underestimation of the calculated ice load appear frequently. This fluctuation is the result of locating structural elements for different camera's views, which is explained in the methodology section. For example, the majority of structural elements are presented in the image frame with their larger diameters at a degree of 240°. At this location, the ice load is calculated as 834 g, which is a high overestimation at this angle. In another case, where the disk is located at 165°, the ice load is calculated as approximately 550 g. This underestimation is due to the smaller diameters of the iced structure appearing in the camera's view. The average of the ice load, obtained at different angles, is 670 g. This result shows coherence between the numerical results and the actual ice load. The average of the calculated ice load is very close to the actual ice load value, with an approximately 4 percent error.

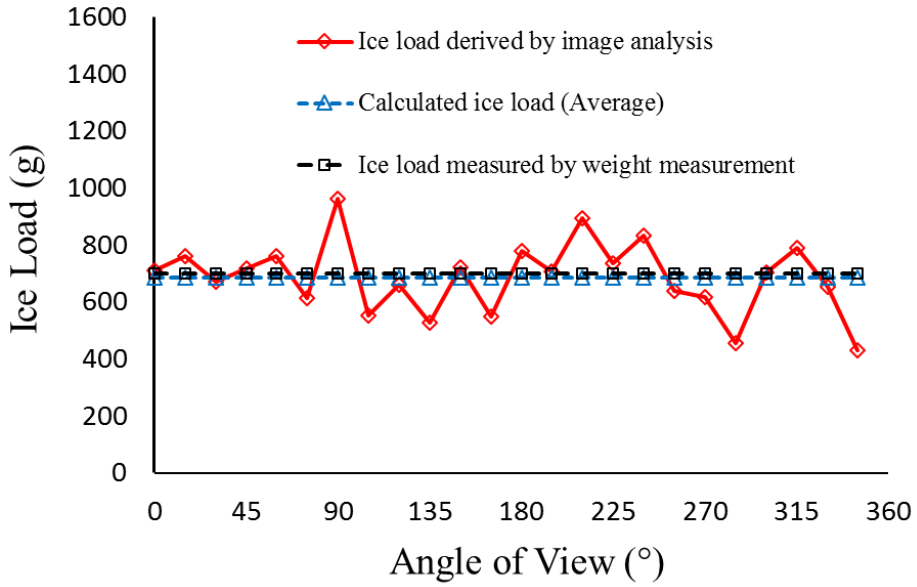

Figure 5.10. Ice load measurements for M= 700 g and Y= 18 cm

Although the disk is rotated to provide 24 points of view, it is not necessary to have this variety of images to measure the ice load of the structure. Table 5.1 demonstrates the calculated ice load for disk rotation at four orthogonal angles 0°, 90°, 180°, and 270°, when the camera is located at a 0 cm altitude. However, overestimations are seen at 90° and 270°, and underestimations at 0° and 180°; the average of the calculated ice load for these four points is very close to the actual ice load value.

Table 5.1. Ice load measurements for M= 700 g and Y= 0 cm

Angle of View (°)	Ice Load (g)
0	660
90	733
180	682
270	792
Average	716.75

5.4.2 **Results for 1100 g Ice Load**

The ice load measurements are obtained for the structure with an 1100 g ice load at 24 angles of view and 6 camera altitudes. Figure 5.11 illustrates the results of the structural trace and ice detection when the camera is located at heights of 0 cm, 18 cm, and 45 cm with no rotation. The results of tracing the structure in the image plane cohere extremely well with the detected iced structure, even when the camera location is changed from one altitude to another. Figure 5.11 (a)-(c) display the structure tracing results when the camera is located at 0 cm,18 cm, and 45 cm and figure 5.11 (d)-(f) display the ice detection results for the camera located at 0 cm,18 cm, and 45 cm.

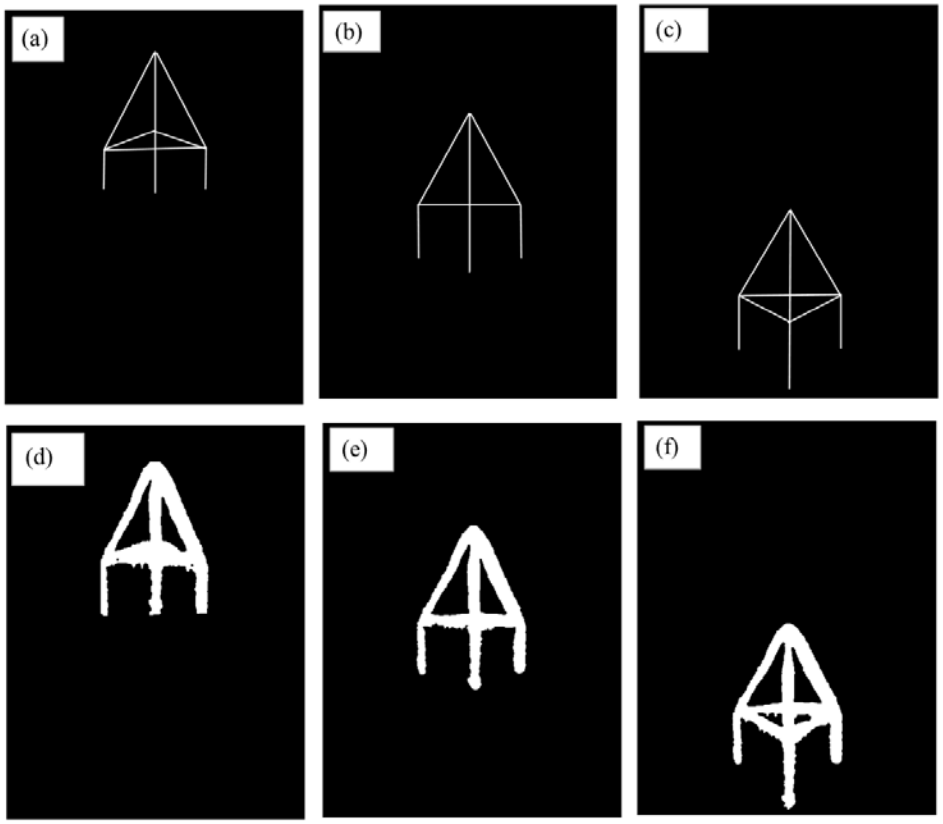

Figure 5.11. Image processing results for M= 1100 g, AOV= 0°, Y= 0, 18, and 45 cm

Figure 5.12 (b) represents the results of ice detection and structure tracing for the iced structure with an 1100 g ice load. The image is captured at a camera altitude of 18 cm and a disk rotation of 315°. In this image, overlaps appear between four elements. As a result of increasing the volume of the accumulated ice on the structure, overlap occures at a shorter distance between the structural elements.

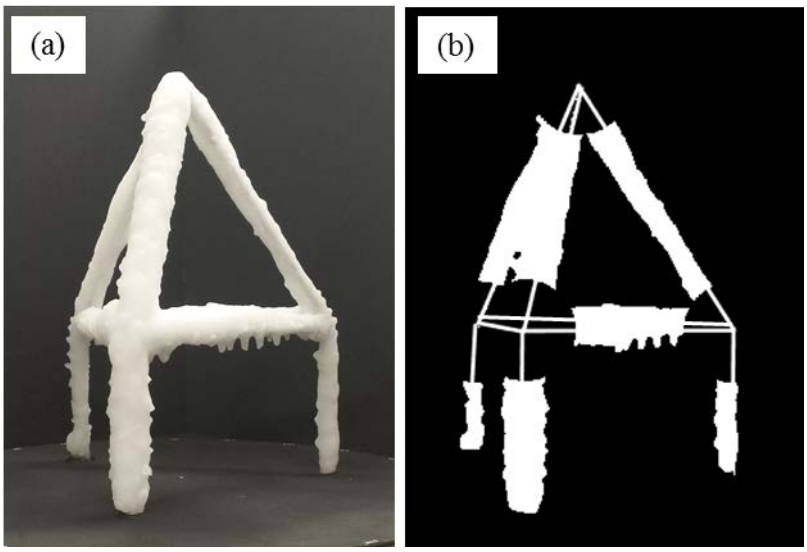

Figure 5.12. Image processing results for M= 1100 g, AOV =315°, and Y=18 cm

Figure 5.13 illustrates the numerical results of the ice load calculated in 24 different views and the actual ice load, which is measured as 1100 g using a calibrated scale. In the majority of the data points, the ice loads are calculated with less than 15% errors. Overestimations and underestimations, occurring due to the camera's point of view, are eliminated in the calculated average ice load from these 24 points of view. The average ice load is obtained as 1174 g and this indicates a less than 6% error in comparison to the real measured ice load of 1100 g.

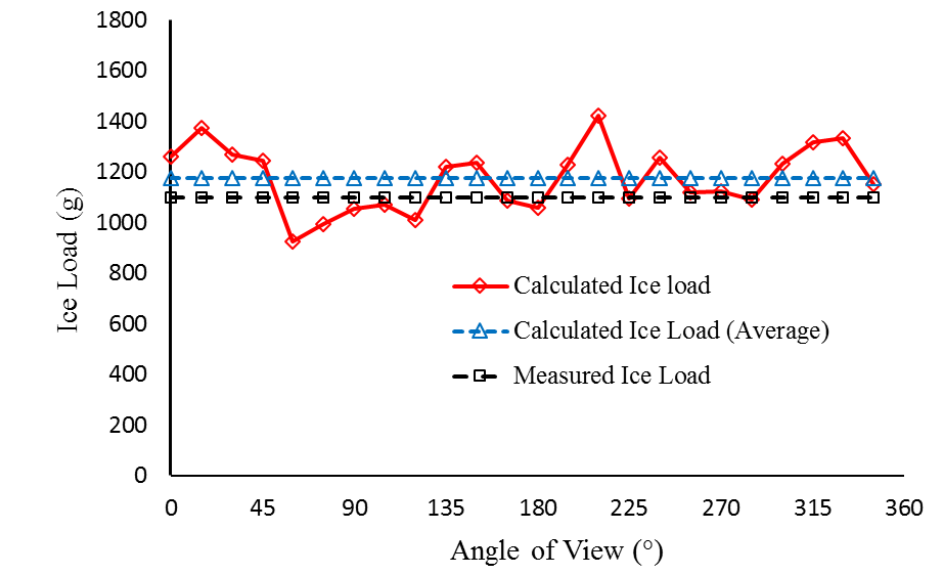

Figure 5.13. Ice load measurements for M= 1100 g and Y= 18 cm

As the ice load is calculated for different camera altitudes, table 5.2 demonstrates the ice load values for the structure with an 1100 g ice load at angles of 0°, 90°, 180°, and 270° and with the camera altitudes of 0 and 36 cm. The values are mostly in an acceptable range of error. Due to changing the camera position, the calculated ice thicknesses at a particular angle may be different at these two altitudes. For instance, at an angle of 270°, when the camera is located at Y equal to 0 cm, the obtained ice load is 878 g, which indicates significant underestimation, while the ice load is calculated as1202 g when the camera is at Y equals 36 cm.

Table 5.2. Ice load measurements for M= 1100 g, Y= 0 and 36 cm

Angle of View (°)	Ice load (g)	
	Y= 0 cm	Y= 36 cm
0	1008	1183
90	1127	1002
180	1059	1029
270	878	1202

5.4.3 **Results for 1500 g Ice Road**

The structure is covered with more ice to produce a 1500 g ice load. Figure 5.14 illustrates the results of image processing for this structure at an angle of 330°, where Y equals 9 cm. As the figure illustrates, the higher volume of ice leads to more overlaps between the structural elements. This factor is considered in the ice thicknesses' calculation to predict what kind of overlap occures.

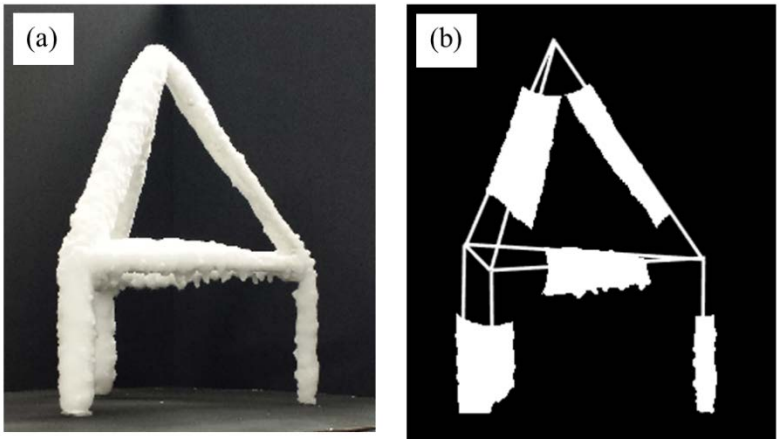

Figure 5.14. Image processing results for M= 1500 g, AOV= 330° and Y= 9 cm

The proposed ice load measurement method is applied to the images, which are captured at different camera altitudes and also at different angle of views. Figure 5.15 displays the calculated ice load fluctuation around the actual ice load, which is 1500 g. In this case, most of the calculated ice load produced errors of less than 10%. As can be seen in the figure, the average calculated ice load is 1495.85 g, which almost matches the actual ice load of 1500 g.

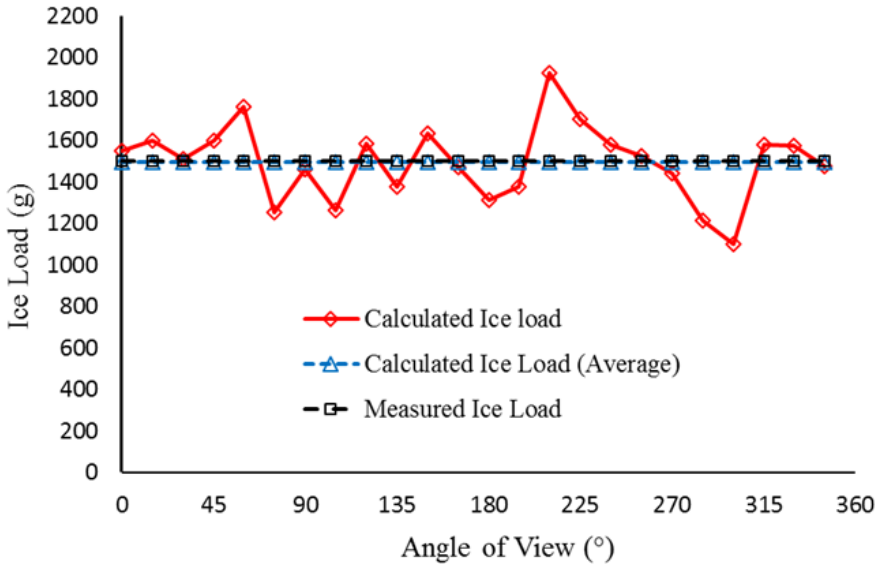

Figure 5.15. Ice load measurements for M=1500 g and Y= 18 cm

As mentioned, it is not necessary to calculate the ice load at all the points of view to achieve accurate results. Table 5.3 shows the calculated ice load when the disk is rotated by an interval of 45°. An acceptable error of about 1.65% occurs when 9 points of view are used to calculate the ice load, while this error is reduced to 0.27% when 24 points of view are imaged. Although increasing the points of imaging may lead to more accurate results, using sufficient points obtains acceptable results.

Table 5.3. Ice load measurements for M= 1500 g and Y= 9 cm

Angle of View (°)	Ice Load (g)	Error (%)
15	1474	1.73
60	1594	-6.26
105	1153	23.1
150	1597	-6.46
195	1503	-0.2
240	1448	3.46
285	1722	-14.8
330	1310	12.66
Average	1475	1.65

5.4.4 **Results for 1900 g Ice Load**

In the last step, the value of the ice load is increased to 1900 g, and images are captured in the same conditions as in the previous experiments. Figure 5.16 (a) displays the structure tracing results, figure 5.16 (b) shows the ice detection results and figure 5.16 (c) illustrates the joint removal results for the image at an angle of 330° when Y equals 45 cm. More accumulated ice on the structure means eliminating more ice detected in the image during the joint removal step. In the case that the dimension of the structure with respect to ice thickness is small, more error may be produced in the ice load calculation.

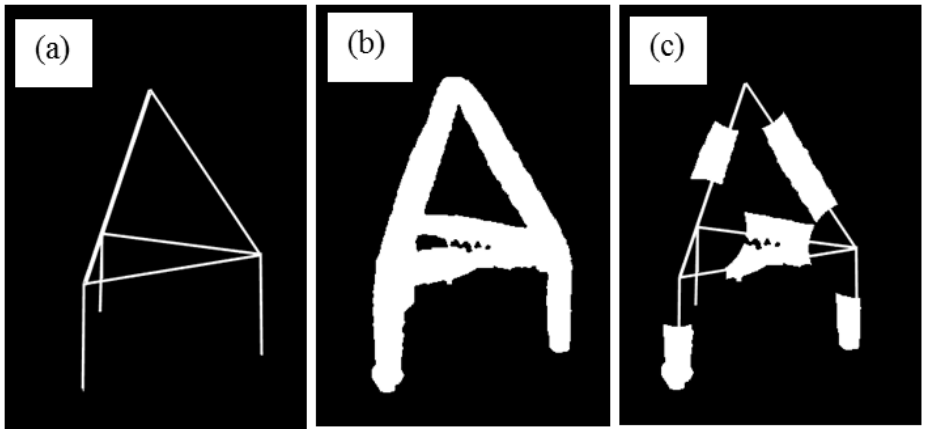

Figure 5.16. Image processing results for M= 1900 g, AOV= 330° and Y= 45 cm

Similar to previous cases, calculated and actual ice load trends according to the angles of view, demonstrated in figure 5.17. Fewer than 20% errors are obtained in most of the points and on average, a 6.45% error is produced in the ice load calculation. Except for two cases of overestimation, which are the results of the false estimation of ice thickness for the

overlapping elements, the other cases are in a good range. The average of the calculated ice obtained load is 1777.33 g.

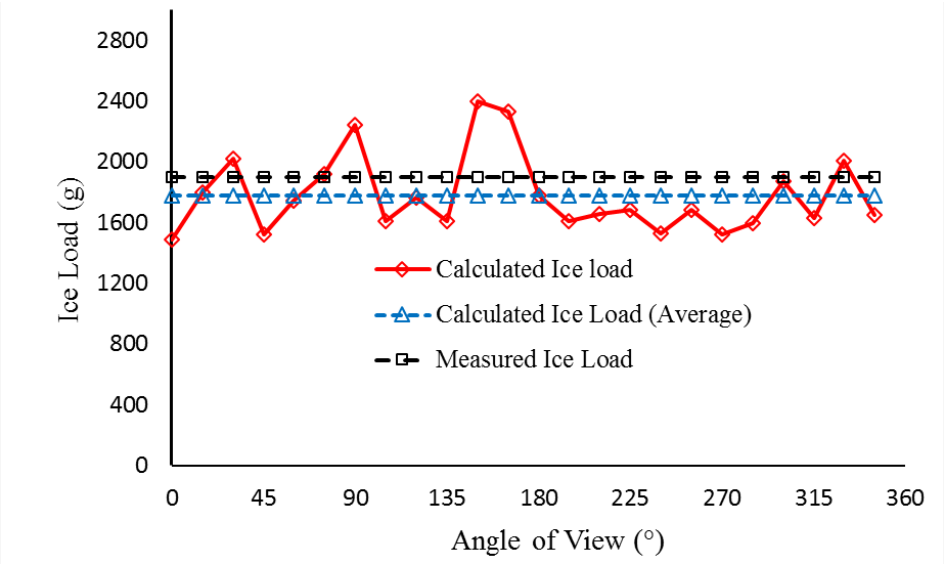

Figure 5.17. Ice load measurements for M= 1900 g and Y= 18 cm

The values of the calculated ice loads at angles of view with an interval of 30° and Y equal to 45 and 18 cm are displayed in table 5.4. According to these data, the ice load calculated is 1777.3 g for the case when the camera is located at an altitude of 18 cm, and this value is 1779.7 g when the camera is at an altitude of 45 cm. Although the calculated ice loads at a similar angle of view and different camera altitudes are different, the average calculated ice loads for both cases are almost the same.

Table 5.4. Ice load measurements for M= 1900 g, Y= 18 and 45cm

Angle of View (°)	Ice load (g)	
	Y= 18 cm	Y= 45 cm
0	1448	1929
30	2018	1698
60	1745	1828
90	2245	1804
120	1767	1903
150	2396	1747
180	1776	1576
210	1657	1585
240	1529	1703
270	1523	1853
300	1870	1897
330	2007	1834
Average	1777.3	1779.7

In another comparison, the ice load values for Y equal to 18, 27 and 45cm at the angles of view 45°, 135°, 210°, and 300° are clarified in table 5.5. In these three cases, most of the ice load values are calculated with less than 20% error, and the average errors are 12.39%, 0.57% and 5.35%. Although the average errors are less than 15%, these differences indicate that selecting proper altitudes and angles may lead to more accurate results.

Table 5.5. Ice load measurements for M= 1900 g, Y= 18, 27 and 45cm

Angle of View (°)	Ice load (g)		
	Y= 18 cm	Y= 27 cm	Y= 45 cm
45	1524	1681	1801
135	1607	1448	1910
210	1657	2610	1585
300	1870	1817	1897
Error	12.39	0.57	5.35

5.6 Conclusion

The ice load accumulated on a more complex structure was calculated using variables including the angle of views and altitude for camera and also the amount of ice load accumulated on the structure. A numerical process was developed for ice detection and ice load measurement on this known structure, applying an image processing method. Overestimation and underestimation in ice thickness measurements occurred due to the camera's angle of view. The majority of the ice load measurements showed a good agreement with the actual ice load value. However, in some cases, about 20 percent error occurred. Calculating the average of the ice loads neutralized the effect of over and underestimation, and the ice load reported had less than a 4 percent error.

Chapter 6

Conclusion and Future Work

6.1 Conclusion

As ice measurement on structures is a challenge in marine industries, in this thesis, image processing methods are developed to calculate ice load on structures. The proposed image processing algorithms are applied on the images obtained from the experimental setups, and the results and their coherence with the actual measurements are discussed in this chapter. Image processing is a technique used in ice thickness measurements in some simple and less complicated scenarios, such as iced power transmissions lines. Thermal and visual cameras are used to record imaging of icing phenomena and videos in order to be analysed. In order to calculate ice load on vessels and offshore structures, which become increasingly complicated when happening in harsh weather conditions, a method is proposed. Based on this new theory, thermal camera are useful and can help to calculate ice loads accurately.

In the first step, in order to calculate ice load on vessels and offshore structures, which becomes increasingly complicated harsh weather conditions, a method is proposed. Based on this method, thermal cameras are useful and can help to calculate ice loads. An experimental setup was used to investigate the effect of ambient conditions such as background colour and light on ice thickness measurements using a thermal camera. The ice thickness of a cylindrical structure was calculated by applying an image processing algorithm on the captured images. Accurate results were obtained for ice thickness using infrared imaging. The results of this expriments illustrated that the background colour and the value of light did not affect the ice measurements when a thermal camera was used, while changing these two parameters influenced ice measurements when a visual camera was used. For example, during the night, a visual camera was not able to capture images suitable for image analysis except when good lighting was available. Ice thicknesses were calculated with high accuracy using the thermal camera, even in the cases with no light and when the background colour was the same as the ice.

In the next step, the combination of thermal and visual imaging was investigated. As thermal imaging and visual imaging fail in some situations, using a combination of thermal and visual imaging is a suggestion to eliminate the drawbacks of these two types of imaging. In this part of the study, two cylinders were used as structures and one of them was used as the main object for which ice thickness was calculated. Combinations of CVI, GVI, CII and GII were used to detect the ice region accumulated on structures. A median filter was applied to images to reduce noise, and at the same time, edges and image pixel values were preserved. The thresholding method based on the collected data was applied to infrared and visual images and the results of thresholding were combined to detect the

ice area. The opening and closing morphological algorithms were used to fill gap areas in the ice region and eliminate narrow white strips that appeared in the image. The ice thickness was calculated counting the number of ice pixels and applying the camera parameters. The experimental and numerical results show that using CII in any combination leads to more accurate results than combinations that use GII. In this study, using CVIs and GVIs in combination had the same results. The applied morphological algorithms changed the boundaries but did not cause a large amount of error when CII was used in the combinations. The results showed less than 7.5 percent error in the combinations that used CII, which is acceptable.

In the next step, a more complex structure was developed. The ice load accumulated on this structure was calculated using variables including the angle of views and altitude for camera and also the amount of ice load accumulated on the structure. A numerical process was developed for ice detection and ice load measurement on this known structure, applying an image processing method. A schematic of the structure was drawn in the image plane using the structure coordinates, camera position and the camera's intrinsic and extrinsic parameters. The images of the iced structure were captured employing a camera located at the position used for tracing the structure schematic. The iced structure was detected in a binary image employing the Otsu thresholding method. As a result, the ice thickness of each element of the iced structure was calculated. Overestimation and underestimation in ice thickness measurements occurred due to the camera's angle of view. The majority of the ice load measurements showed a good agreement with the actual ice load value. However, in some cases, about 20 percent error occurred. Calculating the

average of the ice loads neutralized the effect of over and underestimation, and the ice load reported had less than a 4 percent error.

6.2 Future Work

This section discusses some ideas and recommendations which may be useful for future works to make the results more accurate and applicable in real situations. There are several suggestions that can be lead to improve the results in this research project. Ice detection is one of the steps that needs to be improved in the explained method. As object detection is not the main concern in this research, simple segmenting methods are used to detect the ice area. Concentrating on object detection methods can lead to finding the ice area from the image background with a higher accuracy and also in a complex image scene.

The other recommendations are for ice load measurements on a known complex structure. The structural elements may have overlap, which may add some error to ice load measurements. Introducing models for the different types of overlap that may occur increases the accuracy of the results. Another suggestion is to investigate the optimum points that a camera can be located to capture images in order to reduce the total number of cameras needed. Also, more accurate results can be obtained by applying a thermal camera and even by using a combination of visual and thermal imaging.

References

[1] C. C. Ryerson, “Ice protection of offshore platforms”, *Cold Reg. Sci. Technol.*, vol. 65, no. 1, pp. 97–110, 2011.

[2] A. Bodaghkhani, S.-R. Dehghani, Y. S. Muzychka, and B. Colbourne, “Understanding spray cloud formation by wave impact on marine objects”, *Cold Reg. Sci. Technol.*, vol. 129, pp. 114–136, 2016.

[3] S. R. Dehghani, Y. S. Muzychka, and G. F. Naterer, “Droplet trajectories of wave-impact sea spray on a marine vessel”, *Cold Reg. Sci. Technol.*, vol. 127, pp. 1–9, Jul. 2016.

[4] E. P. Lozowski, K. Szilder, and L. Makkonen, “Computer simulation of marine ice accretion”, *Philos. Trans. R. Soc. London A Math. Phys. Eng. Sci.*, vol. 358, no. 1776, pp. 2811–2845, Nov. 2000.

[5] I. Horjen, “Offshore drilling rig ice accretion modeling including a surficial brine film”, *Cold Reg. Sci. Technol.*, vol. 119, pp. 84–110, 2015.

[6] D. J. Palmer A., “Development of a Marine Icing Monitoring System”, *Proc. 20th*

Int. Conf. Port Ocean Eng. under Arct. Cond., pp. 1–12, 2009.

[7] C. C. Ryerson, “Superstructure spray and ice accretion on a large U.S. Coast Guard cutter”, *Atmos. Res.*, vol. 36, no. 3–4, pp. 321–337, 1995.

[8] C. C. Ryerson, “Assessment of Superstructure Ice Protection as Applied to Offshore Oil Operations Safety: Problems, Hazards, Needs, and Potential Transfer Technologies”, *Erdc/Crrel Tr-08-14*, no. September, p. 156, 2008.

[9] Taimur, H. A. Khawaja, and K. Edvardsen, “Review of marine icing and anti-/de-icing systems”, *J. Mar. Eng. Technol.*, vol. 15, no. 2, pp. 79–87, 2016.

[10] Ocean group Inc., “De-Icing a Cargo Boat”, *Ocean group Inc.*, 2010. [Online]. Available: http://www.groupocean.com/en/achievements/view/21. [Accessed: 02-Aug-2017].

[11] G. Xin and H. Xiaoguang, “On-line monitoring method and observation system of transmission line icing”, *2009 4th IEEE Conf. Ind. Electron. Appl. ICIEA 2009*, pp. 1265–1269, 2009.

[12] X. Wang, J. Hu, B. Wu, L. Du, and C. Sun, “Study on edge extraction methods for image-based icing on-line monitoring on overhead transmission lines”, *2008 Int. Conf. High Volt. Eng. Appl. ICHVE 2008*, pp. 661–665, 2008.

[13] C. Yu, Q. Peng, R. Wachal, and P. Wang, “An image-based 3D acquisition of ice accretions on power transmission lines”, *Can. Conf. Electr. Comput. Eng.*, no. May,

pp. 2005–2008, 2007.

[14] J. Lu, J. Luo, H. Zhang, and B. Li, “An Image Recognition Algorithm Based On Thickness Of Ice Cover Of Transmission Lines”, in *Image Analysis and Signal Processing (IASP)*, 2011, pp. 210–213.

[15] Y. P. Zhong, Q. Zuo, Y. Zhou, and C. Zhang, “A new image-based algorithm for icing detection and icing thickness estimation for Transmission Lines”, *Electron. Proc. 2013 IEEE Int. Conf. Multimed. Expo Work. ICMEW 2013*, 2013.

[16] B. Akbal, “System Design And Implementation To Melt The Ice Occurring In High Voltage Aerial Transmission Lines”, *PhD, Selçuk Univ. Konya, Turkey*, 2015.

[17] M. Shokr and N. Sinha, *Sea ice: physics and remote sensing*. John Wiley & Sons, 2015.

[18] W. G. Rees, *Remote sensing of snow and ice*. CRC press, 2005.

[19] M. Mohseni, M. Frioult, and a Amirfazli, “Simultaneous monitoring of ice accretion and thermography of an airfoil: an IR imaging methodology”, *Meas. Sci. Technol.*, vol. 23, no. 10, p. 105405, 2012.

[20] J. Light, S. Parthasarathy, and W. McIver, “Monitoring winter ice conditions using thermal imaging cameras equipped with infrared microbolometer sensors”, *Procedia Comput. Sci.*, vol. 10, no. Snigm, pp. 1158–1165, 2012.

[21] J. Pasieka, R. Nanua, S. Coulombe, and P. Servio, “The crystallization of sub-cooled

water: Measuring the front velocity and mushy zone composition via thermal imaging", *Int. J. Heat Mass Transf.*, vol. 77, pp. 940–945, 2014.

[22] X. Gong and S. Bansmer, "3-D ice shape measurements using mid-infrared laser scanning", *Opt. Express*, vol. 23, no. 4, pp. 4908–4926, 2015.

[23] J. Casselgren, S. Rosendahl, M. Sjödahl, and P. Jonsson, "Road condition analysis using NIR illumination and compensating for surrounding light", *Opt. Lasers Eng.*, vol. 77, pp. 175–182, 2016.

[24] Z. Long, G. Longde, and Y. Jianjun, "Investigation of ice shape measurement technique based on laser sheet and machine vision in icing wind tunnel", *Proc. 5th Int. Conf. Image Graph. ICIG 2009*, pp. 790–795, 2010.

[25] T. Rashid, H. A. Khawaja, K. Edvardsen, and U. N. Mughal, "Infrared Thermal Signature Evaluation of a Pure and Saline Ice for Marine Operations in Cold Climate", *Sensors & Transducers*, vol. 194, no. 11, p. 62, 2015.

[26] T. Rashid, H. A. Khawaja, K. Edvardsen, and U. N. Mughal, "Infrared Thermal Signature Evaluation of a Pure Ice Block", *International Academy, Research and Industry Association (IARIA)*, 2015.

[27] H. A. K. and K. E. Taimur Rashid, "Ice Detection of Pure and Saline Ice Using Infrared Signature", *IFSA Publ.*, vol. 206, no. 11, pp. 82–87, 2016.

[28] M. Petrou and C. Petrou, *Image processing: the fundamentals*. John Wiley & Sons,

2010.

[29] Z.-Y. Han, D.-H. Gu, and Q.-E. Wu, “Feature Extraction for Colour Images”, in *Electronics, Communications and Networks V*, Springer, 2016, pp. 215–221.

[30] N. Otsu, “A threshold selection method from gray-level histograms”, *Automatica*, vol. 11, no. 285–296, pp. 23–27, 1975.

[31] M. Akhloufi and N. Benmesbah, “Outdoor Ice Accretion Estimation of Wind Turbine Blades Using Computer Vision”, *2014 Can. Conf. Comput. Robot Vis.*, pp. 246–253, 2014.

[32] M. A. Atteya, M. A. M. Salem, D. Abdel, and K. Mohamed, “Image segmentation and particles classification using texture analysis method”, *Research on Biomedical EngineeringAHEAD*, 2016.

[33] R. C. S. Gonzalez and R. E. Woods, *Digital image processing*. Addison-Wesley Publishing Co., 1977.

[34] D. Forsyth and J. Ponce, *Computer vision: a modern approach*. Upper Saddle River, NJ; London: Prentice Hall, 2011.

[35] A. Jayasiri, “Projective geometry and camera calibration”, in *Industrial machine vision lecture*, 2016.

[36] J. R. Martinez-de Dios, B. C. Arrue, A. Ollero, L. Merino, and F. Gómez-Rodríguez, “Computer vision techniques for forest fire perception”, *Image Vis. Comput.*, vol.

26, no. 4, pp. 550–562, 2008.

[37] “MATLAB”, 2016. [Online]. Available: https://www.mathworks.com/help/vision/ug/single-camera-calibrator-app.html. [Accessed: 02-Aug-2017].

[38] “Imagine the Universe”, 2017. [Online]. Available: https://imagine.gsfc.nasa.gov/science/toolbox/emspectrum1.html. [Accessed: 2-Aug-2017].

[39] T. L. Bergman and F. P. Incropera, *Fundamentals of heat and mass transfer*. John Wiley & Sons, 2011.

[40] X. Gong and S. Bansmer, “3-D ice shape measurements using mid-infrared laser scanning”, *Cold Reg. Sci. Technol.*, vol. 115, no. 4, pp. 64–76, 2015.

[41] J. A. Richards, *Remote Sensing with Imaging Radar*. Heidelberg, New York: Springer, 2009.

[42] N. K. Dhar, R. Dat, and A. K. Sood, *Advances in Infrared Detector Array Technology*. Optoelectronics-Advanced Materials and Devices, 2013.

[43] L. Belbin and T. Commonwealth, *User’s Guide ResearchIR*. FLIR Systems, Inc., 2015.

[44] D. Saha, S. R. Dehghani, K. Pope, and Y. Muzychka, “Temperature Distribution during Solidification of Saline and Fresh Water Droplets after Striking a Super-

Cooled Surface", 2016.

[45] R. Hussin, M. R. Juhari, N. W. Kang, R. C. Ismail, and A. Kamarudin, "Digital image processing techniques for object detection from complex background image", *Procedia Eng.*, vol. 41, no. Iris, pp. 340–344, 2012.

[46] E. R. Davies, *Computer and Machine Vision: theory, algorithms, practicalities*. Academic Press, 2012.

Appendix: Publications

Fazelpour, A., Dehghani, S. R., Masek, V., & Muzychka, Y. S. (2017). Ice Load Measurements on Known Structures Using Image Processing Methods. *World Academy of Science, Engineering and Technology, International Journal of Electrical, Computer, Energetic, Electronic and Communication Engineering*, *11*(8), 829-832.

Fazelpour, A., Dehghani, S. R., Masek, V., & Muzychka, Y. S. (2016, October). Infrared image analysis for estimation of ice load on structures. In *Arctic technology conference*. Offshore Technology Conference.

Fazelpour, A., Dehghani, S. R., Masek, V., & Muzychka, Y. S. (2016). Effect of Ambient Conditions on Infrared Ice Thickness Measurement. In *IEEE Newfoundland Section Conference*.

Appendix: Matlab Code

```
tic
clear all
close all
%% Find coordonate of structure in the image coordinate
I1 = imread('20170501_121252.jpg');
b=[-3841.15643946969,0,0;-5.13528418990456,-
3824.73175617788,0;1557.40864199467,2118.22439847314,1]';
[m,n] = size(I1);
n=n/3;
I2=uint8(zeros(m,n));
I4=uint8(ones(m,n));
% I10=uint8(ones(m,n));
 h=[30.5 30.5 15.5 15.5 30.5 29.5 29.5 29.5 15.5];
j1=[15 0 -8.37];
j2=[-15 0 -8.37];
j3=j1+[0.1 15.55 0];
j4=j2+[0.1 15.5 0];
j6=[0 0 16.74];
j5=j6+[.1 15.6 0];
j7=[(j3(1)+j4(1)+j5(1))/3 15.5+(29.5*sin(pi/3)) (j3(3)+j4(3)+j5(3))/3];
jj=[j1;j2;j3;j4;j5;j6;j7];
gama=0;
phi=0;
teta=0;
Ry=[cos(phi*pi/180) 0 sin(phi*pi/180);0 1 0;-sin(phi*pi/180) 0
cos(phi*pi/180)];
j1=Ry*j1';
j2=Ry*j2';
j3=Ry*j3';
j4=Ry*j4';
j5=Ry*j5';
j6=Ry*j6';
j7=Ry*j7';
j1=j1';
j2=j2';
j4=j4';
j3=j3';
j5=j5';
j6=j6';
j7=j7';
```

```
Ry=[1 0 0;0 1 0;0 0 1];
T=[0;15;-100];
T=Ry*T*-1;
a=b*[Ry T];
p1=(1/(j1(3)+T(3))).*a*[j1 1]';
p1=int32(p1);
p2=(1/(j2(3)+T(3))).*a*[j2 1]';
p2=int32(p2);
p3=(1/(j3(3)+T(3))).*a*[j3 1]';
p3=int32(p3);
p4=(1/(j4(3)+T(3))).*a*[j4 1]';
p4=int32(p4);
p5=(1/(j5(3)+T(3))).*a*[j5 1]';
p5=int32(p5);
p6=(1/(j6(3)+T(3))).*a*[j6 1]';
p6=int32(p6);
p7=(1/(j7(3)+T(3))).*a*[j7 1]';
p7=int32(p7);
P1=[p3,p7];
P2=[p7,p4];
P3=[p3,p1];
P4=[p2,p4];
P5=[p7,p5];
P6=[p3,p4];
P7=[p3,p5];
P8=[p5,p4];
P9=[p5,p6];
PP=[P1 P2 P3 P4 P5 P6 P7 P8 P9];
J1=[j3;j7];
J2=[j7;j4];
J3=[j3;j1];
J4=[j2;j4];
J5=[j7;j5];
J6=[j3;j4];
J7=[j3;j5];
J8=[j5;j4];
J9=[j5;j6];
J=[J1 ;J2; J3; J4; J5; J6; J7; J8; J9];
PP=double(PP);
c=zeros(2,9);
s=zeros(1,9);
S=zeros(1,9);
Y=zeros(1,18);
X=zeros(1,9);
sx=(0.000278)*(1/1.03);
for i =1:9
x1=double(PP(1,2*i-1));
y1=double(PP(2,2*i-1));
x2=double(PP(1,2*i));
y2=double(PP(2,2*i));
z(i)=abs((.5*(J(2*i-1,3)+J(2*i,3)))+T(3));
xn = abs(x2-x1);
yn = abs(y2-y1);
c(:,i)=[x2+x1 y2+y1].*.5;
```

```
s(1,i)=(y2-y1)/(x2-x1);
S(1,i)=atan(s(i))*180/pi;
X(1,2*i-1:2*i)=[x1 x2];
Y(1,2*i-1:2*i)=[y1 y2];
if (xn > yn)
    xc = x1 : sign(x2-x1) : x2;
    yc = round( interp1([x1 x2], [y1 y2], xc, 'linear') );
else
    yc = y1 : sign(y2-y1) : y2;
    xc = round( interp1([y1 y2], [x1 x2], yc, 'linear') );
end

linelength(i)=[hypot(x1-x2,y1-y2)];
end
figure
imshow(I1)
figure
imshow(I2)
figure
imshow(rgb2gray(I1)+I2)
%% Ice detection
xmin=min(min(X))-150;
ymin=min(min(Y))-50;
xmax=max(max(X))+150;
ymax=max(max(Y))+50;
for i=1:m
     for j=1:n

             if (i<ymin || i>ymax)

                 I4(i,j)=0;
             end
             if (j<xmin || j>xmax)
                 I4(i,j)=0;
         end
     end
end
I1 = rgb2gray(I1);
level = graythresh(I1);
I3 = im2bw(I1,level);
I3=im2uint8(I3);
I5=I3.*I4;
I3=im2bw(I3);
I5=im2bw(I5);
figure
imshow(I1)
figure
imshow(I3)
figure
imshow(I5)
%
%% Safe area detection
I4=I2;
se1 = strel('disk',10);
```

```
se2 = strel('disk',20);
se3 = strel('disk',10);
I7=imdilate(I5,se1);
figure
imshow(I7)
I7=imerode(I7,se2);
I7=imdilate(I7,se3);
figure
imshow(I7)
p1=double(p1);
p2=double(p2);
p3=double(p3);
p4=double(p4);
p5=double(p5);
p6=double(p6);
p7=double(p7);
safty=300;
for j=1:m
    for i=1:n

        joint1=hypot(p1(1,1)-i,p1(2,1)-j);
        joint2=hypot(p2(1,1)-i,p2(2,1)-j);
        joint3=hypot(p3(1,1)-i,p3(2,1)-j);
        joint4=hypot(p4(1,1)-i,p4(2,1)-j);
        joint5=hypot(p5(1,1)-i,p5(2,1)-j);
        joint6=hypot(p6(1,1)-i,p6(2,1)-j);
        joint7=hypot(p7(1,1)-i,p7(2,1)-j);

if joint3<safty
    I7(j,i)=0;
end
if joint4<safty
    I7(j,i)=0;
end
if joint5<safty
    I7(j,i)=0;
end

if joint7<safty
    I7(j,i)=0;
end
    end
end
figure
imshow(I7)
I2=im2bw(I2);
figure
imshow(I7+I2)
%% Ice thickness measurement
Region1=regionprops(I7,'Area','Orientation','Centroid','BoundingBox','Eq
uivDiameter');
areas=cat(1, Region1.Area);
Region = Region1(areas >7000)
centroids = cat(1, Region.Centroid);
```

```
orientations = cat(1, Region.Orientation);
areas=cat(1, Region.Area);
bound=cat(1, Region.BoundingBox);
for k = 1 : length(Region)
  thisBB = Region(k).BoundingBox;
  rectangle('Position', [thisBB(1),thisBB(2),thisBB(3),thisBB(4)],...
  'EdgeColor','r','LineWidth',2 )
end
N=max(size(areas));
Sn11=zeros(9,9);
Sn22=zeros(9,9);
Sn2=zeros(9,9);
L1=zeros(1,9);
L2=zeros(1,9);
L3=zeros(1,9);
surfacearea=zeros(1,9);
for i=1:9
    for j=1:9
        q=0;
        L(i)=hypot(bound(k(i),4),bound(k(i),3))*cos((abs(teta(i))-
abs(S(i)))*pi/180);
       L3(i)=L(i);
    if k(i)==k(j)
        if i~=j
            for e=1:max(size(xx))
      if bound(k(i),1)<xx(i,e) && xx(i,e)<bound(k(i),1)+bound(k(i),3)
          if bound(k(i),2)<yy(i,e) &&
yy(i,e)<bound(k(i),2)+bound(k(i),4)
         Sn11(i,j)=1

         end
      end


            end
        end
    end

    end
end
for i=1:9
    for j=1:9
      if Sn11(i,j)~=Sn11(j,i)
                Sn22(i,j)=1

      end
    end
end
SnS=zeros(1,9);
SnL=zeros(1,9);
SnM=zeros(1,9);
Sn1=Sn11.*not(Sn22)
Sn2=Sn22.*Sn11
```

```
linelength1=zeros(1,9);
for i=1:9
    for j=1:9
        q=0;
       if Sn1(i,j)==1

        jj=S(i)-S(j);
        if ((-20<jj && jj<-8) || (8<jj && jj<20))

        SnM(i)=1;
        if D(i)<D(j)

       L1(i)=hypot(bound(k(i),4),bound(k(i),3))*cos((abs(teta(i))-
abs(S(i)))*pi/180);
        else

       L1(i)=hypot(bound(k(j),4),bound(k(j),3))*cos((abs(teta(j))-
abs(S(j)))*pi/180);
        end


            l(1,:)=[PP(1,2*i-1) PP(2,2*i-1)];
            l(2,:)=[PP(1,2*i) PP(2,2*i)];
            l(3,:)=[PP(1,2*j-1) PP(2,2*j-1)];
            l(4,:)=[PP(1,2*j) PP(2,2*j)];

             for t=1:4
                for t1=1:4

                    if t1~=t
                        if (l(t,:)-l(t1,:)==0)
                              x1=l(:,1);
                              y1=l(:,2);
                              vi = convhull(l(:,1),l(:,2))
                          surfacearea(i)=polyarea(x1(vi),y1(vi));
                        end

                      end
                    end


             end
             for t2=1:4
                for t22=1:4
                    if t2~=t22
                if (l(t2,:)-l(t22,:)~=0)
                         q=q+1
                          if q>11
                              x1=l(:,1);
                              y1=l(:,2);
                              vi = convhull(l(:,1),l(:,2))
                          surfacearea(i)=polyarea(x1(vi),y1(vi));
```

```
                            end
                    end
                    end
                    end
                end

               linelength1(i)=max(linelength(j),linelength(i));

            end
            if (-8<jj && jj<8)
                SnS(i)=1
                L(i)=L(i);
            end
            if (jj<-20 || jj>20)
                SnL(i)=1
L2(i)=(L(i)+L(j))
L2(j)=(L(i)+L(j))

            end
        end
        end
end

L=L-SnM.*L-SnL.*L+L1+L2;
for i=1:9
   rr(i)=(areas(k(i))/L(i));
  end
SS=(rr.*linelength1)-surfacearea;
for i=1:9
    if linelength1(i)~=0
rc1(i)=SS(i)./linelength1(i);
    else
        rc1(i)=0
    end
end
rrr=(rr+rc1-rr.*SnM);
t=0;
SnA=zeros(1,9);
for i=1:9
    for j=1:9
        if Sn2(i,j)==1
            t=t+1;
            rrr(j)=0
            SnA(j)=1;
        end
    end
end
t=1;
avg=sum(rrr)/(9-t);
rrr=rrr+SnA*avg
 for i=1:9
cylinderthichness(i)=rrr(i)*sx*z(i);
icethickness(i)=((rrr(i)*sx*z(i)))/2;
 end
```

```
%% Ice load measurements
for i=1:9
    m(i)=(pi*h(i)*(icethickness(i)^2))-(pi*h(i)*.25);

end
m=sum(m);
e=(1900-m)*100/1900
toc
```

Ice Load Measurements on Known Structures Using Image Processing Methods

Azam Fazelpour, Saeed R. Dehghani, Vlastimil Masek, Yuri S. Muzychka

***Abstract*—**This study employs a method based on image analyses and structure information to detect accumulated ice on known structures. The icing of marine vessels and offshore structures causes significant reductions in their efficiency and creates unsafe working conditions. Image processing methods are used to measure ice loads automatically. Most image processing methods are developed based on captured image analyses. In this method, ice loads on structures are calculated by defining structure coordinates and processing captured images. A pyramidal structure is designed with nine cylindrical bars as the known structure of experimental setup. Unsymmetrical ice accumulated on the structure in a cold room represents the actual case of experiments. Camera intrinsic and extrinsic parameters are used to define structure coordinates in the image coordinate system according to the camera location and angle. The thresholding method is applied to capture images and detect iced structures in a binary image. The ice thickness of each element is calculated by combining the information from the binary image and the structure coordinate. Averaging ice diameters from different camera views obtains ice thicknesses of structure elements. Comparison between ice load measurements using this method and the actual ice loads shows positive correlations with an acceptable range of error. The method can be applied to complex structures defining structure and camera coordinates.

***Keywords*—**Camera calibration, Ice detection, ice load measurements, image processing.

I. Introduction

STRUCTURE icing is a phenomenon influencing marine and offshore activities during cold seasons in Arctic regions [1]-[3]. Monitoring ice conditions plays an important role to apply de-icing in proper situations. Models have been established to predict the amount of ice load on marine structures [3], [4]. Ice detection and ice load measurements are challenges in marine icing research and have been investigated for years [5]-[7].

Current methods for modeling and measuring ice loads are based on physical properties, which need expensive equipment to be measured, and human interference, which causes safety hazards. Developing algorithms to predict and remove ice accumulation is automatically an essential component to reduce hazards and cost [1]. Image processing techniques have been established for ice monitoring, and are used to calculate the ice thickness on power transmission lines. The ice thickness on transmission lines is calculated applying edge detection and thresholding algorithms. Ice thicknesses are calculated by the subtraction of uniced and iced line thicknesses [8]. In another study, two cameras are employed to capture images of an iced power transmission lines. The matched corresponding points are found in the images establishing correlation methods. The edges of accumulated ice are detected using 3D coordinates obtained from two existing images [9]. The ice thickness of a cylindrical structure is measured employing a thermal camera. Thermal imaging is not affected by background color and light [10]. The combination of visual and thermal imaging is conducted to calculate the ice thickness on a structure and leads to detect the ice area more accurately than using a single type image [11]. Current image based methods can measure ice thickness on simple structures. Ice load measurements based on image processing for complicated structure can provide more advantages for ice monitoring.

In this paper, a method for ice load measurement defining the information of a known structure is developed. Using the structure information and camera position, a scheme of the structure is drawn in the image frame. An experimental setup is performed to capture images and obtain real measured data. Applying the threshold method and a morphological algorithm, the ice area is extracted from captured images. The ice load of each component of the structure is calculated and the total ice load is then obtained by the summation of component ice loads.

II. Methodology

Intersection nodes of the structure and its bar elements are defined in a determined coordinate system. This coordinate system is named the world coordinate system. The world coordinate system is converted to the camera coordinate system using extrinsic parameters, including rotation matrix, R, and translation matrix, t. These two matrices show the camera position and angle with respect to the world coordinate system. To obtain the structure coordinate in the image plane, intrinsic parameters are calculated using camera calibration. Intrinsic parameters are defined as a matrix, K, including focal length, image coordinate system origin, and correction parameters. Equation (1) shows converting a point in the world coordinate system, P_{wc}, to the image coordinate system, p_{ic}, using intrinsic and extrinsic parameters [12].

$$p_{ic} = K[R|t]P_{wc} \quad (1)$$

Using (1), each intersection node of the structure, P_i, with the coordinate of (X_i, Y_i, Z_i) in the world coordinate system is

Azam Fazelpour and Vlastimil Masek re with the Department of Electrical Engineering, Memorial University of Newfoundland, St. John's, NL, Canada (e-mail: a.fazelpour@mun.ca, masek@mun.ca).

Saeed R. Dehghani and Yuri S. Muzychka are with the Department of Mechanical Engineering, Memorial University of Newfoundland, St. John's, NL, Canada (e-mail: srdehghani@mun.ca, yurim@mun.ca).

transformed to p_i with the coordinate of (x_i, y_i) in the image coordinate system. The connections between the intersection nodes are defined in the image plane. Fig. 1 illustrates the coordinate conversion. Using this method, the structure is traced in the image plane according to the camera position and angle without capturing any image. The schemed structure is then restored in a binary format.

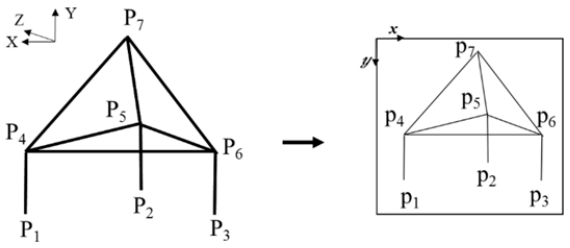

Fig. 1 Structure coordinates conversion from a 3D to a 2D coordinate system

Images are captured when ice is fully accumulated and stable. The Otsu thresholding method is used to detect the iced structure in the image [13]. The result of this method is a binary image with a value of 1 for the iced structure and a value of 0 for the background. As the block diagram in Fig. 2 illustrates, the result of ice detection is combined with the result of structure detection to calculate ice thickness for each part of the structure. Predetermination of the structure coordinates in the image, shown in Fig. 1, helps to remove irrelevant areas detected as ice in the created binary image.

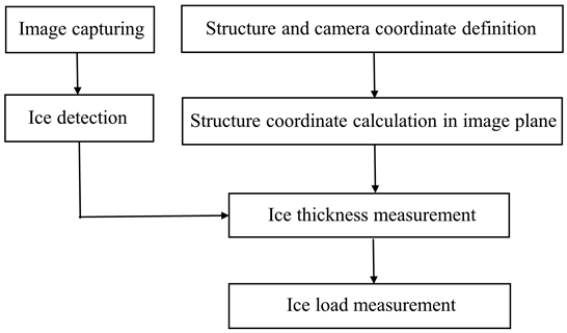

Fig. 2 Block diagram of ice load measurement

To find the ice thickness of each element independently, the data corresponding to the joints between the elements of the structure are removed in the binary image. This occurs using the joint coordinates, p_i, obtained in the image coordinate system. Fig. 3 shows the settling of ice and a selected part of the structure after removing the joints. The thickness of the element, r_i, is calculated using its detected surface area, S_i, in the binary image and its length, h_i which are shown in (2). The thickness values are calculated counting the number of ice pixels. Using camera parameters, the thickness values are obtained in the metric system [14]. Employing the calculated ice thicknesses, ice density, ρ, element length, l, and element radius, r_c, the ice load of each element, m_i, is calculated in (3). The total ice load, M, is concluded by the summation of the calculated element ice loads.

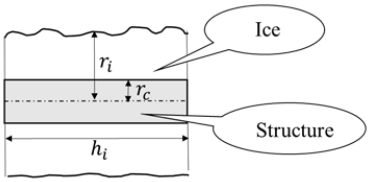

Fig. 3 Ice accumulated on the structure

$$r_i = S_i/2h_i \tag{2}$$

$$m_i = \rho\pi l_i(r_i{}^2 - r_c{}^2) \tag{3}$$

$$M = \sum m_i \tag{4}$$

This algorithm calculates the ice thickness of elements including overlaps. In the case where two elements of the iced structure are detected as a single element in the binary image, the detected ice thickness will be larger than each iced element thickness. The difference between real thicknesses and detected thicknesses is estimated by the surface area surrounded by the elements. Subtracting surface between these two elements from the measured ice surface area in the binary image is used to calculate the ice thickness of elements overlapped.

Different ice thicknesses are calculated based on camera positions and angles of view. Fig. 4 shows an elliptical cross section of a cylinder covered by ice in three different views. Locating the camera in the point view1, the ice cross section seems a circle with a diameter equal to the minor axis of the ellipse, D_1. A larger circle with a diameter of D_3 is detected if the camera is located at point view3. Setting the camera in point view2, a medium-size circle with diameter D_2 is obtained and its surface area is closer to the ellipse surface area. Calculating different ice thicknesses from different views may cause underestimation or overestimation. The average of the calculated ice thicknesses from different views provides more accurate ice thickness estimations.

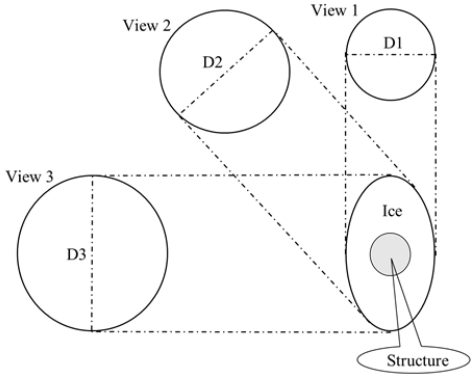

Fig. 4 The schematic of an iced structure with ellipse cross section from different views

III. Experimental Setup

A set of experiments was conducted in a cold room with a

temperature of -20 ± 1℃. Nine cylindrical elements with a diameter of 1 cm are welded to form a pyramidal structure, Fig. 5. The geometry of the complex structure is known. The length of the legs of the structure is 15 cm and the other bars lengths are 30 cm. The structure is unsymmetrically covered by saline ice with a salinity of 35‰. The ice load is measured 700 g using an accurate digital scale.

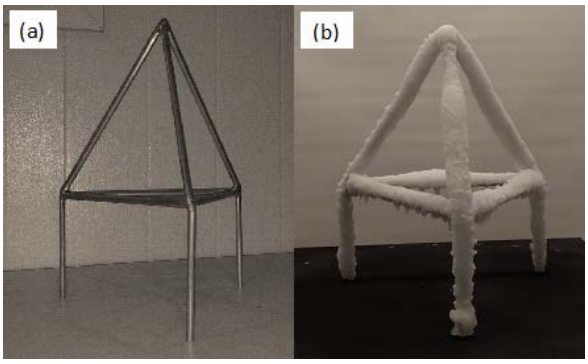

Fig. 5 The known structure used for experiments (a) The pyramidal structure with no ice, (b) The iced structure

The structure is located on a circular disk graded from 0° to 360° to provide different angles of view. The disk is able to rotate around its center in intervals of 15°. The origin point of the world coordinate system is located at the center of the disk. The structure intersection node coordinates and the connection between them are defined with respect to the world coordinate system. The camera is located at a distance of 65 cm and a height of 15 cm with respect to the center of the disk. Disk rotation provides 24 various views of the structure for camera imaging, see Fig. 6.

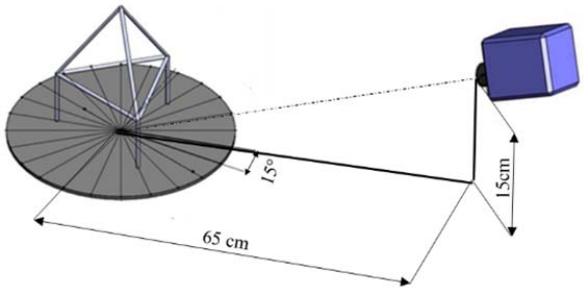

Fig. 6 The schematic of experimental setup

IV. Results and Discussion

The steps described in the methodology section were applied to the captured images to calculate ice loads on the structure. Fig. 7 (b) shows the result of tracing the structure in the image plane according to the camera position and the structure coordinates. In this case, the disk is located at the angle of 0°. Comparison between Figs. 7 (a) and (b) shows a good agreement between the image and the tracing of the structure. The ice area is detected using the Otsu thresholding method on this image by creating a binary image, Fig. 7 (c). Defining the structure coordinate, the joints between connected elements are removed to obtain the ice thickness of each element. The ice thicknesses of six structure elements are calculated independently, while overlaps appear in three elements. Ice thicknesses for elements with overlaps are estimated using this method.

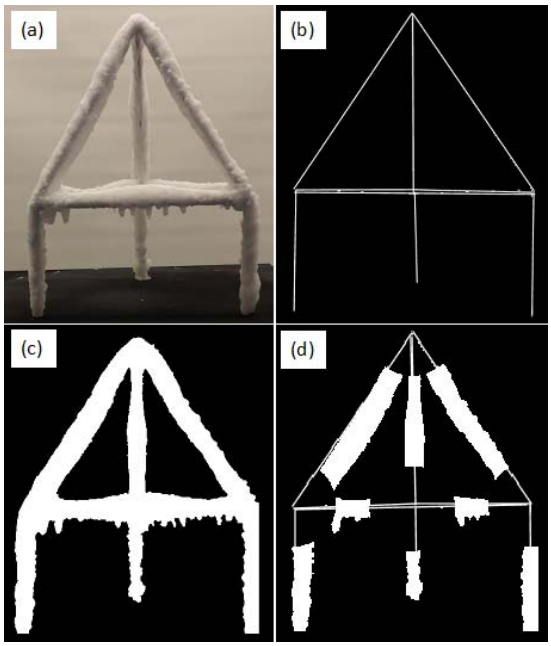

Fig. 7 Image processing results for the structure located at the angle of 0°; (a) Iced structure image, (b) locating structure scheme in the image plane, (c) Ice detection results, (d) Removing the joints using the structure scheme

Fig. 8 shows the results of image processing under the condition that the disk is rotated to 30°. In this case, the overlap involved four elements in the binary image, Fig. 8 (a). The algorithm calculates ice thicknesses for these four elements by subtracting the measured ice area and the area surrounded by elements. One of the elements appears short in the image; removing the corresponding joints in this case leads to eliminating ice detected on this element. The ice thickness of an element with similar properties is assigned as the thickness of this element.

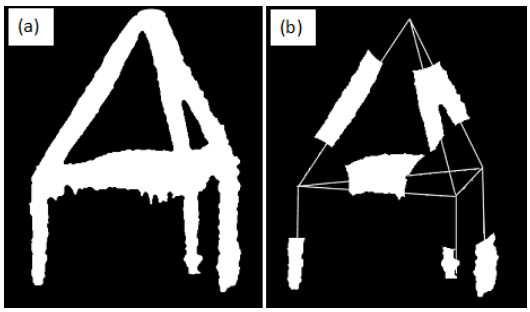

Fig. 8 Image processing results for the structure located at the angle of 30°; (a) Ice detection results, (b) Removing the joints using the structure scheme

Fig. 9 shows the ice detection and joint movement at the

angle of 165°. The ice thicknesses of four elements are calculated independently and ice thicknesses of other elements are estimated using the proposed method. At this angle, most structure elements are located in the camera view with a smaller ice diameter. As a result, underestimation of ice load calculation is expected.

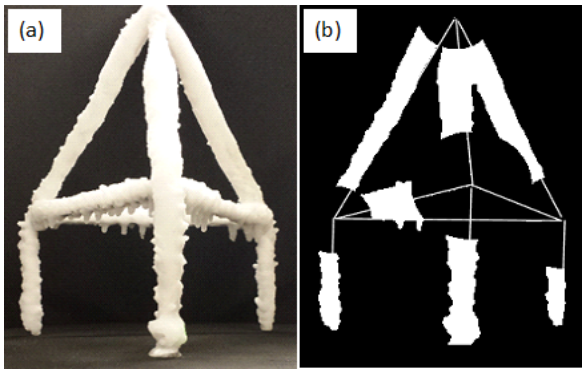

Fig. 9 Image processing results for the structure located at the angle of 165°; (a) Ice detection results, (b) Removing the joints using the structure scheme

Fig. 10 illustrates the numerical results of the ice load calculated in different 24 views and the actual ice load which is measured 700 g using a calibrated scale. Calculated ice loads fluctuate about the value of the actual ice load. Ice loads in different angles are mostly calculated with an error less than 20 percent. Overestimation and underestimation of the calculated ice load appear frequently. This fluctuation is the result of locating structure elements in different camera views, which is explained in the methodology section. For example, the majority of structure elements are presented in the image frame with their larger diameters at the location of 240°. At this location, the ice load is calculated 834 g, which is high overestimation at this angle. In another case, where the disk is located at 165°, the ice load is calculated approximately 550 g. This underestimation is due to appearing smaller diameters of the iced structure in the camera view. The average of ice load obtained at different angles is 670 g. This result shows a good agreement between the numerical results and the actual ice load. The average of calculated ice load is very close to the actual ice load value with an approximately 4 percent error.

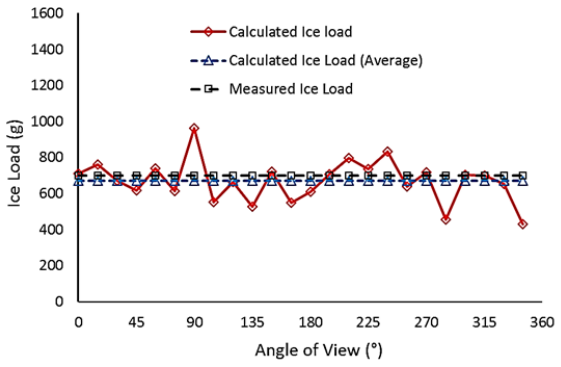

Fig. 10 Comparison between the calculated and measured ice loads

V. Conclusion

A numerical process is developed for ice detection and ice load measurement on a known structure applying an image processing method. A scheme of the structure is drawn in the image plane using the structure coordinates, camera position, and camera intrinsic and extrinsic parameters. The images of the iced structure are captured employing a camera located at the position used for tracing the structure schematic. The iced structure is detected in a binary image considering the Otsu thresholding method. As a result, the ice thickness of each component of ices structure is calculated. Overestimation and underestimation in ice thickness measurements occur due to the camera angle of view. The majority of the ice load measurements show a good agreement with the actual ice load value. However, in some cases, about 20 percent error occurs. Calculating the average of the ice loads neutralize the effect of over and underestimation, and the ice load is reported with less than 4 percent error.

Acknowledgment

The authors gratefully acknowledge the financial support from Statoil (Norway), MITACS, Petroleum Research Newfoundland and Labrador (PRNL) and ABS for this research.

References

[1] C. C. Ryerson, "Ice protection of offshore platforms," *Cold Reg. Sci. Technol.*, vol. 65, no. 1, pp. 97–110, 2011.
[2] A. Bodaghkhani, S.-R. Dehghani, Y. S. Muzychka, and B. Colbourne, "Understanding spray cloud formation by wave impact on marine objects," *Cold Reg. Sci. Technol.*, vol. 129, pp. 114–136, 2016.
[3] A. R. Dehghani-Sanij, S. R. Dehghani, G. F. Naterer, and Y. S. Muzychka, "Sea spray icing phenomena on marine vessels and offshore structures: review and formulation," *Ocean Eng.*, vol. 132, pp. 25–39, 2017.
[4] E. P. Lozowski, K. Szilder, and L. Makkonen, "Computer simulation of marine ice accretion," *Philos. Trans. R. Soc. London A Math. Phys. Eng. Sci.*, vol. 358, no. 1776, pp. 2811–2845, Nov. 2000.
[5] C. C. Ryerson, "Superstructure spray and ice accretion on a large U.S. Coast Guard cutter," *Atmos. Res.*, vol. 36, no. 3–4, pp. 321–337, 1995.
[6] C. C. Ryerson, "Assessment of Superstructure Ice Protection as Applied to Offshore Oil Operations Safety: Problems, Hazards, Needs, and Potential Transfer Technologies," *Erdc/Crrel Tr-08-14*, no. September, p. 156, 2008.
[7] D. J. Palmer A., "Development of a Marine Icing Monitoring System," *Proc. 20th Int. Conf. Port Ocean Eng. under Arct. Cond.*, pp. 1–12, 2009.
[8] X. Wang, J. Hu, B. Wu, L. Du, and C. Sun, "Study on edge extraction methods for image-based icing on-line monitoring on overhead transmission lines," *2008 Int. Conf. High Volt. Eng. Appl. ICHVE 2008*, pp. 661–665, 2008.
[9] C. Yu, Q. Peng, R. Wachal, and P. Wang, "An image-based 3D acquisition of ice accretions on power transmission lines," *Can. Conf. Electr. Comput. Eng.*, no. May, pp. 2005–2008, 2007.
[10] A. Fazelpour, S. R. Dehghani, V. Masek, and Y. S. Muzychka, "Effect of Ambient Conditions on Infrared Ice Thickness Measurement," in *IEEE Newfoundland Section Conference*, 2016.
[11] A. Fazelpour, S. R. Dehghani, V. Masek, and Y. S. Muzychka, "Infrared Image Analysis for Estimation of Ice Load on Structures," in *Arctic Technology Conference*, 2016.
[12] E. R. Davies, *Computer and Machine Vision: Theory*. 2012.
[13] N. Otsu, "A threshold selection method from gray-level histograms," *Automatica*, vol. 11, no. 285–296, pp. 23–27, 1975.
[14] R. C. S. Gonzalez and P. Wintz, "Digital image processing," 1977.

OTC-27409-MS

Infrared Image Analysis for Estimation of Ice Load on Structures

Azam Fazelpour, Department of Electrical Engineering, Memorial University of Newfoundland; Saeed R. Dehghani, Department of Mechanical Engineering, Memorial University of Newfoundland; Vlastimil Masek, Department of Electrical Engineering, Memorial University of Newfoundland; Yuri S. Muzychka, Department of Mechanical Engineering, Memorial University of Newfoundland

This paper was prepared for presentation at the Arctic Technology Conference held in St. John's, Newfoundland and Labrador, 24-26 October 2016.

Abstract

An analysis using infrared and visual images is made to measure the ice thickness of a cylindrical component. The proposed method is useful for ice detection and measurement on structures, even in harsh conditions and low light situations such as night. This type of analysis can fill a gap of knowledge related to ice measurement using both visual and thermal images. Thermal imaging shows differences in the emissivity and temperature of objects. This can help to detect objects and measure the amount of ice accumulated on the objects. Combining the information of visual and thermal images can compensate for their weak points and present better results. Combinations of the color-visual image (CVI), grayscale-visual image (GVI), color-infrared image (CII) and grayscale-infrared image (GII) are used to find the most accurate results. A binary image is acquired using the threshold method based on data collected from infrared and visual images. Using threshold levels removes irrelevant data that come from the background. Common ice pixels detected from both infrared and visual images are considered as the ice area. Thresholding methods cause unwanted gaps and strips in binary images. Morphological algorithms are used to remove these imperfections. The best results are obtained when one of the elements of the combinations is CII. The results of using CVI and GVI are almost the same. The experiments show that this method is reliable and its results are aligned with the real data.

Introduction

Marine and offshore structures are faced with severe icing during cold seasons in Arctic regions (Horjen, 2015; Ryerson, 2011). Ice accumulates from periodic wave-impact sea spray caused by wave breakup and the cold substrates of structures (Bodaghkhani et al., 2016; Dehghani et al., 2016). Some models have been developed to predict the amount of ice load on the marine structures (Lozowski et al., 2000). Detection and measurement of ice loads are other challenges of this field of research and have been investigated for many years (Palmer A., 2009; Ryerson, 2008, 1995).

Monitoring iced structures in harsh weather has been a lasting major challenge. It is very important to develop algorithms to automatically monitor icing situations including icing detection and ice load estimations (Roebber and Mitten, 1987; Ryerson, 2008). There have been some methods, based on visual

image processing, developed for ice monitoring in different situations. The edge of iced objects is detected using different threshold methods. Comparing the boundary of ice and structure yields the calculation of ice thickness. Using wavelet-transform and floating-threshold methods is effective to calculate the thickness of smooth ice. On the other hand, the combination of the optimal threshold and the morphological algorithm is effective in the detection of complex ice edges (Wang et al., 2008). For transmission lines, the information of ice intensities and locations in no ice situations is used to improve the edge detection during the measurement of ice thickness. When transmission lines drift, using this information leads to the accurate calculation of ice thickness (Zhong et al., 2013). Another example of using images for measuring the accumulated ice on power transmission lines involves two cameras being used to capture images of an iced power transmission line. The corresponding points are matched in these two images using correlation methods. Ice edges are detected using 3D coordinates obtained from two images (Yu et al., 2006). For icing in wind tunnels, a system of ice shape measurements is developed using the laser sheet and image processing technique. A camera detects the backscattered light that ice reflects after reaching the laser scattering. This method measures the ice shape with a high accuracy (Long et al., 2009).

Thermal images reveal differences in the emissivity and temperature of objects and provide a good opportunity to detect ice from the background. The cold objects that have a temperature close to the freezing point of ice emit energy in a range that most commercial infrared sensors record. Therefore, infrared thermography can be useful for ice surface studies (Rees, 2005). There are some works which use thermal cameras to monitor ice conditions and ice detection. For example, an infrared camera is used to monitor the surface temperature of energized airfoils and to measure the ice accretion on the airfoil in a wind tunnel. In addition, the effect of ice accumulation on the temperature of airfoils is revealed using a thermal camera (Mohseni et al., 2012). In another example, a thermal camera is used to monitor snow cover and ice conditions in winter. The real time ice condition is determined by classifying captured infrared images (Light et al., 2012). Thermal cameras can be used for capturing the process of freezing (Pasieka et al., 2014). In this study, the front velocity of sub-cooled water when water freezes is studied. An infrared camera is used to monitor the steps for freezing. Four images of sub-cooled water are captured several times to monitor the velocity of the thermal front. Results of using the infrared camera agree with the results obtained using other methods (Pasieka et al., 2014). An infrared camera and mid- infrared laser scanning can be used to measure a 3D ice shape without considering the type of ice. The results of 3D measurement using this method show that they are in good agreement with the results acquired by a visual camera (Gong and Bansmer, 2015). A lab experiment is performed to detect the variation of the temperature of ice using an infrared camera to analyze thermal signatures of saline and fresh water ice. The behavior of fresh water and saline ice with different temperatures is observed using a thermal camera. However, falsely detected information is still a concern (Rashid et al., 2015a, 2015b). Different road conditions such as snowy, icy, wet and dry are distinguished using an infrared camera and illuminated with a near-infrared laser. Using three different near-infrared laser wavelengths leads to classifying various road conditions with higher accuracy (Casselgren et al., 2016).

In this paper, a new method is developed for ice load measurement using the combination of infrared and visual images. An experimental setup is performed to capture infrared and visual images and obtain real measured data. Using the threshold method and a morphological algorithm, ice is extracted. The method is applied to grayscale and color images and ice thicknesses are measured using four combinations of color and grayscale images.

Theory and Methodology

Measuring the intensity of ice at various points of the target object and organizing the data occur in the stage of data collection. Data collections are performed to define ice intensity ranges in infrared and visual images using the infrared and visual images taken. Iced structures are located in different positions and angles to

simulate all possible cases with different behavior. CVIs and CIIs are converted to the RGB format, and consequently, pixels in these images include red, green and blue components. Three intensity ranges are obtained for CVIs and CIIs and one intensity range is provided for GVIs and GIIs. Ice pixel ranges for images are found using ice histograms and checking ice pixel values, which are formulated in Eqs. (1–4). These intensity ranges, which are acquired in this step, provide threshold levels that will be used for ice detection.

$$I_{Lk} \le I_k(i,j) \le I_{Hk} \qquad k = R, G \text{ and } B \tag{1}$$

$$I'_{Lk} \le I'_k(i,j) \le I'_{Hk} \qquad k = R, G \text{ and } B \tag{2}$$

$$I_{Lg} \le I_g(i,j) \le I_{Hg} \tag{3}$$

$$I'_{Lg} \le I'_g(i,j) \le I'_{Hg} \tag{4}$$

After data collection, several steps are needed to obtain the ice thickness value. Figure 1 shows the steps that lead to ice thickness measurements. Preprocessing includes image resampling and noise reduction is applied to visual and infrared images in the first step. In our experiments, the resolution of infrared images is less than that of visual images. Therefore, the infrared and visual images should be converted to the same image size to be able to combine the information correctly. Image resampling is performed for the infrared image to obtain the same size as the visual image. Some noise is generated in the visual image and filtering is performed to reduce noise in the image before the object detection. The median filter is chosen to remove the noise while the edge of the ice is preserved.

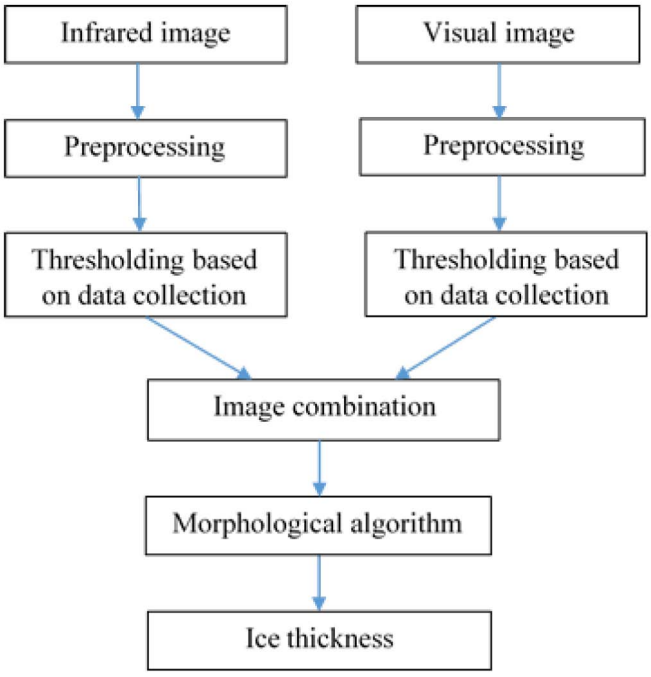

Figure 1—Block diagram of ice thickness measurement

In the next step, threshold levels, obtained from Eqs. (1–4), are used to classify images into the background and ice area categories. Pixels that do not belong to the ice intensity range are eliminated and replaced by the value of 0, the ice pixels are valued as 1 and a binary image is formed (Hussin et al., 2012). Four binary images are obtained by thresholding CVIs, CIIs, GVIs and GIIs. Using the AND function for the combination of four binary images provides four new binary images that contain the information of both infrared and visual images. The first binary image is created by the combination of the thresholded CII and

the thresholded CVI and shown as $I_{c1}(i, j)$. The second binary image is obtained using the thresholded CII and the thresholded GVI with the name of $I_{c2}(i,j)$. The third binary image is defined using the combination of thresholded CVI and the thresholded GII and defined as $I_{c3}(i,j)$. The combination of the thresholded GVI and the thresholded GII creates a binary image with the notation of $I_{c4}(i,j)$. Eqs. (5–8) formulate all the mentioned combinations.

$$I_{c1}(i,j) = \begin{cases} 1 & I_{Lk} \le I_k(i,j) \le I_{Hk} \text{ and } I'_{Lk} \le I'_k(i,j) \le I'_{Hk} \quad k = R, G \text{ and } B \\ 0 & \text{Otherwise} \end{cases} \tag{5}$$

$$I_{c2}(i,j) = \begin{cases} 1 & I_{Lk} \le I_k(i,j) \le I_{Hk} \text{ and } I'_{Lg} \le I'_g(i,j) \le I'_{Hg} \quad k = R, G \text{ and } B \\ 0 & \text{Otherwise} \end{cases} \tag{6}$$

$$I_{c3}(i,j) = \begin{cases} 1 & I_{Lg} \le I_g(i,j) \le I_{Hg} \text{ and } I'_{Lk} \le I'_k(i,j) \le I'_{Hk} \quad k = R, G \text{ and } B \\ 0 & \text{Otherwise} \end{cases} \tag{7}$$

$$I_{c4}(i,j) = \begin{cases} 1 & I_{Lg} \le I_g(i,j) \le I_{Hg} \text{ and } I'_{Lg} \le I'_g(i,j) \le I'_{Hg} \\ 0 & \text{Otherwise} \end{cases} \tag{8}$$

The lack of collected data may cause black gaps in the ice area of binary images. Also, the same intensity values of the background and ice area cause the creation of some small white strips, which are connected to the ice area. Morphological image processing algorithms are used to correct or remove imperfect areas which are obtained by the threshold method. The closing morphological algorithm removes small black areas, which are surrounded by the ice area. The opening morphological algorithm is used to eliminate white strip areas.

In order to calculate a pixel size in the real world coordinate system, a camera calibration is performed to measure each pixel size using the software which belongs to the thermal camera. The iced surface area is calculated using the multiplication of the calculated pixel size and the number of ice pixels, which is determined from the binary image. The ice surface is assumed to be rectangular; its width is the iced structure diameter and its length is the structure length. Ice thicknesses are measured by subtracting the structure thicknesses from the iced structure thicknesses (Wang et al., 2008).

Results and Discussion

Experiments are conducted in a cold room which has a temperature of −20 ± 1°C. A cylindrical component with an outer diameter of 4 cm, covered by saline ice with a salinity of 35‰, is used as the target object of image processing. Another cylinder, which acts as part of the background, is covered by fresh water ice to represent old ice, which has lower salinity, or ice located far from the target cylinder. The size of the background cylinder is the same as the target cylinder. This cylinder is located behind the first cylinder. The wall of the cold room, which is behind the cylinders, acts as the rest of the background. Two cylindrical components are placed in five different angles and arrangements that make five different cases in this research. The camera is located at a distance of 1.45 m to the front object during the imaging. The camera calibration is performed using infrared camera software, the distance of the camera to the front object and also by defining a real dimension value on the object in the software.

The specified steps in the methodology are used to extract and measure the ice thickness. Four combinations of visual and infrared images are compared to determine which combination is more accurate. The combinations are the CII-CVI, CII-GVI, GII-CVI, and GII-GVI. After preprocessing of the images, several images containing the iced structure are used to determine threshold levels for infrared and visual

images. Table 1 shows the threshold levels which are obtained for red, green and blue components and grayscale images.

Table 1—Threshold levels for components of R, G and B and grayscale images

Channel	Visual image		Infrared image	
	Lower level	Upper level	Lower level	Upper level
R	43	133	25	160
G	58	132	0	31
B	51	120	90	178
Grayscale	61	122	30	66

Five cases with different arrangements and angles are investigated to define their ice thicknesses. The histogram of case number 1 is calculated to discuss possible results. As Figure 2(a) shows, the histograms of three components, R, G and B, in their visual image are centered on the intensity of 100, and their deviations are almost the same. The grayscale histogram of the visual image is very similar to R, G and B histograms in shape, Figure 2(b). According to Table 1, the ice pixel intensity levels have similar values for R, G and B components and the grayscale image. Therefore, the CVI does not have more additional information than the GVI does.

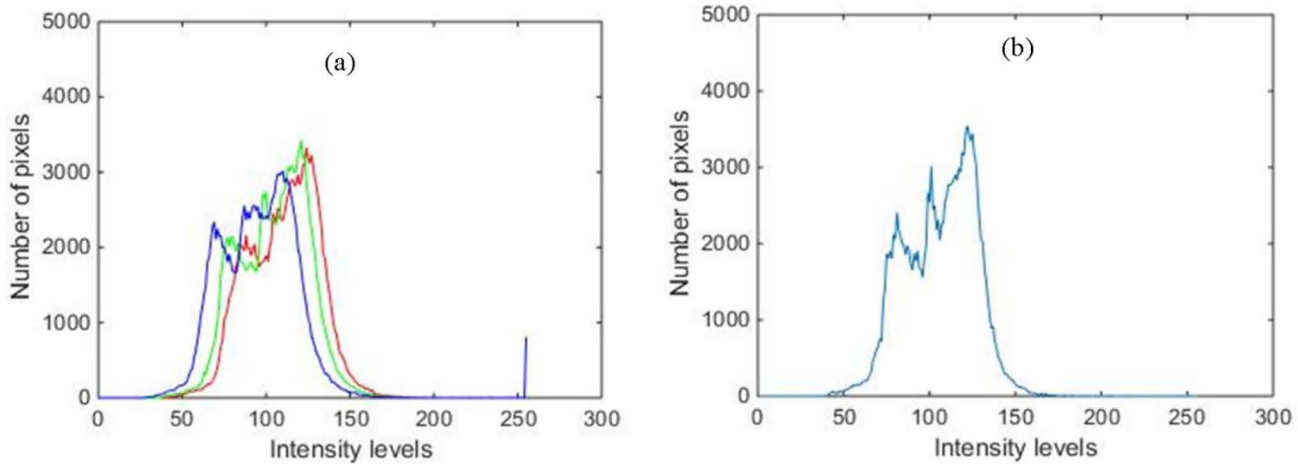

Figure 2—Histograms of the visual image of case number 1; a) CVI, b) GVI

The histograms of the CII, Figure 3(a), and the histogram of the GII, Figure 3(b), show different trends and shapes. According to data from Table 1, the values of ice intensity levels are different for the three components, R, G and B. Therefore, using combinations that include CII or GII causes different results. The color image has three independent components and there is more information in this type of image; consequently, the result of using the CII is more accurate than that of the GII.

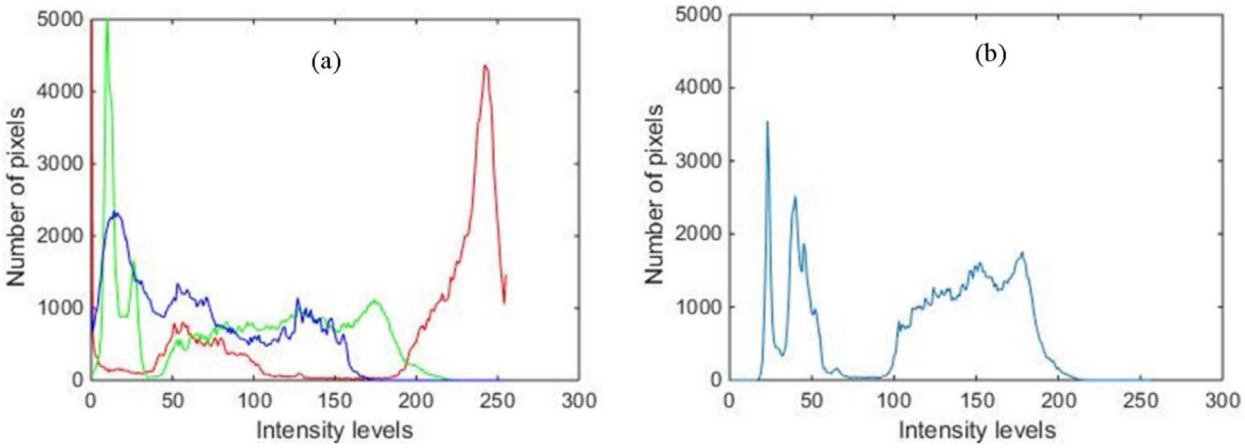

Figure 3—Histograms of the infrared images of case number 1; a) CII, b) GII

The threshold method is applied on images to create binary images. Binary images are obtained for five cases using different combinations of infrared images and visual images. In all cases, the target cylinder, covered by saline ice, is on top of the second cylinder, covered by fresh water ice. Some shadow appears in the visual image. The shadow does not have any effect on infrared images but its effect is shown in visual images. Therefore, using infrared images removes the effect of the shadow in the results. In case number 1, as Figures 4(a) and 4(b) show, the main cylinder mostly covers the lower one. Due to the different temperature and emissivity of the background with respect to the target object, the color of the target object is different from the background. This contrast with the background helps to extract the object from the background using threshold levels. Figure 4(c) shows the binary images acquired using the combination of CVI and CII. This combination shows fairly good results. Figure 4(f) shows the binary image obtained using the combination of GII, Figure 4(d) and GVI, Figure 4(e). An extra part is shown in Figure 4(f) that shows the threshold has considered part of the fresh water ice as the target ice. The shapes of the ice are detected and reported well in the binary image.

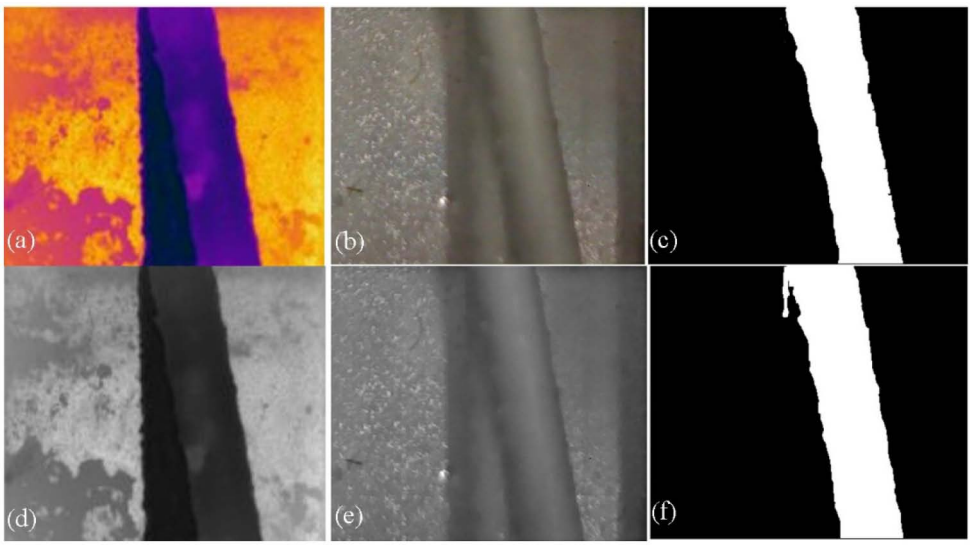

Figure 4—Extracted images for case number 1; a) CII, b) CVI, c) the binary image using a combination of CII and CVI, d) GII, e) GVI, f) the binary image using a combination of GII and GVI

In case number two, the target cylinder only covers a small portion of the second cylinder, shown in Figure 5. In both infrared and visual images, the second cylinder has the same color as the main cylinder; therefore, the object cannot be extracted using only the threshold method. Morphological algorithms are

used to remove the effect of the similarity of the object and the background. Figure 5(c) shows the binary image acquired using Figures 5(a) and 5(b). Figure 5(f) shows the binary image obtained using the GVI and CII. There is no difference between the results of the first and second combinations. The effect of using the morphological algorithms in the boundary of the binary image is shown in Figures 5(c) and 5(e).

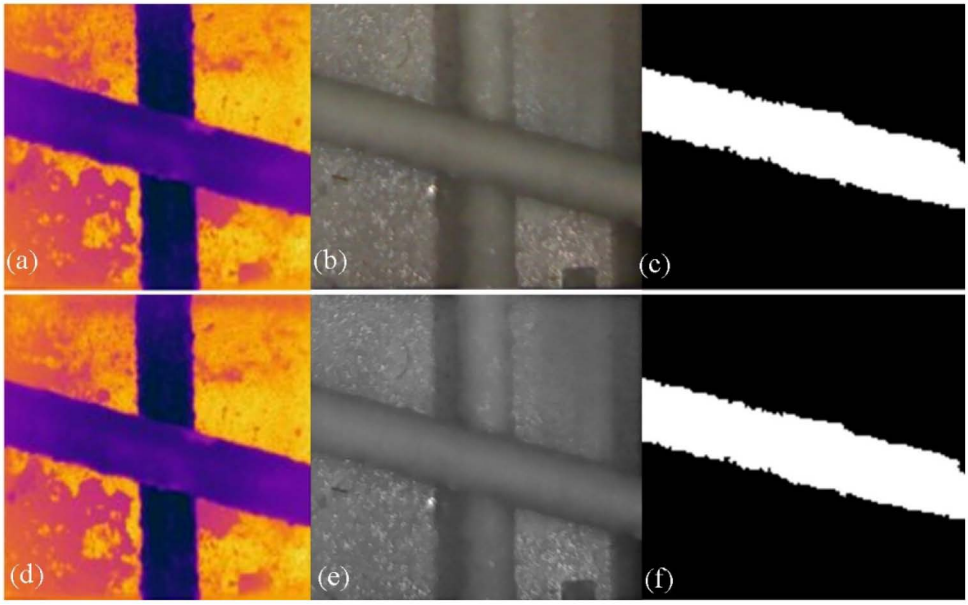

Figure 5—Extracted images for case number 2; a) CII, b) CVI, c) the binary image using the combination of CII and CVI, d) CII, e) GVI, f) the binary image using the combination of CII and GVI

As Figure 6 shows, in case number 3, some parts of the object have the same color as the background in the CII. The visual image helps to recognize the correct ice area of the target object and remove the part of the background that is considered as ice in the infrared image. Using infrared images, the shadow that appears in the visual image and has the same intensity as the ice is considered as the background. The morphological algorithms that are used to remove imperfection have a negative effect on the boundary in binary images. The combination using the GII is affected more by the morphological algorithms than that of the CII, and the ice in the bottom of the cylinder is not detected.

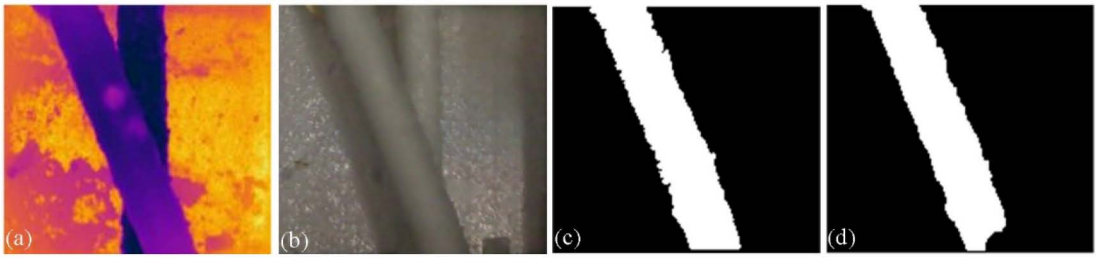

Figure 6—Extracted images for case number 3; a) CII, b) CVI, c) the binary image using the combination of CII and CVI, d) the binary image using the combination of GII and GVI

In case number 4, the visual image shows no ice in the bottom of the target cylinder, Figure 7(b), but because the cylinder has the same temperature as the ice, it has the same color as the ice in the infrared image, Figure 7(a). According to this proposed method, a pixel is considered to be ice if it belongs to the ice range of the visual and infrared images. Therefore, the bottom of the cylinder, which does not belong to the visual ice intensity range, is assumed as the background. Using CII in a combination has a better result

than the combination that uses GII. The effect of the morphological algorithm is shown in the boundary of binary images.

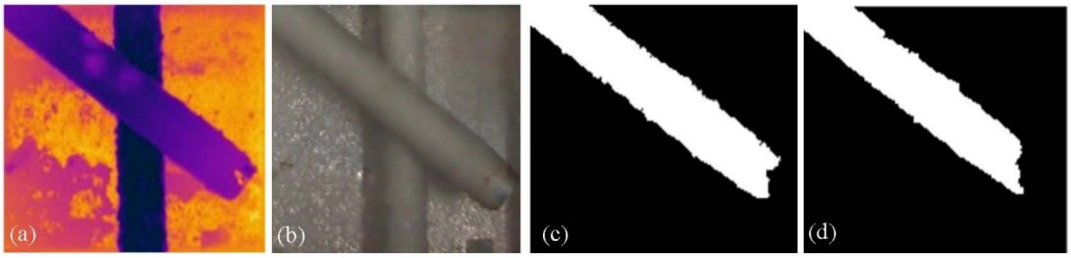

Figure 7—Extracted images for case number 4; a) CII, b) CVI, c) the binary image using the combination of OII and CVI, d) the binary image using the combination of GII and GVI

In case number 5, two cylinders are almost orthogonal to each other with a high similarity between the background and objects, shown in Figure 8. When applying the threshold method on a single image, these parts of the background are considered as the target object. Combining the images helps to recognize the ice area and background correctly. There are some similarities between the boundaries of fresh water and saline ice which appear in infrared and visual images. The morphological algorithms are used to remove these similarities. The effect of morphological algorithms on boundaries of ice is shown in Figures 8(c) and 8(f). The combination of the GII and GVI shows less accuracy in ice detection.

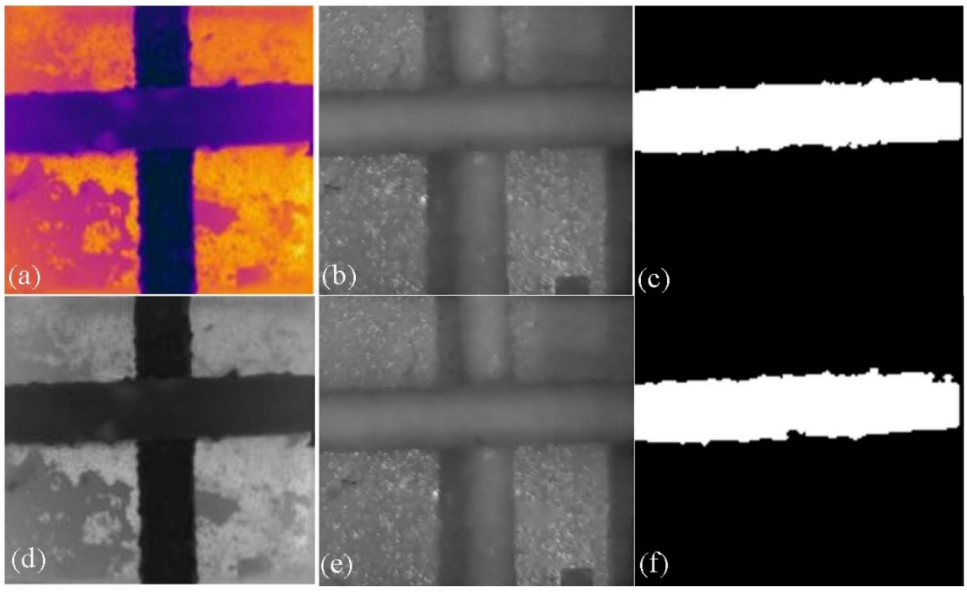

Figure 8—Extracted images for case number 5; a) CII, b) GVI, c) the binary image using the combination of CII and GVI, d) GII e) GVI, f) the binary image using the combination of GII and GVI

The ice thickness is measured at several points. The ice thickness is about 1.75 cm. Figure 9 shows the numerical results of the ice thickness calculated for every case. The results show that the combinations that use the CII calculate the ice thickness more accurately, while the combinations that use the GII have less accuracy. These results indicate that the combination with CVI has the same results as those of the GVI, which is expected from Figure 2. In cases 3 and 4, using the GII causes more inaccuracy in the results than in other cases. In case number 3, the main object and the background have a similarity in some areas. Using the CII in the combination is more useful to detect the ice area than using the GII. A larger size of an opening morphological algorithm is needed to remove the additional area that appears when using the GII in the combination. Increasing of the opening function size causes an increase in inaccuracy. In case number 4,

the morphological algorithms remove the area distributed around the bottom and reduce the number of ice pixels. As a result, a thinner ice is calculated in this case. The values of these results are less than those of the experimental result because the opening morphological operation is used to eliminate thin protrusions in the binary image.

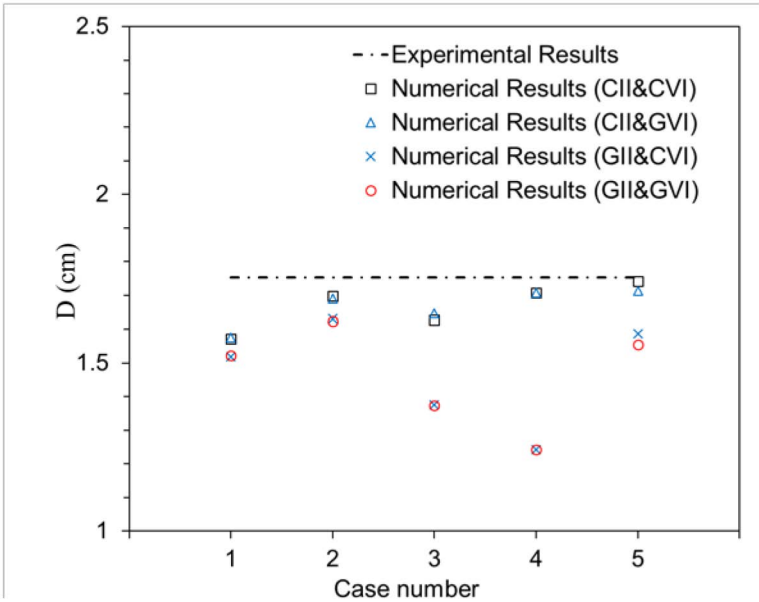

Figure 9—Comparison between ice thicknesses for five cases and the real measured thickness

Conclusions

A method is examined for the detection of ice and measurement of ice thicknesses on cylinders using infrared and visual images. Combinations of CVI, GVI, CII and GII are used to detect the ice region accumulated on structures. A median filter is applied on images to reduce noises, and at the same time, edges and image pixel values are preserved. The thresholding method based on the collected data is applied on infrared and visual images and the results of thresholding are combined to detect the ice area. The opening and closing morphological algorithms are used to fill gap areas in the ice region and eliminate narrow strips that appear in the image. The ice thickness is calculated counting the number of ice pixels and the camera parameter. The experimental and numerical results show that using CII in combination leads to more accurate results than combinations that use the GII. In this study, using CVIs and GVIs in combination has the same results. The applied morphological algorithms changed the boundaries but they did not cause a large amount of error when CII is used in combinations. The results showed less than 7.5 percent error in the combinations that used CII, which is acceptable. As a simple threshold method was used to detect the ice area, it caused some imperfections in the combined images which are removed using the morphological algorithm and consequently, caused some errors. More accurate segmentation methods can reduce this imperfect area in images and the result can be calculated accurately. Using an individual visual image with a high resolution visual camera provides more information, and is more useful as part of a combination to distinguish the ice area from the background.

Acknowledgements

The authors gratefully acknowledge the financial support from Statoil (Norway), MITACS, and Petroleum Research Newfoundland and Labrador (PRNL) (IT03198) for this research.

Nomenclature

B	Blue component
D	Ice thickness
G	Green component
I_{c1}	Binary image of the first combination
I_{c2}	Binary image of the second combination
I_{c3}	Binary image of the third combination
I_{c4}	Binary image of the fourth combination
I_g	Grayscale infrared image
I_{Hg}	Upper level of ice intensity in grayscale infrared images
I_{Hk}	Upper level of ice intensity for each component of color infrared images
I_k	Each component of color infrared images
I_{Lg}	Lower level of ice intensity in grayscale infrared images
I_{Lk}	Lower level of ice intensity for each component of color infrared images
I'_g	Grayscale visual image
I'_{Hg}	Upper level of ice intensity in grayscale visual images
I'_{Hk}	Upper level of ice intensity for each component of color visual images
I'_k	Each component of color visual images
I'_{Lg}	Lower level of ice intensity in grayscale visual images
I'_{Lk}	Lower level of ice intensity for each component of color visual images
i	Pixel row number
j	Pixel column number
R	Red component

References

Bodaghkhani, A., Dehghani, S.-R., Muzychka, Y.S., Colbourne, B., 2016. Understanding spray cloud formation by wave impact on marine objects. *Cold Reg. Sci. Technol*.

Casselgren, J., Rosendahl, S., Sjödahl, M., Jonsson, P., 2016. Road condition analysis using NIR illumination and compensating for surrounding light. *Opt. Lasers Eng*. **77**, 175–182.

Dehghani, S.R., Muzychka, Y.S., Naterer, G.F., 2016. Droplet trajectories of wave-impact sea spray on a marine vessel. *Cold Reg. Sci. Technol*. **127**, 1–9. doi:10.1016/j.coldregions.2016.03.010

Gong, X., Bansmer, S., 2015. 3-D ice shape measurements using mid-infrared laser scanning. *Opt. Express* **23**, 4908–4926.

Horjen, I., 2015. Offshore drilling rig ice accretion modeling including a surficial brine film. *Cold Reg. Sci. Technol*. **119**, 84–110. doi:10.1016/j.coldregions.2015.07.006

Hussin, R., Juhari, M.R., Kang, N.W., Ismail, R.C., Kamarudin, A., 2012. Digital image processing techniques for object detection from complex background image. *Procedia Eng*. **41**, 340–344.

Light, J., Parthasarathy, S., Mclver, W., 2012. Monitoring winter ice conditions using thermal imaging cameras equipped with infrared microbolometer sensors. *Procedia Comput. Sci*. **10**, 1158–1165.

Long, Z., Longde, G., Jianjun, Y., 2009. Investigation of ice shape measurement technique based on laser sheet and machine vision in icing wind tunnel, in: *Image and Graphics, 2009*. ICIG'09. Fifth International Conference on. IEEE, pp. 790–795.

Lozowski, E.P., Szilder, K., Makkonen, L., 2000. Computer simulation of marine ice accretion. *Philos. Trans. R. Soc. London A Math. Phys. Eng. Sci*. **358**, 2811–2845. doi:10.1098/rsta.2000.0687

Mohseni, M., Frioult, M., Amirfazli, A., 2012. Simultaneous monitoring of ice accretion and thermography of an airfoil: an IR imaging methodology. *Meas. Sci. Technol*. **23**, 105405.

Palmer A., D.J., 2009. Development of a Marine Icing Monitoring System. Proc. 20th Int. Conf. Port Ocean Eng. under Arct. Cond. 1–12.

Pasieka, J., Nanua, R., Coulombe, S., Servio, P., 2014. The crystallization of sub-cooled water: Measuring the front velocity and mushy zone composition via thermal imaging. *Int. J. Heat Mass Transf*. **77**, 940–945.

Rashid, T., Khawaja, H.A., Edvardsen, K., Mughal, U.N., 2015a. Infrared Thermal Signature Evaluation of a Pure and Saline Ice for Marine Operations in Cold Climate. *Sensors & Transducers* **194**, 62.

Rashid, T., Khawaja, H.A., Edvardsen, K., Mughal, U.N., 2015b. *Infrared Thermal Signature Evaluation of a Pure Ice Block*.

Rees, W.G., 2005. *Remote sensing of snow and ice*. CRC press.

Roebber, P., Mitten, P., 1987. *Modelling and measurement of icing in Canadian waters*. Atmospheric Environment Service.

Ryerson, C.C., 2011. Ice protection of offshore platforms. *Cold Reg. Sci. Technol*. **65**, 97–110. doi:10.1016/j.coldregions.2010.02.006

Ryerson, C.C., 2008. *Assessment of Superstructure Ice Protection as Applied to Offshore Oil Operations Safety: Problems, Hazards, Needs, and Potential Transfer Technologies*. Erdc/Crrel Tr-08-14 156.

Ryerson, C.C., 1995. Superstructure spray and ice accretion on a large U.S. Coast Guard cutter. *Atmos. Res*. **36**, 321–337. doi: 10.1016/0169-8095(94)00045-F

Wang, X., Hu, J., Wu, B., Du, L., Sun, C., 2008. Study on edge extraction methods for image-based icing on-line monitoring on overhead transmission lines, in: *High Voltage Engineering and Application, 2008*. ICHVE 2008. International Conference on. IEEE, pp. 661–665.

Yu, C., Peng, Q., Wachal, R., Wang, P., 2006. An Image-Based 3D Acquisition of Ice Accretions on Power Transmission Lines, in: 2006 Canadian Conference on Electrical and Computer Engineering. IEEE, pp. 2005–2008.

Zhong, Y., Zuo, Q., Zhou, Y., Zhang, C., 2013. A new image-based algorithm for icing detection and icing thickness estimation for Transmission Lines, in: Multimedia and Expo Workshops (ICMEW), 2013 IEEE International Conference on. IEEE, pp. 1–6.

Effect of Ambient Conditions on Infrared Ice Thickness Measurement

Azam Fazelpour[1]; Saeed R. Dehghani[2]; Vlastimil Masek[1]; Yuri S. Muzychka[2],
[1] Department of Electrical Engineering, Memorial University of Newfoundland
[2] Department of Mechanical Engineering, Memorial University of Newfoundland

Introduction

Structure icing is a phenomenon influencing marine and offshore activities during cold seasons in Arctic regions[1]. Therefore, monitoring ice conditions plays an important role in deicing structures. Some models have been established to predict the amount of ice load on marine structures. Considering the difficulties and unsafe situations caused by harsh weather, indirect methods have been developed to measure accumulated ice. It is very important to design algorithms which automatically monitor icing situations [2].

Some indirect methods have been developed based on visual image processing. Positive results have been obtained using visual imaging in special conditions such as clear scene, high contrast, and also appropriate lighting [3]. Visual cameras need light during dark times, and cannot provide a clear image in foggy conditions[4]. In order to overcome these shortcomings of visual cameras, the use of thermal cameras is proposed. As thermal images are captured according to the object's temperature, inappropriate lighting and weather conditions do not affect imaging. This method measures the thickness of ice accumulated on structures in situations in which visual imaging is unable to extract the ice boundary [5].

In this study, a new method is developed to measure ice thickness using thermal imaging. An experimental setup is conducted to capture thermal infrared images. Using thresholding methods and morphological algorithms, the ice area is extracted. The ice thickness is measured in high flux light and low flux light conditions with black and white backgrounds.

Methodology

A thresholding algorithm based on the Otsu method is performed to detect ice area. This thresholding method divides the image into the background and the main target [6]. Ice pixels are represented by a value of 1 in the image and background pixels are represented by a value of 0. A binary image with some imperfect areas is thus obtained using the Otsu method. These imperfect areas are the result of small objects in the image with a close intensity of ice. The erosion and dilation morphological algorithms are used to remove this imperfect area in the binary image.

$$I_B(i,j) = \begin{cases} 1 & I(i,j) > T_{Otsu} \\ 0 & Otherwise \end{cases}$$

T_{Otsu}: Otsu threshold

I_B: Binary image

I: Infrared image

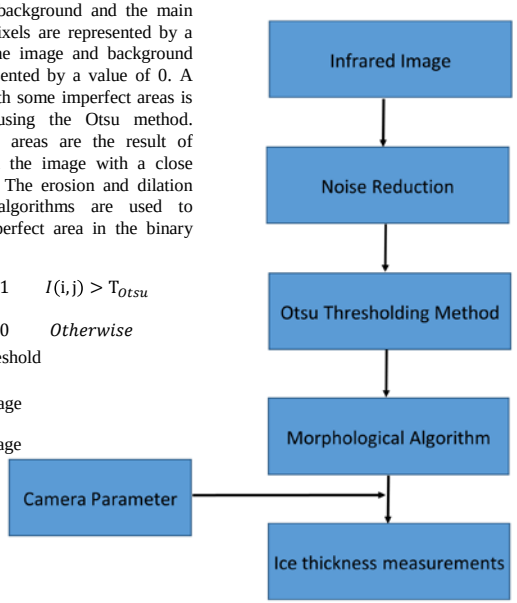

Figure 1. Block diagram of ice thickness measurement

Results and Discussion

An experimental set up is conducted at a temperature of -15°C. A cylindrical structure, covered with ice, is the main object in the image. The camera calibration is performed using the distance of the thermal camera from the object and a using a real dimension value on the object. The effect of the background color is investigated using a black and a white background behind the main object. In order to study the effect of light on ice measurements, images are captured in low light lux and high light lux conditions. Therefore, four cases are obtained to measure ice thicknesses. These cases include black background with high light, black background with low light, white background with high light and white background

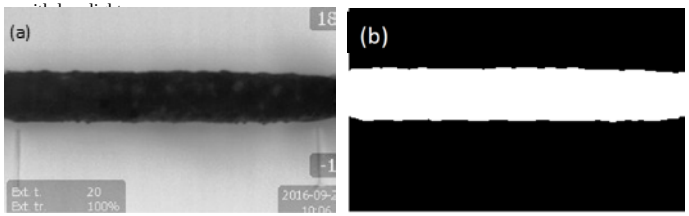

Figure2. Extracted images; a) infrared image with black background and high light, b) the binary image applying the method on Figure a

Figure 2-5 shows the binary images obtained by applying the steps, shown in Figure 1, to infrared images in the four mentioned situations

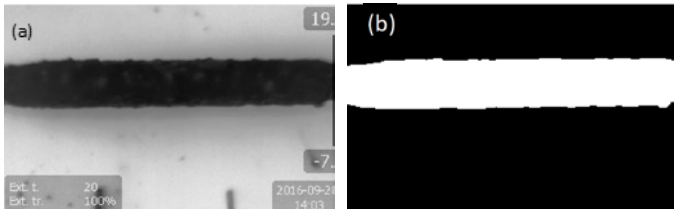

Figure3. Extracted images; a) infrared image with black background and low light, b) the binary image applying the method on Figure a

The infrared images obtained in these four combinations are almost same; therefore, similar binary images are acquired. Although using morphological algorithms causes changes in the edges of the images, these changes cause slight inaccuracies in the ice measurements.

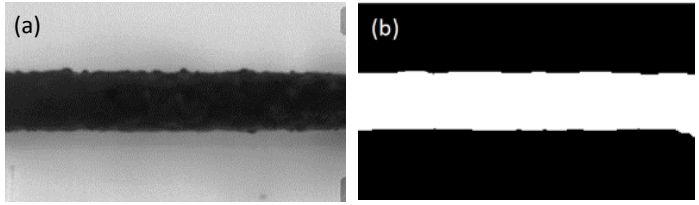

Figure4. Extracted images; a) infrared image with white background and high light, b) the binary image applying the method on Figure a

The real value measured for ice thickness is 5.3 cm. Table 1 shows the ice thicknesses calculated for the cases with a black and a white background in the light with 0 lux and 350 lux. The results show high accuracy with less than 3 percent error.

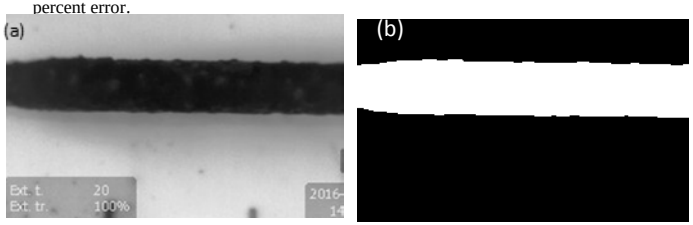

Figure5. Extracted images; a) infrared image with white background and low light, b) the binary image applying the method on Figure a

In the case with white background and high light, the calculated ice thickness is 5.44 cm which is less accurate than other results. This error is the result of a dark area appearing at the end of the corresponding cylinder. The time duration of capturing the image causes the dark area in this image. The results are extremely reliable and accurate.

Table 1. The measured ice thickness according to background color and light

Light Flux	White Background	Black Background
0 (lux)	5.24(cm)	5.21(cm)
350 (lux)	5.44(cm)	5.35(cm)

Conclusion

Accurate results are obtained for ice thickness using infrared imaging. The results illustrate that the background color and the value of light do not affect the ice measurements where the infrared camera are used.

Acknowledgement

The authors gratefully acknowledge the financial support from Statoil (Norway), MITACS, Petroleum Research Newfoundland and Labrador (PRNL) and ABS for this research.

References

[1] A. Bodaghkhani, S.R. Dehghani, Y. S. Muzychka, and B. Colbourne, "Understanding spray cloud formation by wave impact on marine objects," *Cold Reg. Sci. Technol.*, vol. 129, pp. 114–136, 2016.

[2] C. C. Ryerson, "Ice protection of offshore platforms," *Cold Reg. Sci. Technol.*, vol. 65, no. 1, pp. 97–110, 2011.

[3] Y. P. Zhong, Q. Zuo, Y. Zhou, and C. Zhang, "A new image-based algorithm for icing detection and icing thickness estimation for Transmission Lines," *Electron. Proc. 2013 IEEE Int. Conf. Multimed. Expo Work. ICMEW 2013*, 2013.

[4] B. Akbal, "System Design And Implementation To Melt The Ice Occurring In High Voltage Aerial Transmission Lines," *Ph.D., Selçuk Univ. Konya, Turkey*, 2015.

[5] M. Shokr and N. Sinha, *Sea ice: physics and remote sensing*. John Wiley & Sons, 2015.

[6] N. Otsu, "A threshold selection method from gray-level histograms," *Automatica*, vol. 11, no. 285–296, pp. 23–27, 1975.